UNIVERSITÀ DEGLI STUDI DI PADOVA

SCUOLA DI SCIENZE
Dipartimento di Geoscienze
Direttore Prof. Nicola Surian

TESI DI LAUREA MAGISTRALE IN GEOPHYSICS FOR NATURAL RISKS AND RESOURCES

A quantitative multidisciplinary approach for understanding the role of plants in salt-marsh retreat: the case study of the San Felice salt marsh (VE)

Relatore: Chiar.mo Prof. Andrea D'Alpaos
Correlatore: Chiar.mo Prof. Jacopo Boaga

Laureanda: Teresa Moschitta
Matricola: 2076731

ANNO ACCADEMICO 2024-2025

Dedicated to Zelda

CONTENTS

1 INTRODUCTION 1
2 VENICE LAGOON AND SAN FELICE SALT MARSH 4
2.1 Geographical overview 4
2.2 Geological setting, geomorphological features and anthropological modifications 5
2.3 Salt Marshes 7
2.4 The role of plants in salt marshes 8
3 MATERIALS AND METHODS 11
3.1 Seismic Refraction 11
3.1.1 Data acquisition 14
3.1.2 Data processing 18
3.2 Remote Sensing 20
3.2.1 Data sampling with Google Earth Pro 21
3.2.2 Data processing with QGIS 23
3.3 Wind Wave-Tidal Model 25
3.4 Soil Core Analysis 28
3.4.1 Field sampling 28
3.4.2 Laboratory Processing 29
4 RESULTS 31
4.1 Seismic Refraction 31
4.2 Remote Sensing 42
4.3 Wind Wave-Tidal Model 61
4.4 Soil Core Analysis 69
5 DISCUSSION 74
6 CONCLUSIONS AND FUTURE WORKS 78
APPENDIX A 81
APPENDIX B 86
REFERENCES 110
ACKNOWLEDGEMENTS 118

ABSTRACT

Salt marshes are delicate yet rich environments expected to undergo significant changes due to the rise in sea levels caused by climate change. They are low-lying intertidal wetlands characterised by halophytic herbaceous plants, often divided by networks of tidal channels that facilitate the exchange of water, sediments, and nutrients between tidal flats and the open sea. This thesis aims to understand the role of plants in mitigating salt marsh retreat, using the San Felice salt marsh (Venice Lagoon) as an example. Four different quantitative approaches were employed to achieve this.

Ten seismic refraction datasets were collected in 2023 and 2024 in vegetated and non-vegetated soils under both low and high tide conditions. The data were processed and inverted (Rücker et al., 2017) to model the velocity propagation of subsurface waves. The results showed significant differences between vegetated and non-vegetated areas, indicating that plants' roots can substantially modify the mechanical properties of subsurface sediments - with higher organic matter and water content in vegetated areas likely contributing to this effect.

A spatial-temporal analysis covering a twenty-year period was conducted on four channels of the San Felice salt marsh: the Gaggian Channel, the San Felice Channel, an artificial channel, and the channel where geophysical surveys were performed. The observed migration rates suggest that bank retreat is primarily driven by hydrodynamic forces, such as currents and wind waves, with estimated rates on the order of 0.30 m/yr. While this highlights the dominant role of hydrodynamic processes in driving salt marsh retreat, the specific contribution of vegetation to mitigating lateral erosion could not be conclusively demonstrated, mainly due to the lack of non-vegetated marsh surfaces at comparable elevations for direct comparison.

Additionally, a combined wind wave-tidal model (Carniello et al., 2005, 2011) demonstrated a strong coupling between water level, wave height, and total bottom shear stress, indicating that high tides coincide with increased wave action and enhanced erosion potential.

Finally, four core samples collected in the San Felice salt marsh were analysed for water content and loss-on-ignition (LOI). The results revealed a strong correlation between water content and organic matter content, which is consistent with the seismic observations and further supports the hypothesis that vegetation influences the mechanical behaviour of surface sediments through root-induced processes.

Overall, the study demonstrates that salt marsh vegetation can modify the mechanical properties of subsurface sediments and may contribute to enhancing soil resistance. However, the systems’ complex dynamics and the current limitations in site comparison call for further research to fully elucidate the role of vegetation in controlling salt marshes’ lateral erosion.

RIASSUNTO

Le barene sono ecosistemi ricchi e delicati che si stima possano andare incontro a trasformazioni significative a causa dell'innalzamento del livello medio del mare dovuto al cambiamento climatico. Si tratta di zone umide, intertidali a bassa latitudine caratterizzate da piante erbacee ed alofite ed attraversate da canali tidali che facilitano lo scambio di acqua, sedimenti e nutrienti tra piane mareali e il mare aperto. Lo scopo di questa tesi è comprendere il ruolo delle piante nel mitigare l'erosione laterale delle barene, con la barena San Felice (Laguna di Venezia) studiata come esempio. Quattro diversi metodi quantitativi sono stati utilizzati per questo obiettivo.

Dieci set di dati di sismica a rifrazione sono stati raccolti nel 2023 e 2024 in suoli vegetati e non vegetati in condizioni di bassa ed alta marea. I dati sono stati processati e ne è stata fatta l'inversione (Rücker et al., 2017) per modellare le velocità di propagazione delle onde sismiche nel sottosuolo. I risultati hanno dimostrato differenze significative tra aree vegetate e non vegetate, indicando che le radici delle piante potrebbero giocare un ruolo importante nel modificare le proprietà meccaniche del sottosuolo - con un possibile contributo dovuto al maggior contenuto di materia organica e di acqua nelle aree vegetate.

Un'analisi spazio-temporale è stata realizzata nell'arco di venti anni su quattro canali: il Canale San Felice, il Canale Gaggian, un canale artificiale ed il canale dove sono state condotte le indagini geofisiche. I tassi di migrazione osservati suggeriscono arretramenti dovuti principalmente a forze idrodinamiche, come correnti ed onde generate dal vento, dai valori stimati nell'ordine dei 0.30 m/anno. Nonostante questi risultati mettano in luce un ruolo dominante da parte dei processi idrodinamici nell'erosione laterale delle barene, il contributo specifico da parte delle piante per mitigare questo effetto non è potuto essere dimostrato in modo conclusivo a causa della scarsa presenza di superfici di barena non vegetate ad elevazioni comparabili per un confronto diretto.

Inoltre, un modello combinato tra onde di vento e maree (Carniello et al., 2005, 2011) ha dimostrato un effetto combinato tra livello d'acqua, altezza d'onda e stress al fondo,

indicando che l'alta marea coincide con un'azione delle onde maggiore ed un aumento dello stress al fondo.

Infine, quattro campioni di carote, raccolti nella barena San Felice, sono stati analizzati per individuarne il contenuto d'acqua e materia organica via loss-on-ignition (LOI). I risultati hanno dimostrato una forte correlazione tra contenuto d'acqua e materia organica, il che è coerente con le osservazioni fatte per i modelli sismici e supporta ulteriormente l'ipotesi che la vegetazione influenzi il comportamento meccanico dei sedimenti superficiali attraverso processi indotti dalle radici.

Complessivamente, lo studio dimostra che la vegetazione delle barene può modificare le proprietà meccaniche dei sedimenti e potrebbe contribuire a migliorare la resistenza del suolo. Tuttavia, la complessa dinamicità del sistema e le limitazioni attuali nel confronto tra diverse zone richiedono ulteriori ricerche per chiarire completamente il ruolo della vegetazione nel controllare l'erosione laterale delle barene.

1 INTRODUCTION

Coastal salt marshes are dynamic intertidal environments where sediment deposition and organic matter accumulation create fertile soils and complex ecosystems, and socio-economically, one of the most valuable natural assets (Blount et al., 2022). These zones function as natural filters between marine and terrestrial systems, playing a key role in stabilising coastlines by dissipating wave energy and storing “blue carbon”. In recent decades, the significance of salt marshes has grown, not only because of their ecological value but also due to their potential to mitigate climate change through carbon sequestration (Puppin, 2022). Because of climate change, these systems are vulnerable to retreat due to increasing sea-level rise, storm frequency, and human pressures. Understanding the processes of salt marsh evolution is therefore essential for sustainable coastal management and adaptation strategies to future scenarios (FitzGerald et al., 2021; Gedan et al., 2010).

Salt marshes are intertidal zones characterised by continuous interactions among hydrodynamic forces, sediment transport, and biological activity. They develop due to both natural processes, such as tidal fluctuations, riverine sediment supply, storm events, and human-induced alterations that impact sediment distribution and ecosystem dynamics. These environments contribute to coastal stability by dissipating wave energy, with vegetation acting as a natural barrier against erosive forces, sequestering carbon through organic matter accumulation, and creating diverse habitats that foster rich biodiversity (Tosi et al., 2024; Möller et al., 2014).

Salt marshes are studied with different approaches. Satellite and aerial imaging have transformed our capability to monitor salt marsh evolution over time. High-resolution multispectral imagery, LiDAR, and time-series analyses enable researchers to delineate salt marsh boundaries, quantify area loss, and map internal channel migration with remarkable precision. For instance, studies by Campbell and Wang (2019) and Friess et al. (2012) have demonstrated the efficacy of applying remote sensing tools and GIS software to track shoreline changes and assess habitat degradation in response to sea-level rise and storm events. Other studies - such as Lopes et al. (2020) and Sun et al.

(2018) - employed Landsat imagery and advanced classification algorithms to map long-term vegetation dynamics and sediment deposition. Blount et al. (2022) highlighted some uncertainties associated with mapping salt marsh boundaries: while moderate-resolution satellite imagery is broadly compelling, these datasets' inherent spatial resolution limits can introduce errors when delineating narrow or highly dynamic marsh shorelines.

Researchers have increasingly turned to geophysical techniques to investigate the subsurface characteristics of salt marshes. Electrical resistivity tomography (ERT) has proven valuable in reconstructing the internal stratigraphy and evaluating soil mechanical properties. Boaga et al. (2014) utilised ERT to explore plant–soil interactions in the Venice Lagoon, revealing how extensive root networks can alter sediment compaction and water retention behaviour.

A crucial function of salt marsh vegetation is its ability to attenuate wave energy under extreme hydrodynamic conditions. Möller et al. (2014) conducted experimental studies demonstrating that vegetation can cause considerable wave attenuation during storm surge events, thereby reducing the erosive force exerted on salt marsh boundaries. Their work highlights that the attenuation capacity is closely related to vegetation density and structure, identifying the protective role of plant communities in mitigating storm-induced erosion.

Understanding salt-marsh depositional history and organic matter dynamics requires detailed sediment sampling and laboratory analysis. Core sampling techniques, loss-on-ignition (LOI) measurements, and grain size analysis have allowed researchers such as Puppin et al. (2025) to reconstruct vertical profiles of organic matter content and water retention. These analyses provide insights into long-term accretion processes and the functioning of salt marshes as carbon traps. Roner et al. (2016) demonstrated the relationship between sediment composition and hydrodynamic conditions to assess the overall stability of these environments.

Studies on salt marsh ecomorphodynamic evolution emphasise the importance of an integrated, multidisciplinary approach, which, combining remote sensing, geophysical techniques, and numerical simulations, provides surface and sub-surface data that yield an exhaustive picture of marsh dynamics.

Comparing observational data and predictive models, current research attempts are moving toward more robust assessments of salt marsh vulnerability and resilience. Such efforts will be critical in guiding both the restoration of degraded marshes and the sustainable management of coastal regions worldwide.

This thesis aims to understand the role of vegetation in mitigating salt marsh retreat using a quantitative, multidisciplinary approach. We acquired data revealing differences in soil mechanical properties using seismic refraction techniques on vegetated and non-vegetated areas during low and high tide conditions. The seismic velocity models indicate that roots influence the shallow subsurface by reducing compaction. At the same time, deeper layers exhibit signs of enhanced consolidation likely linked to root suction effects.

With Google Earth Pro and QGIS, we have monitored changes in the marsh area and channel migration over a twenty-year period. This analysis quantified the amount of channel migration and documented a nearly linear reduction in the salt marsh area.

A combined wind wave-tidal model (developed by Carniello et al., 2005) was used to simulate the hydrodynamic forces within the marsh by correlating water level, wave height, and total bottom shear stress.

Laboratory processing of core samples from vegetated and non-vegetated patches enabled us to assess the vertical distribution of organic matter and water content. The higher concentrations of organic matter observed in vegetated areas support our hypothesis that plants contribute to the altered mechanical behaviour of the soil in its surface layers.

The objective of this thesis is to elucidate how vegetation influences the physical properties of the San Felice salt marsh soil, specifically by modifying the subsurface structure through processes such as root-induced fracturing and suction, which may mitigate erosion.

2 VENICE LAGOON AND SAN FELICE SALT MARSH

2.1 Geographical overview

The Lagoon of Venice is in northeastern Italy, in the Veneto region, in the provinces of Venice and Padua. It is located in the Gulf of Venice, which extends along the northern Adriatic coast, with an oblong, arched shape and bounded by the Sile River to the North and the Brenta River to the South. It is the largest lagoon in the Mediterranean Sea, and its surface is around 500 km^2. It is 50 km long and between 8 and 14 km wide. It is connected to the sea by three port inlets: Chioggia, Malamocco and Lido (Brambati et al., 2003; Bondesan, 2017).

There are nine municipalities in the Venice Lagoon: Venice (Venezia), Campagna Lupia, Cavallino-Treporti, Chioggia, Codevigo (PD), Jesolo, Mira, Musile di Piave, and Quarto d’Altino, with a total population of 407000 (Wikipedia, 2025).

The San Felice salt marsh (area of interest for this thesis) is in the Venice Lagoon, Northeast of Venice and North of Cavallino-Treporti. Its elevation varies between 0 m a.s.l. and 40 cm a.s.l. It is delimited by two main channels: the San Felice Channel and the Gaggian Channel (Figure 2.1).

Figure 2.1: Aerial view of the Venice Lagoon. In the black panel: Italy (red) and the Veneto Region (blue); in the yellow panel, the Venice Lagoon; in the red panel, the San Felice Salt Marsh, bordered by the San Felice Channel and the Gaggian Channel (2021 orthophotography).

2.2 Geological setting, geomorphological features and anthropological modifications

The Venetian area is at the centre of the Neogene-Quaternary foreland, North of the Adria microplate, between the Northern Apennine range (NE-vergent) and the Western-Southern Alpine range (S-vergent) (Tosi et al, 2007).

The Lagoon of Venice originated around 6 to 7 kyr, establishing, approximately, the coast in its current position. The early lagoon was smaller than today, featuring eight inlets for water exchange with the sea, compared to the three that exist now. Two main factors influenced the lagoon's growth: the sediment supply from the Adige, Bacchiglione, Brenta, Sile, and Piave rivers flowing into the lagoon, resulting in a filling rate that exceeded natural subsidence and eustatic sea level rise; and the coastal nourishment, also from the Po River to the south, which led to the silting of tidal inlets (Brambati et al., 2003).

The substratum is characterised by folds and faulted overfolds (clastic origin) parallel to the primary tectonic trend of the Apennines. It includes several gas-bearing traps at depths higher than 2000 m. The quaternary sediments mainly consist of sandy and silty-clayey layers of alluvial and marine origin (Tosi et al., 2007; Brambati et al., 2003).

The entire area is impacted by both natural and anthropogenic subsidence. Geological subsidence occurs due to tectonic processes (less than 0.5 mm/yr) and sediment consolidation (1.3 mm/yr). Anthropogenic subsidence is caused by groundwater withdrawals (more than 2.5 mm/yr). The overall relative land subsidence amounts to an elevation loss of 23 cm, 12 cm of land subsidence, both natural (3 cm) and anthropogenic (9 cm), and 11 cm of sea level rise during the last century.

The relative 23 cm rise in the sea level in the Lagoon has contributed to the increase in:

- the flooding phenomenon, both in frequency and degree, with damages to population and monumental patrimony;
- the hydrodynamics inside the lagoon, leading to erosion of its floor, channel silting up, and changes in the internal eco-morphology;
- the fragility of litorals, enhancing the risk of destructive sea storms and flooding from overtopping (Brambati et al., 2003).

The Venetian Lagoon was a strategic area for defence and economic trade. From 1400 AD, the Venetians began to preserve it through various hydraulic works. They avoided turning the lagoon into a marshland, but also caused an abrupt reversal in its natural evolution. In the 17th century, the major rivers (Brenta, Bacchiglione, Sile, Adige and Piave) were diverted at the southwest and northeast borders of the lagoon itself into the Adriatic Sea to prevent silting of the lagoon and its channels. Since the 1900s, the natural setting of the lagoon became fully a tidal environment, with no fluvial influence (Brambati et al., 2003; D'Alpaos, 2010).

To facilitate the entry of larger vessels into the lagoon, from 1882 to 1935, deeper canals were excavated, altering the tidal regime of the area due to the increased current velocity. This led to larger areas of the basin becoming ebb-dominated, which heightened erosion and resulted in sediment loss in the sea (D’Alpaos, 2010).

The most recent intervention in the lagoon is the Mo.S.E Project, which has been designed and installed in front of the three inlets to protect the city of Venice and other lagoon settlements from flooding during abnormally high tides. The project has resulted in slightly reduced tidal amplitude and increased tidal phase delay within the lagoon (Baccarin, 2024).

Nowadays, the riverine sediment input is null. Over time, marine properties began to dominate, further enhanced by human interventions. The lagoon comprises shallow, tidal flats, salt marshes, islands and a dense network of channels (Brambati et al., 2003). The lagoon experiences a semidiurnal micro tidal regime with an average tidal range of one metre (Merlo, 2016).

2.3 Salt Marshes

Salt marshes are delicate environments anticipated to undergo substantial changes or, potentially, to vanish entirely in the coming centuries due to sea level rise. These environments are found worldwide in warm to cool latitudes (>30° latitude), behind barrier islands, bordering estuaries, and lower delta plains. Sea level rise will primarily drive the loss and degradation of coastal marshes, exacerbated by human activities such as dredging and filling, reductions in sediment supplies, and hydrocarbon withdrawals (FitzGerald et al., 2021; Fagherazzi et al., 2012).

Salt marshes are low-lying intertidal wetlands characterised by halophytic herbaceous plants. Floods or tides periodically inundate these areas and constitute a transition zone between deep water aquatic systems and terrestrial environments. Depending on their morphology, the development and evolution of these environments involve aggradation and degradation along the margins and surface of salt marshes. Aggradation processes encompass organic and inorganic accumulation at a rate primarily determined by sea-level rise. The vertical growth of salt marshes is associated with a rapid influx of inorganic sediment due to floods, storm surges, and human disturbances. Also, the presence of growing plants means marsh aggradation (FitzGerald et al., 2021; Marani et al., 2006; Tognin et al., 2024).

Degradation processes can be vertical or horizontal. One of the main processes is the physical erosion of wind-generated waves that act on marsh margins: a sharply inclined scarp develops due to undercutting, which may lead to a cantilever collapse or a toppling failure. Boat wakes and other human activities may exacerbate this process. Another component of degradation is vertical subsidence. In undisturbed marshes, accretion and autocompaction (compression of water and gas-filled organic structures with increasing overburden) are usually in relative equilibrium. When the sedimentation inflow is altered, subsidence may be the winning process. A coupled process of rising sea level, wind waves, and subsidence may endanger the salt marsh (Tosi et al., 2024; FitzGerald et al., 2021; Fagherazzi et al., 2012).

Salt marsh platforms are often dissected by networks of tidal channels, which can be simple and linear or more complex, resembling dendritic or meandering patterns. These channels are crucial as they facilitate the exchange of water, sediments, and nutrients between the adjacent tidal flats and the open sea. The development of channels on marsh platforms is driven by the concentration of flow, which is enhanced by the presence of random perturbations in the elevation of the marsh platform (Soldati et al., 2017).

2.4 The role of plants in salt marshes

It is still debated whether plants directly or indirectly prevent or slow down the retreat process of salt marshes. Feagin et al. (2009) state that the primary variable influencing the lateral erosion of salt marshes is the soil type, while plants do not directly reduce wetland edge erosion but do so indirectly through modifications of soil parameters. Möller et al. (2014) affirm that vegetation causes considerable wave attenuation in storm surge conditions. Boaga et al. (2014) found that roots' suction increases during marsh flooding, creating a persistently aerated layer below the flooded surface.

What is certain is that the presence of vegetation promotes vertical growth due to the accumulation of sediments trapped by the plants themselves (Marani et al., 2006). FitzGerald et al. (2021) stated that vegetation growth is the most visible and often dominant process of marsh buildup. It provides the framework of interwoven roots and rhizomes that strengthen the resulting peat.

In the 2004 review, Marani et al. stated that salt marshes' stability is linked to the presence and distribution of halophytic vegetation. Vegetation stabilises marsh surface sediments, increases friction against hydrodynamic flow, and reduces the water's sediment transport capacity. This process favours sediment deposition and inhibits the formation of wind-induced waves that cause sediment resuspension.

Fagherazzi et al. (2012) modelled that the consolidation of clays and silts is strengthened by the rooting activities of the vegetation, strongly increasing the shear strength of the sediment bed. Furthermore, numerical simulations demonstrated that vegetation determines the rate of marsh progradation and regression during marsh retreat (Figure 2.2).

Vannoppen et al. (2017) and Hollis et al. (2018) showed that plant roots are very efficient in reducing concentrated flow erosion rates, depending on the apparent soil cohesion and the root-system type: fine, fibrous roots are most effective in non-cohesive soils (sands and silts).

In the San Felice salt marsh, the following plants can be found: *Inula crithmoides*, *Suaeda maritima*, *Sarcocornia fruticosa*, *Limonium narbonense*, *Halimione portulacoides*, *Puccinellia palustris*, and *Juncus maritimus* (Marani et al., 2004). A description of the aforementioned plants can be found in Appendix A. Unfortunately, none of these plants were photographed in their natural habitat during the field campaigns.

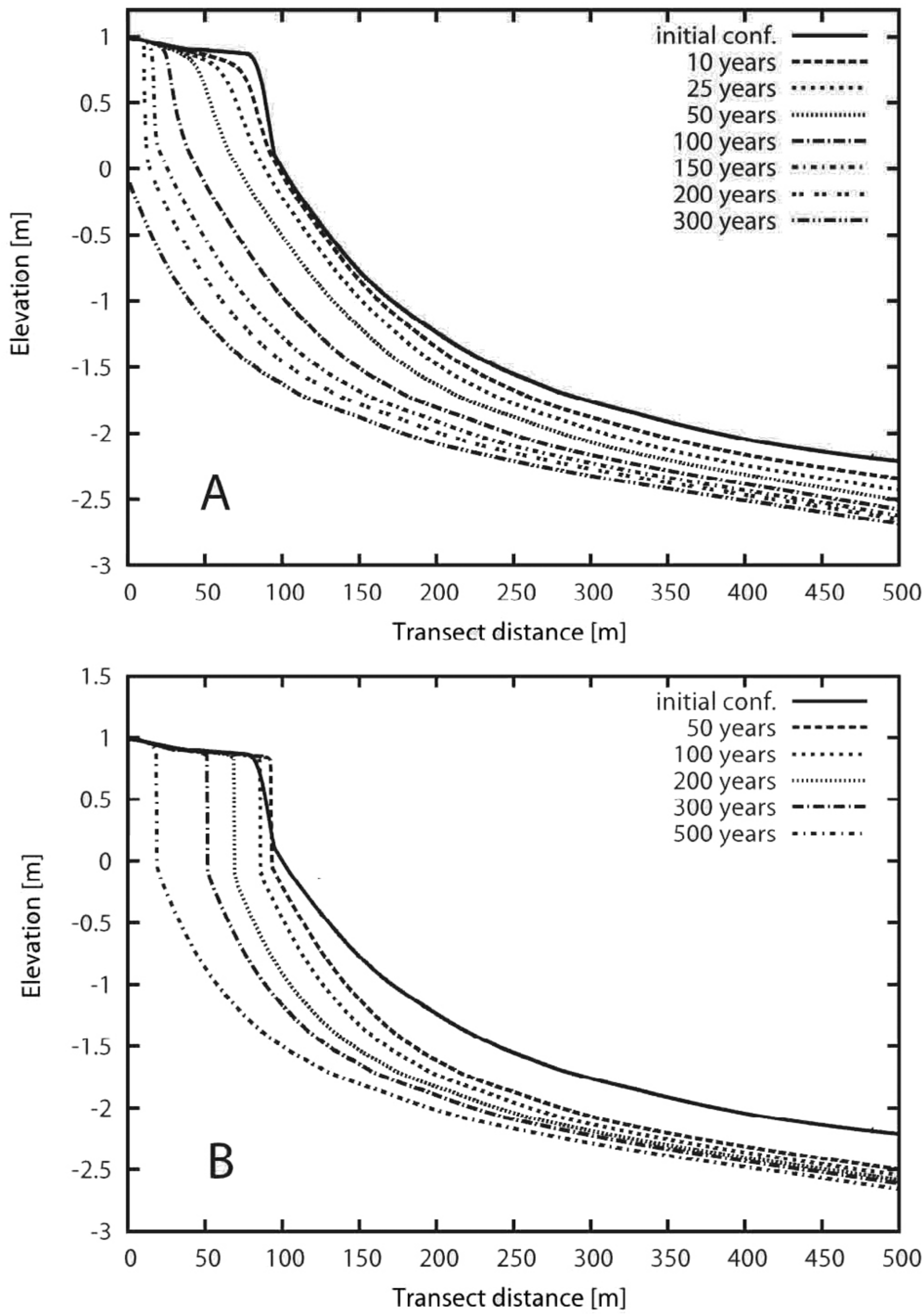

Figure 2.2: Erosion of salt marsh boundary simulated with the model of Mariotti and Fagherazzi (2010). (A) without vegetation, (B) with vegetation (Fagherazzi et al., 2012).

3 MATERIALS AND METHODS

3.1 Seismic Refraction

Seismic refraction surveying is a technique within applied seismology used to investigate subsurface structures. The method works by generating seismic waves in the subsoil and observing the refracted waves that travel along particular interfaces to the surface to retrieve the seismic velocity of the layers present (Levergne, 1989). From such values, it is possible to derive geotechnical parameters such as rock strength, rippability and potential fluid content (Reynolds, 2011).

Seismic waves are elastic waves that propagate through the Earth's interior and along its surface. These waves are generated by natural phenomena, such as earthquakes and volcanic eruptions, or by anthropogenic sources (controlled explosions). They are classified into two types: body waves and surface waves. Body waves, which travel within the Earth, can be compressive waves (primary or P waves) and shear waves (secondary or S waves). Surface waves are divided into Love and Rayleigh waves, which travel along Earth's surface (Encyclopaedia Britannica, 2023).

The seismic refraction method is based on the principle that when a body wave encounters a boundary with a contrast in velocity, the direction of travel and velocity of that wave changes according to the mechanical properties of the new medium (Reynolds, 2011). A part of the wave is reflected into the first medium, while another is refracted into the second. The incident wave is split into compressional and shear reflected and refracted components, a process known as P-to-S conversion (Everett, 2013) (Fig. 3.1a).

Consider the simple case shown in Figure 3.1b. The ray incident at the critical angle i_c travels along the interface as a P-wave with velocity V_2, where the angle of refraction r_c=90°. To derive the critical angle, it is possible to write Snell's law as:

$$\frac{\sin i_c}{v_1} = \frac{\sin r_c}{v_2} \tag{3.1}$$

$$\sin i_c = \frac{v_1}{v_2} \tag{3.2}$$

As this wave travels along the interface, energy is transmitted continuously into the upper and lower layers according to Huygens' principle, which states that every point of a wavefront can be the source of a new set of waves. Once the wave is energised at the source (TX), the geophone or receiver (RX) registers the time of the first arrivals of a certain wave: for small TX-RX distance the first arrival is the direct P-wave; at the cross-over distance, the direct wave is substituted by the critically refracted wave, also known as the head wave (Everett, 2013) (Figure 3.2).

In the following text, we assume that velocity increases with depth and that the layers are horizontal, homogeneous, parallel to each other and the surface, and thicker than the wavelength of the incident energy (Reynolds, 2011). Looking at Figure 3.1b, the function of the travel time of ray path 3 is:

$$T(x) = \frac{2h}{v_1 \cos i_c} + \frac{x - 2h \tan i_c}{v_2} \tag{3.3}$$

where the first term refers to the upward and downward portions of the ray path, and the second one to the horizontal propagation. If we consider again Snell's law for critical refraction (eq. 3.2), equation 3.3 reduces to:

$$T(x) = \frac{x}{v_2} + \frac{2h\sqrt{v_2^2 - v_1^2}}{v_1 v_2} \tag{3.4}$$

hence, refracted waves move out linearly with TX-RX separation x. T(x) has a slope of $\frac{1}{v_2}$, the direct wave moves out with a slope of $\frac{1}{v_1}$ To calculate the time, we need to extrapolate the head wave arrival back to the origin as

$$T_0 = T(0) = \frac{2h\sqrt{v_2^2 - v_1^2}}{v_1 v_2}. \tag{3.5}$$

This last equation also calculates the layer's height (Everett, 2013).

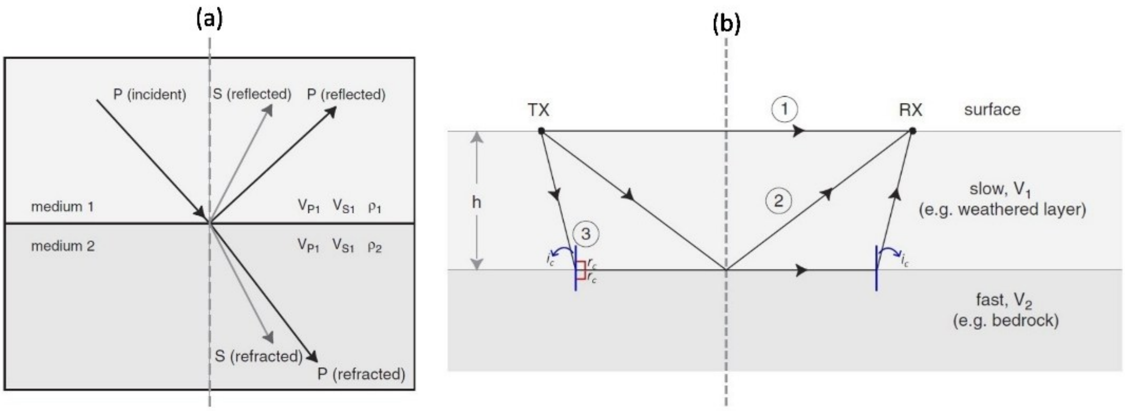

Figure 3.1: (a): P-wave reflection and refraction at an interface, including P-to-S conversion; (b): Ray paths of direct P-wave (1), reflected P-wave (2), and critically refracted P-wave (3) between seismic source (TX) and geophone (RX) (modified from Everett, 2013).

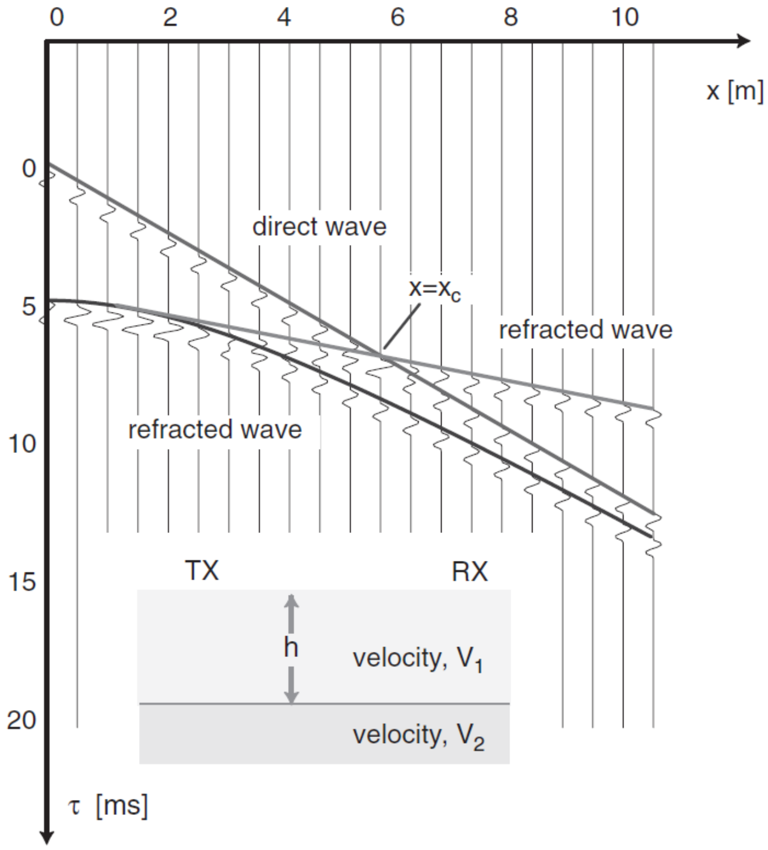

Figure 3.2: Simple case of refraction seismogram of a two-layered subsoil (Everett, 2013).

The seismic refraction method can also be used to analyse a dipping interface (dipping-layer case), a subsoil with more than two layers (multilayer case), and other geometries, such as the presence of a step and irregular interfaces. The abovementioned equations must be adjusted to the case considered (Reynolds, 2011).

3.1.1 Data acquisition

Seismic data can be acquired both offshore and onshore. Onshore acquisition may be performed either through borehole techniques or surface methods. In this chapter, only surface data acquisition on land will be considered.

Acquiring seismic data requires three main components: a seismic source, motion receivers, and a recording system. Seismic sources can be impulsive (e.g., sledgehammer) or vibratory (e.g., vibroseis). In both cases, the source must be sufficiently robust to generate short-wavelength energy and should allow for repetition to enhance the signal-to-noise ratio (Sharma, 1997).

In the case of impulsive sources, data sampling strategies depend on the positioning of the hammer and the geometry of the geophone array. The simplest configuration involves geophones evenly spaced over a flat surface. The spacing between receivers is proportional to the desired depth of investigation, where the maximum depth achievable is approximately one-third of the array length. Typically, arrays consist of twenty-four or forty-eight geophones.

The hammer can be positioned near the receivers (zero offset) or offset by one or more meters from the ends of the array. Seismic signals are recorded using a receiver unit, usually a computer equipped with appropriate acquisition software (Sharma, 1997).

In the context of this study, two seismic data acquisition campaigns were conducted in 2023 and 2024. Although only the 2024 acquisition was attended directly, the procedures followed in 2023 were reported to be similar in methodology and setup. The measurements were conducted on vegetated and bare soil, and test sites are shown in Figure 3.3.

On May 10, 2024, six different acquisitions were performed: four during low tide and two during high tide. Vertical and horizontal geophones were used during low tide to record P-waves and SH-waves (shear horizontal). In contrast, due to the expected presence of water in the subsurface, only vertical geophones were deployed during high tide. In the 2023 campaign, only vertical geophones were employed.

The survey used twenty-four geophones spaced 20 cm apart. The seismic source was a sledgehammer, and data were recorded using a Panasonic multichannel seismograph. For each configuration, three or more shots were performed, one-meter offset at the ends of the geophone array, and zero-offset every two odd geophones (Fig. 3.4). The timetable of the various acquisitions in 2024 is reported in Table 3.1.

The acquired data were subsequently processed to derive seismic velocities.

Table 3.1: Acquisition timetable and geophone setup for each soil type.

Day	Time [hours]	Tidal phase	Soil	Geophone setup
10/05/2024	10:00	low tide	Vegetated	Vertical
11/05/2024	10:30	low tide	Vegetated	Horizontal
12/05/2024	11:00	low tide	Bare	Vertical
13/05/2024	11:30	low tide	Bare	Horizontal
14/05/2024	12:00	high tide	Vegetated	Vertical
15/05/2024	12:30	high tide	Bare	Vertical

Figure 3.3: Sites of data acquisition; (a) place of interest, (b) position of the surveys on bare and vegetated soils.

Figure 3.4: Acquisition day; (a) data acquisition configuration; (b) acquisition on bare soil; (c) acquisition on vegetated soil.

3.1.2 Data processing

The first step in the seismic data processing workflow was identifying and picking the first arrivals, also known as first breaks. This process is critical, as the accuracy of the final velocity models strongly depends on the precision of the first break picking.

First breaks correspond to the first observable energy arriving at each receiver and typically represent the direct P-wave or critically refracted P-wave (or SH-wave in the case of horizontal geophones), depending on the source-receiver distance. Picking was performed manually on each seismic trace to ensure maximum accuracy, given that automatic picking algorithms sometimes fail due to low signal-to-noise ratios or complex subsurface conditions (Everett, 2013).

The picking process was done using the open-source software Front End Express 10.0 of Geogiga Technology Corporation. Each trace was normalised and picked from the normalised saved SEG-Y or SEG2 files. In Figure 3.5, one of the normalised seismographs and relative picks can be observed. The resulting picks were compiled into time–distance tables using Notepad++. Ten tables were obtained to perform the modelling process, one for each year and acquisition configuration. It is essential to understand that not every trace produced a satisfactory first pick, due to noise or because the geophone did not register any signal. Hence, all the tables were compiled without some of the picks. Nonetheless, the resulting data remained sufficient for accurate modelling.

Seismic data can be interpreted with two fundamental approaches: forward modelling or inverse modelling. In the forward case, the subsurface is modelled, with parameters such as layer thickness and seismic velocity, and the theoretical travel times of seismic waves are calculated through that model. Synthetic and observed field data are then compared, and the model is adjusted manually until the fit is satisfactory. The process is subjective and does not guarantee a unique solution. Still, it is helpful for simple geological settings or preliminary steps in more complex analysis.

Conversely, inverse modelling consists of deriving a subsurface velocity model from the observed travel time data through mathematical inversion algorithms. The model parameters are adjusted to minimise the differences between observed and calculated travel time, which can provide more objective and quantitative results (Reynolds, 2011).

In this work, the inversion process and modelling were performed using the open-source library pyGIMLi (Python Library for Inversion and Modelling in Geophysics), designed explicitly for geophysical and hydrological problems (Rücker et al., 2017).

The seismic data were modelled in two dimensions using triangular finite element cells for the mesh, with an area of 0.01, which allowed flexible representation of complex subsurface geometries. The inversion algorithm is based on a generalised Gauss-Newton approach[1], in which the solution is obtained by iteratively minimising an objective function combining data misfit and model smoothness constraints (Rücker et al., 2017).

To ensure the velocity models were geologically plausible, parameter transformations such as enforcing positivity of velocity values and smoothing (lambda) for controlled variations between adjacent cells were applied. The inversion output included the estimated velocity fields and synthetic travel time curves, which were compared with the observed data to assess model consistency and guide interpretation.

The parameters for each model are summarised in Table 3.2.

[1] The Gauss-Newton method is an iterative optimisation algorithm used to solve nonlinear inverse problems by successively updating a model to minimise the difference between observed and calculated data. It is particularly suited for seismic inversion because it converges efficiently and allows for regularisation and constraint handling (Rücker et al., 2017).

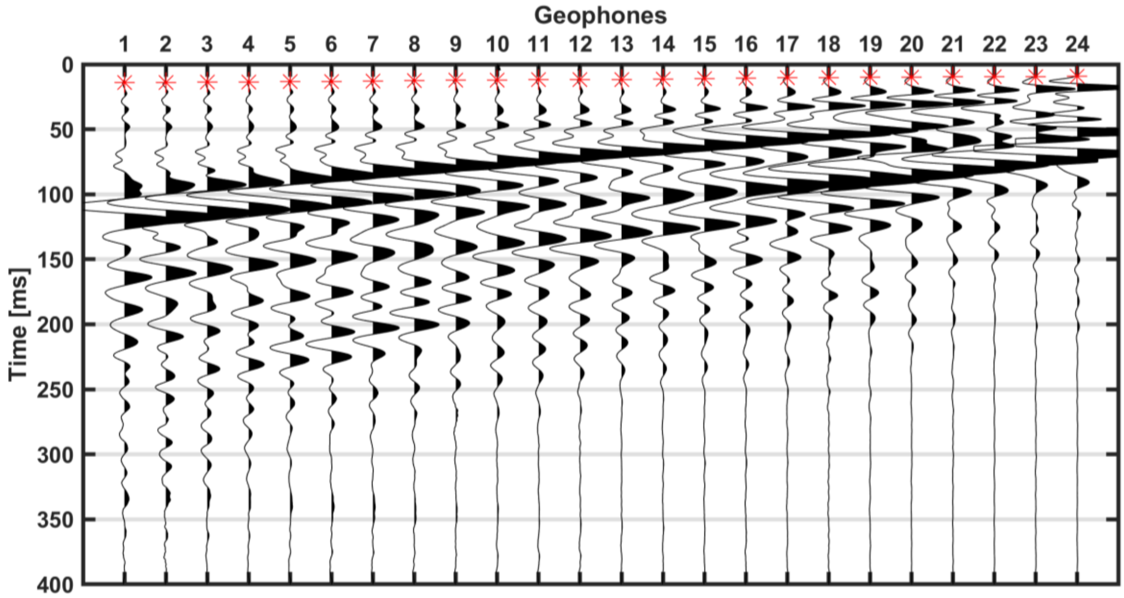

Figure 3.5: Normalised seismic traces for low-tide vegetated soil; red stars are the first break picking of each trace.

Table 3.2: Velocity model parameters; BareVert is the name given to unvegetated soil with vertical geophones setup; VegVert stands for vegetated soil with vertical geophones setup; VegHor and BareHor are the names for vegetated and bare soils with horizontal geophones setup.

Datasets			Error [s]	Vtop [m/s]	Vbottom [m/s]	Lamba
2023	lowtide	VegVert	0.00045	50	1000	50
		BareVert	0.0005	50	1000	50
	hightide	VegVert	0.00065	50	1000	50
		BareVert	0.00055	50	1000	50
2024	lowtide	VegVert	0.00035	50	1000	50
		VegHor	0.0017	20	100	50
		BareVert	0.0003	50	1000	50
		BareHor	0.0008	20	100	50
	hightide	VegVert	0.0004	50	1000	50
		BareVert	0.00045	50	1000	50

3.2 Remote Sensing

For this work, Google Earth Pro was used to visualise and sample geographical data, while QGIS was used to analyse geospatial information. Google Earth Pro is an intuitive platform that provides access to high-resolution satellite imagery and geographic data;

QGIS is a powerful open-source Geographic Information System (GIS) designed for elaborating, analysing, and representing complex spatial datasets. Integrating both tools was necessary because Google Earth Pro enabled quick and visual access to geospatial information, while QGIS allowed for advanced spatial analyses. Importantly, both platforms are open-source and supported by extensive documentation.

3.2.1 Data sampling with Google Earth Pro

Google Earth Pro is a geospatial application developed by Google that allows users to visualise satellite imagery, maps, and geographic data in a three-dimensional interactive environment. Initially intended for professional use, it is now freely available and serves as a versatile tool for geospatial exploration and analysis (Wikipedia, 2025).

Google Earth Pro integrates satellite imagery from remote sensing, aerial photographs, and topographical data to generate virtual representations of the Earth (and, in some cases, other planetary bodies). It allows for visualising high-resolution aerial and satellite images in three dimensions. Additional functionalities include importing external data formats such as KML/KMZ files and shapefiles, tools for measuring distances and areas, and time-series visualisation using historical imagery (dating back to 1985).

The coordinate reference system used in Google Earth Pro is WGS 84 (EPSG:4326), which employs geographic coordinates (latitude and longitude) (Google LLC, 2024).

For this study, Google Earth Pro was used to delineate the San Felice salt marsh polygon and the boundaries of its main channels between 2004 and 2024. The channels included in the analysis are the Gaggian Channel, the San Felice Channel, an artificial channel, and the one where the seismic refraction surveys were conducted. Additionally, twenty reflectors were identified each year to calculate displacement errors over time (Fig. 3.6; see Table 3.3).

Due to insufficient data or excessive georeferencing error, not all twenty years within the study period were retained for subsequent analysis.

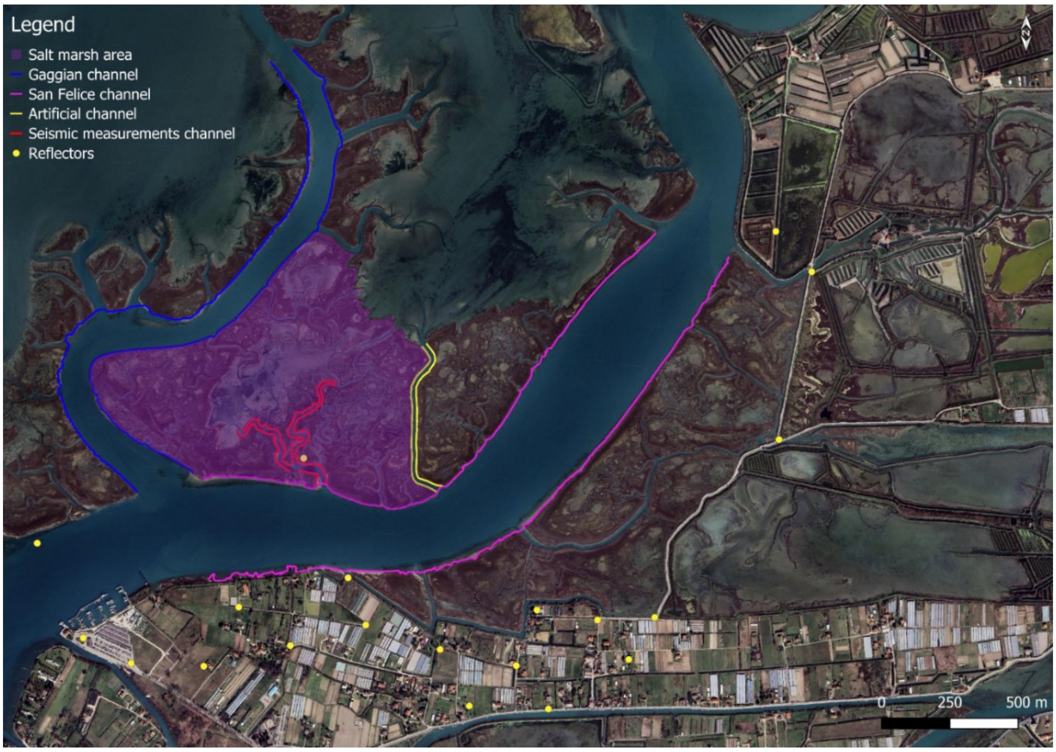

Figure 3.5: Channel boundaries, area of the San Felice salt marsh and position of the twenty reflectors (2023).

Table 3.3: Attributes of the satellite remote sensing datasets used in the study.

Year	Type	Sensing Date
2004	Satellite image	31 July
2005	Satellite image	8 June
2006	Satellite image	13 September
2007	Satellite image	22 September
2008	Absent data	
2009		
2010		
2011		
2012		
2013		
2014	Satellite image	14 March
2016	Satellite image	28 June
2017	Satellite image	26 June
2018	Satellite image	2 April
2019	Satellite image	5 September
2021	Satellite image	25 March
2023	Satellite image	21 March
2024	Satellite image	12 April

3.2.2 Data processing with QGIS

QGIS is open-source software for managing, analysing, and visualising geospatial data. Initially developed in 2002 under the name Quantum GIS, it has grown through contributions from a global community of developers and users. Today, QGIS is one of the most widely used geographic information systems in professional and academic settings. Its versatility lies in its ability to support various vector and raster formats and spatial databases.

QGIS allows users to visualise, overlay, and analyse various spatial data types using a comprehensive set of built-in tools and an extensive plugins library that extends its core functionality. Notably, the *Processing Toolbox* enables advanced operations such as raster georeferencing, elevation modelling, and spatial data transformation (QGIS Development Team, 2024).

All geospatial analyses in this study were conducted using the Monte Mario Italy 2 (EPSG:3004) projected coordinate system to ensure consistency across datasets. Additionally, upon export to shapefile format, all vector layers—polygonal, linear, and point-based—were treated as 2D (planar), excluding altitude information.

QGIS was employed to process remote sensing data of the San Felice salt marsh. Specifically, polygonal datasets representing the marsh area from 2004 to 2024 were imported after conversion from KMZ to shapefile format. The *Field Calculator* tool was used to compute square metres (m^2) surface areas, enabling systematic quantification of spatial changes throughout the observation period. All calculated values were exported to Excel for further processing.

The previously identified twenty reflectors were analysed via distance comparison to assess georeferencing accuracy. These reference points were imported as KMZ files and subsequently converted into shapefiles. Using the *Distance Matrix* tool, Euclidean distances between matching reflectors across different years were calculated. These values provided estimates of positional displacement, interpreted as proxies for georeferencing uncertainty. Year pairs showing excessive reflector displacement or poor data quality were excluded from subsequent analyses to ensure the robustness of the final dataset (see Table 3.4).

Based on the Dynamic Time Warping (DTW) algorithm, the Channel Migration plugin was used to quantify annual changes in canal bank geometry for channel migration analysis. The tool aligns channel boundaries across consecutive years and calculates migration vectors accordingly. The following key parameters were defined:

- Years: Time interval (in years) between compared datasets.
- Spar: Smoothing parameter for spline interpolation; zero indicates no smoothing.
- Curvature multiplier: Scales the influence of curvature differences relative to spatial displacements.
- Step pattern: Defines DTW constraints by limiting the allowed alignment steps.
- Step: Specifies how frequently migration vectors are computed along the channel boundary.

Using these settings, the plugin analysed canal bank shapefiles—derived initially from KMZ inputs—and computed migration rates for each consecutive year pair (e.g., 2007–2014, 2017–2018, etc.). As with the distance analysis, years affected by excessive displacement or inconsistencies were excluded to ensure data integrity. The parameters are the same for each year and riverbank: the spar used is 0.4, the curvature multiplier is 1.0, the step pattern is symmetricP05, and the step is 2 m.

The migration values obtained for each riverbank segment and the calculated marsh surface areas for each year were exported to Excel for subsequent analysis. The migration rate was calculated as the distance divided by the years between observations. This allowed for the aggregation, comparison, and visualisation of both areal and linear changes across different time intervals.

Table 3.4: Reflector displacements for each year pair. Selected pairs used for analysis are shown in bold, with mean and standard deviation values highlighted in yellow.

REFLECTORS	DISTANCE													
	2004-2005	2005-2006	2006-2007	**2007-2014**	2014-2016	2016-2017	**2017-2018**	**2018-2019**	**2019-2021**	2021-2023	2023-2024	**2014-2017**	**2021-2024**	**2007-2024**
1	6.626813	7.44392	2.942482	1.267605	-	3.368927	0.597501	0.930366	0.919147	4.875034	5.141574	-	1.345742	-
2	13.15305	7.984244	4.664994	1.396496	4.478024	4.758723	1.136656	0.358372	0.492629	6.045234	6.962569	1.323798	4.548576	3.532736
3	7.845671	7.388785	3.544435	1.501867	4.511947	4.4314	0.394597	1.169434	0.884007	4.525742	4.490782	0.698766	1.083376	1.731911
4	7.679979	7.707319	2.60044	1.502499	4.352192	4.204561	0.935441	1.570486	1.061106	5.019953	5.176898	1.075126	1.518602	1.694706
5	7.457717	8.08714	3.327492	1.404878	4.03391	3.977781	0.972595	1.34882	0.917529	4.535717	4.429535	1.094022	0.927084	1.218793
6	8.524608	13.13043	3.240512	2.319584	2.822889	2.616615	1.282757	1.965876	1.32011	5.017164	4.332831	2.475576	0.940962	1.293652
7	7.143321	8.531193	4.186817	0.647158	4.098487	4.217274	0.32603	2.786414	2.433861	5.087998	2.609786	0.324381	2.478646	2.3189
8	4.982314	4.664553	3.291371	1.313861	2.229533	3.47986	1.549061	0.436977	2.699547	4.562979	5.813131	1.422856	1.260625	0.773476
9	6.500941	7.50207	3.575457	0.603591	4.716424	5.686202	0.969977	0.850862	0.340759	4.479271	4.313362	0.969977	0.731822	0.170485
10	7.036936	8.597133	2.579339	2.584816	3.891637	4.485372	0.321002	0.985354	0.717452	4.747901	4.491421	1.301471	0.8531	2.222075
11	5.664767	7.875117	2.703764	1.0326	2.607021	3.243476	0.186569	1.121928	1.457728	2.958905	4.42894	0.898843	1.720407	0.902165
12	6.867303	6.428357	3.462732	2.148281	4.330793	4.140751	0.67387	0.558767	1.388838	3.884872	2.537268	1.928608	1.420571	3.148366
13	6.636706	7.840842	3.108836	1.452782	3.995001	4.643358	0.529131	1.251988	0.911258	5.225249	4.704444	0.916796	0.704961	1.793018
14	7.071761	7.719546	2.443862	2.147196	2.291565	2.531801	0.647309	1.225458	1.277807	4.607602	5.056531	1.364119	1.25795	1.87286
15	6.079478	3.06907	2.055394	2.989472	3.506918	2.982419	0.838442	1.483947	1.118782	4.531578	5.228568	2.21712	1.927439	1.968729
16	8.089365	8.835726	4.003373	1.48821	3.685681	3.755239	0.519572	1.350875	1.044652	4.967164	4.674593	1.177439	0.929893	1.303212
17	6.973667	7.838372	2.609563	1.055766	4.022	4.451873	0.175961	0.941808	0.710731	4.55551	4.376202	0.503193	0.78484	1.589809
18	5.827394	6.893625	2.300404	1.254157	3.875922	3.803683	0.731423	1.188775	0.577504	4.551036	4.406303	1.058432	0.716164	0.618505
19	9.482691	10.33336	5.016114	4.882193	3.463301	4.733265	3.017233	1.098123	0.975615	4.749418	8.352739	3.478697	5.630808	1.310286
20	9.841121	10.23501	3.5624	4.344309	4.266784	4.562905	2.581658	1.679056	1.244925	5.313123	8.076127	3.376847	3.802848	2.232186
MEAN	7.47428	7.90529	3.260989	1.866866	3.746317	4.003774	0.919339	1.215184	1.124699	4.712073	4.98018	1.452951	1.729221	1.668204
S.D.	1.793806	2.02903	0.780716	1.120659	1.111345	0.790295	0.740294	0.543909	0.576874	0.599099	1.453024	0.875113	1.373641	0.884189

3.3 Wind Wave-Tidal Model

Note to the reader: This chapter presents the combined wind wave-tidal model originally developed by Carniello et al. (2005, 2011). Please note that I have not developed or executed the model myself; the outputs were generated by an external party and provided for analysis. My contribution here is limited to visualising, compiling, and interpreting these results (via MATLAB).

The numerical model developed by Carniello et al. (2005) (and further improved in Carniello et al., 2011) combines wind waves with tidal fluxes in a tidal basin, like the Venice Lagoon. The hydrodynamic and wave components' calculations are on the same triangular mesh (with 52000 nodes and 98000 triangular elements), a fundamental aspect of accurately reproducing the system's geometric complexity.

The model is divided into two main modules: the tidal and wind wave modules. The hydrodynamic model solves the two-dimensional shallow water equations and includes a sub-grid modelling of the most recent bathymetry (2003) to deal with flooding and drying processes in irregular domains (Carniello et al., 2005, 2011). The model utilises a semi-implicit staggered finite difference discretisation to be coupled with the wind-wave model to assess wave group velocity and bottom influence on wave propagation. The wind wave model is based on conserving the wave action, resolving a simplified version of the Hasselmann (1973) spectral formulation. Nonetheless, the model uses a monochromatic approach to obtain computational efficiency for long-term morphodynamic studies. This means that some spectro-temporal complications (such as lateral energy diffusion) are avoided, and only one dominant frequency is adopted. In this case, the dispersion is a semi-empirical relationship that couples the local wave period and wind velocity with depth.

The transfer from wind energy to waves is modelled in two phases: linear energy input, where the energy is expressed as a function of wind velocity and local turbulence measurements, and exponential growth from perturbation feedback, where once the water surface is disturbed, the wind flow field over it is disturbed, causing a greater transfer of energy (Carniello et al., 2005).

There are different mechanisms for wave energy dissipation: bottom friction, white capping, and depth-induced breaking. Bottom friction (including dissipation through percolation, friction, motion of the soft muddy bottom, and bottom scattering) is the most important mechanism. White capping couples the dissipated energy with the steepness of waves. In depth-induced breaking, the maximum wave height is a function of depth. The dissipation by breaking is divided into two different parts. A first dissipation (boundary breaking) occurs at the boundary between the deeper and the shallower element; the second dissipation (element breaking) gradually develops in the downstream computational element. This makes it possible to separate the energy dissipated because of a sudden variation of bathymetry from the continuously occurring dissipation over horizontal or gently sloping bottom surfaces (Carniello et al., 2005).

The model enlightens the importance of the relationship between wave and tidal fields. Waves modify the water level and influence the residual circulation. The wave field directly affects the value of the bottom shear stress, which is higher in the presence of waves than in the absence of waves (currents only). Finally, the model assumes an immediate alignment between wind and wave direction (neglecting refraction and diffraction phenomena), justified by experimental studies in enclosed basins and the rapid decay of waves without wind (Carniello et al., 2005, 2011).

The model has been rigorously validated by correlating its outputs with observational data collected from multiple monitoring stations throughout the Venice Lagoon, thereby confirming its excellent performance and validity.

Figure 3.6 shows the two geographical points where the model was run. The water level, wave height and total bottom shear stress for both investigated points are presented for 2020-2023 and May 2024. For each parameter, the model gave a solution for every half hour of every day of every year.

Figure 3.6: Locations where the hydrodynamic model was run, (1) is in the channel where seismic measurements were conducted, and (2) is in the San Felice Channel.

3.4 Soil Core Analysis

Detailed soil analyses of salt marshes are essential for understanding how the vertical distribution of soil matter captured in sediment cores offers key insights into the long-term accretion processes and marshes' capacity to sequester carbon, often referred to as “blue carbon” (Puppin et al., 2025). Studies such as Roner et al. (2015) and Puppin et al. (2025) have demonstrated that variations in both organic and inorganic deposition across different depositional environments critically influence the carbon (hence, organic matter) storage potential and structural evolution of coastal wetlands. By accurately measuring parameters like water content, organic matter content via loss-on-ignition (LOI) and chemical treatments, and grain size distribution, it is possible to quantify the contributions of both autochthonous and allochthonous inputs. This information helps understand the present-day sedimentary processes, reconstruct the depositional history, and assess changes in relative sea level and hydrodynamic conditions over time. Ultimately, such analyses are essential for predicting marsh resilience under future climate change scenarios, guiding coastal management strategies to mitigate greenhouse gas emissions through wetland preservation and restoration initiatives (Kolker et al., 2009; Runer et al., 2015; Puppin et al., 2025).

3.4.1 Field sampling

Note to the reader: The soil core samples presented in this chapter were collected by external collaborators on 26th April 2025 in the area where high-resolution seismic refraction analyses were conducted during the 2023 and 2024 campaigns. Although I did not participate in the fieldwork or collect the cores directly, my contribution involved processing, analysing, and visually representing these samples to evaluate the soil's depositional and organic matter characteristics in the San Felice salt marsh.

Four 1-metre-long undisturbed soil cores were collected from the study area: two from vegetated zones and two from non-vegetated areas. Figure 3.7 represents the approximate sampling positions. Once collected, the samples were stored in refrigerators for further processing.

3.4.2 Laboratory Processing

The procedure applied to each core sample is based on the works of Kolker et al. (2009), Roner et al. (2015), and Puppin et al. (2025).

The first step was core splitting and sub-sampling. Each core was halved longitudinally. A slice 2.5 cm thick was taken from the top of one half of each. Subsequent sub-samples were collected every 5 cm from 2.5 to 52.5 cm, with additional 5 cm slices taken from the 67.5-72.5 cm interval and again from the 87.5-92.5 cm interval. The intact half of each core was then photographed (Figure 3.8). The freshly extracted (wet) samples were weighed immediately to record their raw mass on an analytical balance.

Secondly, all sub-samples were placed in an oven at 60°C for 48 hours to dry them out. After drying, the sub-samples were weighted again. The difference between the wet and the dry weight was used to calculate the water content (WC) as:

$$WC = \frac{W_{wet} - W_{dry}}{W_{dry}} \quad (3.6)$$

where W_{wet} is the weight of the raw sample and W_{dry} is the weight of the sample after drying.

As a third step, the dried sub-samples were ground into a fine powder and transferred individually into crucibles. For each depth (except the top 2.5 cm sample, which was entirely utilised), only half of the powdered sample was used for further analysis. Each sample was weighed again on an analytical balance fitted with draft shields. The prepared samples in the crucibles were then placed in a muffle furnace and heated to 375°C for 16 hours to combust the organic matter (Puppin et al., 2025).

After combustion, the samples were cooled at room temperature in a vacuum container and then re-weighed on the analytical balance with draft shields. The loss in weight (loss on ignition, LOI) served as an estimate of the organic matter content with:

$$LOI = \frac{W_{dry} - W_{ash}}{W_{dry}} \quad (3.7)$$

where, W_{ash} is the weight of the sample after the muffle treatment.

The results were visualised using MATLAB.

Figure 3.7: Approximate position of the four core samplings: 1 non-vegetated, and 2 vegetated in the area of 2024 seismic measurements; 3 non-vegetated, and 4 vegetated in the area of 2023 seismic measurements.

Figure 3.8: Core samples slices. From bottom to top: 1, 2, 3, 4 refer to where the core was collected.

4 RESULTS

4.1 Seismic Refraction

Following the acquisition and processing of the seismic refraction data, ten velocity models were obtained - four from the 2023 campaign and six from the 2024 campaign. The 2024 dataset includes both P-wave and SH-wave models, while in 2023, only P-wave acquisitions were performed. These models, derived through the inversion of manually picked first arrivals, illustrate the distribution of seismic velocities in the shallow subsurface along the geophone array.

The resulting models allow for a comparative analysis of the soil's physical properties under different surface conditions (vegetated versus non-vegetated) and tidal phases (low versus high tide). Interpreting these models provides insight into the mechanical behaviour of the shallow subsurface, with particular attention to the influence of vegetation and water content on seismic velocities.

The geophone array consisted of 24 sensors spaced at 20 cm intervals, resulting in a total length of 4.8 m. In seismic refraction surveys, the maximum depth of investigation is approximately one-third of the total array length, depending on the source-receiver geometry and wave propagation conditions (Reynolds, 2011). Thus, the models obtained in this study image the subsurface to a depth of approximately:

$$z_{max} \approx \frac{L}{3} = \frac{4.8\ m}{3} \approx 1.6\ m. \tag{4.1}$$

The reliability of the inversion results depends not only on the accuracy of the picked travel times but also on the error estimate introduced at the beginning of the modelling process. This error value is used to weight the importance of the data misfit during the inversion and directly affects the value of the chi-squared (χ^2) misfit statistic, which measures how well the synthetic travel times fit the observed ones, relative to the assumed uncertainty. Ideally, χ^2 should be close to 1: a $\chi^2 \ll 1$ suggests that the model may be overfitting the data, often due to an overestimated error or excessive regularisation; in contrast, a $\chi^2 \gg 1$ implies that the model does not adequately fit the data, which may be due to underestimated error values or poor initial picks (Rücker et al., 2017).

To assess the reliability of the inversion results, both the dromocrones (the curves representing the travel times of seismic waves) of the picked first arrivals and the synthetic travel times computed from the inverted models are presented alongside the corresponding velocity models (Figures 4.1-4.15).

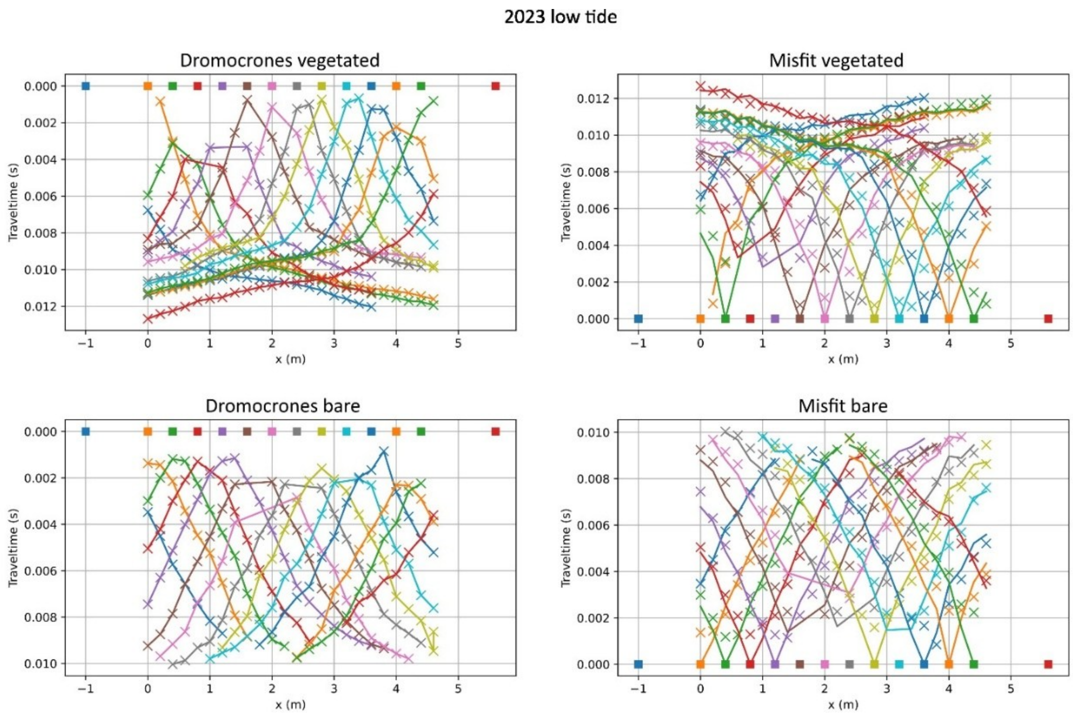

Figure 4.1: Dromocrones and data misfit for 2023 vegetated and non-vegetated during low tide. In the misfit images, crosses represent the manually picked first arrivals, solid lines the modelled travel times.

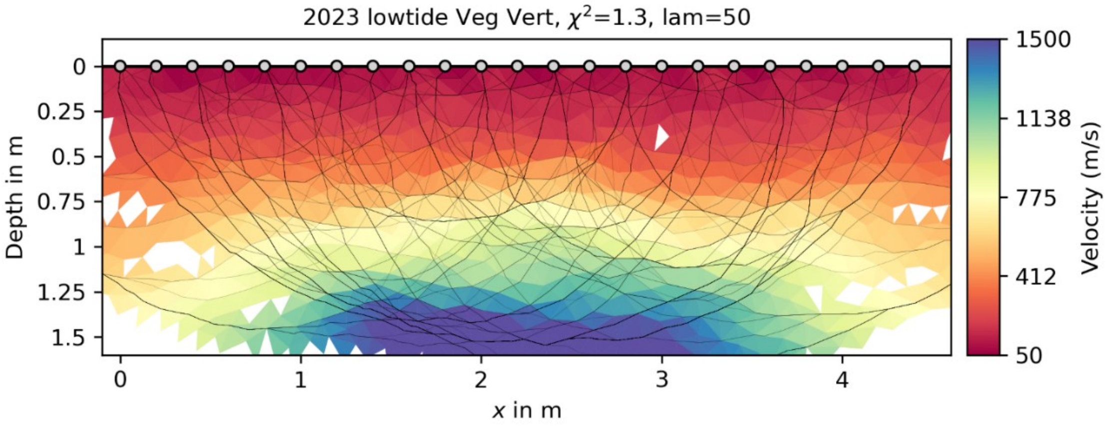

Figure 4.2: P-wave seismic velocity model of vegetated soil at low tide (2023). The model shows velocity variations with depth, with χ^2=1.3 and λ=50. Grey dots indicate geophone positions, and black solid lines represent the ray paths. On the right is the velocity scale in m/s.

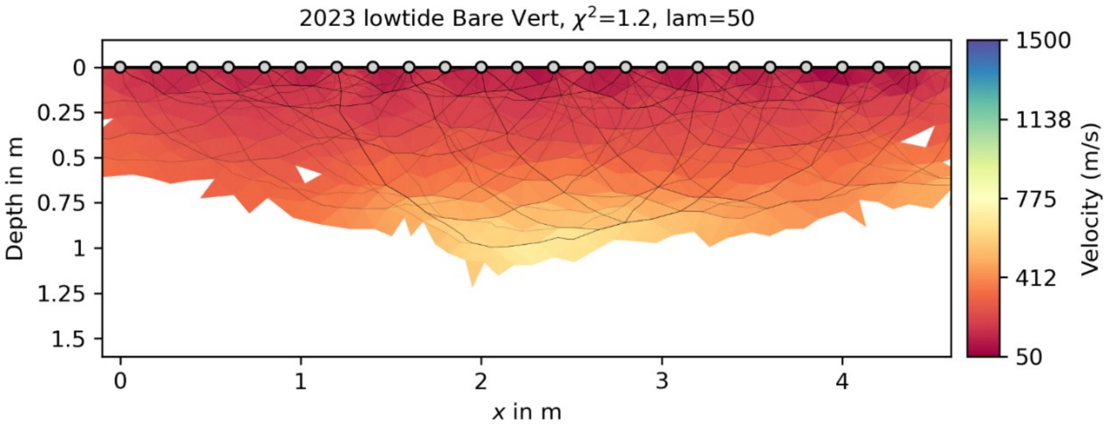

Figure 4.3: P-wave seismic velocity model of non-vegetated soil at low tide (2023). The model shows velocity variations with depth, with χ^2=1.2 and λ=50. Grey dots indicate geophone positions, and black solid lines represent the ray paths. On the right is the velocity scale in m/s.

Figure 4.1 shows the dromocrones and corresponding misfits for vegetated and non-vegetated soils at low tide in 2023. In the vegetated case, the dromocrones show two different trends: a steeper increase within the first 0.008 s and a more gradual one towards 0.012 s. In the bare soil, the curves show a steep trend across the entire time window. The misfit panel reflects these patterns and shows the differences between observed and modelled arrivals. Even if the first picks and the modelled travel times do not always correspond, the model is still considered valid for assessing the velocity of the subsurface since the differences fall into the millisecond (10^{-3} s) range.

Figure 4.2 shows the velocity model of the vegetated soil, while Figure 4.3 shows the velocity model of the bare soil in the low tide case. Comparing the two images, it is possible to affirm that the vegetated soil has a higher wave velocity propagation overall than the bare soil.

During picking the first arrival for the bare case, it is important to report that the amplitude of these signals was low. Unfortunately, only 198 picks were reported on pyGIMLi for the inversion process, against the 306 for the vegetated case. This might have caused the absence of information at a depth lower than 1 metre. This was probably due to the poor mechanical coupling between the geophones and the soil.

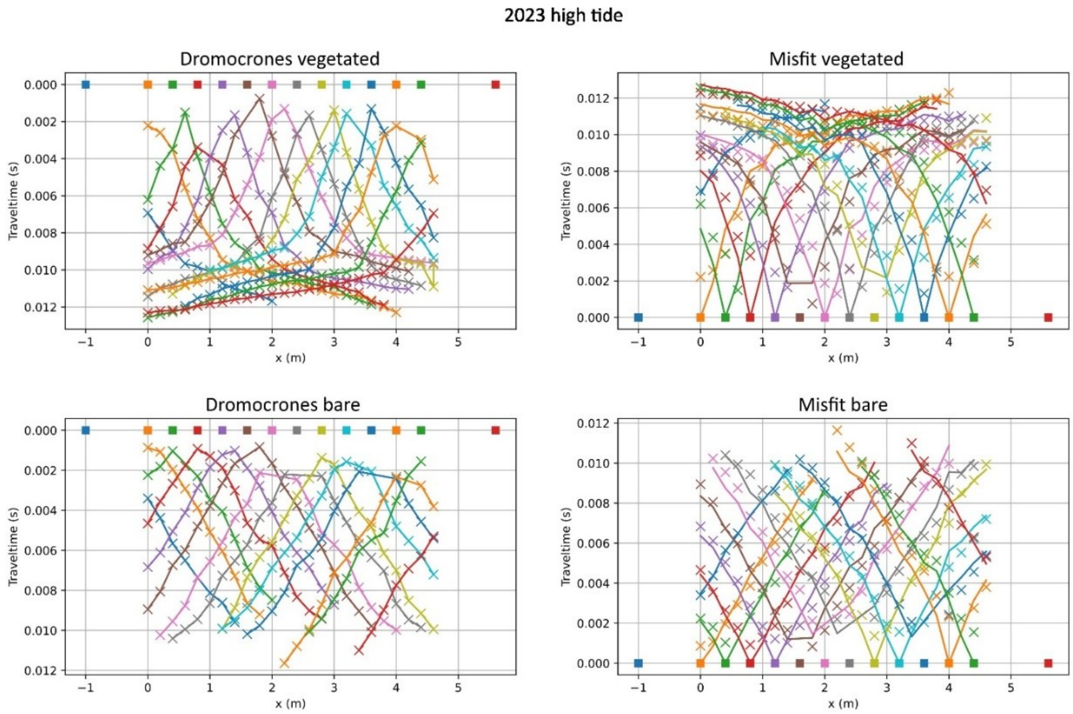

Figure 4.4: Dromocrones and data misfit for 2023 vegetated and non-vegetated during high tide. In the misfit images, crosses represent the manually picked first arrivals, solid lines the modelled travel times.

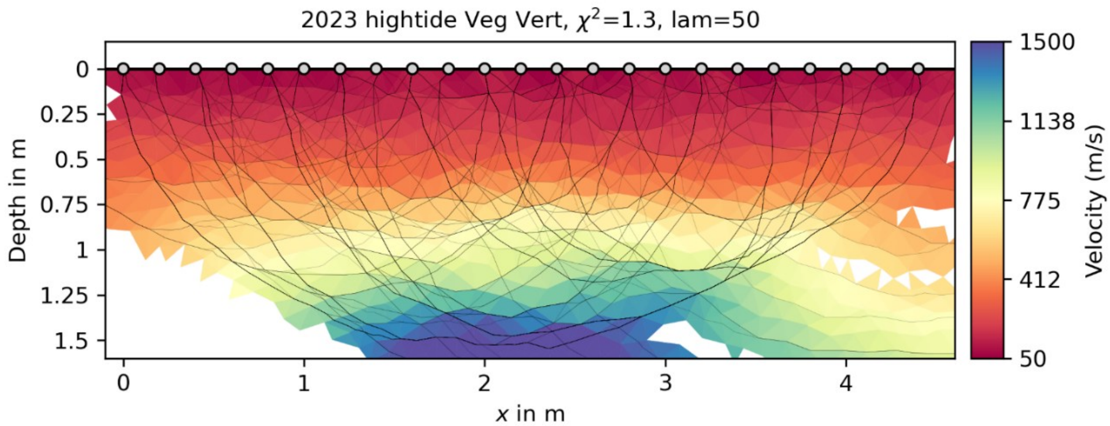

Figure 4.5: P-wave seismic velocity model of vegetated soil at high tide (2023). The model shows velocity variations with depth, with χ^2=1.3 and λ=50. Grey dots indicate geophone positions, and black solid lines represent the ray paths. On the right is the velocity scale in m/s.

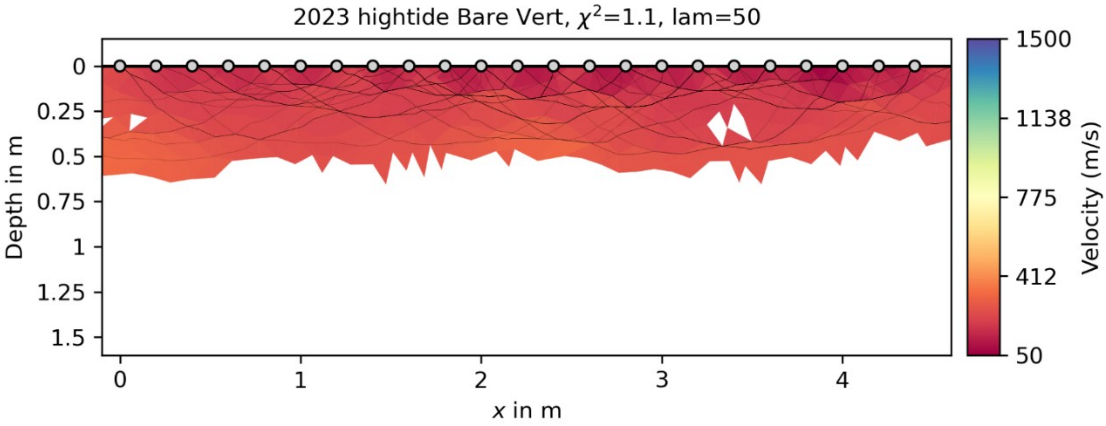

Figure 4.6: P-wave seismic velocity model of non-vegetated soil at high tide (2023). The model shows velocity variations with depth, with χ^2=1.1 and λ=50. Grey dots indicate geophone positions, and black solid lines represent the ray paths. On the right is the velocity scale in m/s.

Still for 2023 measurements, Figure 4.4 shows a similar behaviour to Figure 4.1 during high tide. Similar to the low tide case, Figure 4.5 shows that the wave propagation velocity increases with depth during high tide. Comparing the two tidal phases, the vegetated soil during high tide has a slightly lower wave propagation velocity than during low tide at a depth of 1.25 m.

Figure 4.6 shows the velocity model of the bare soil during high tide. Again, the information is inconclusive due to poor picking.

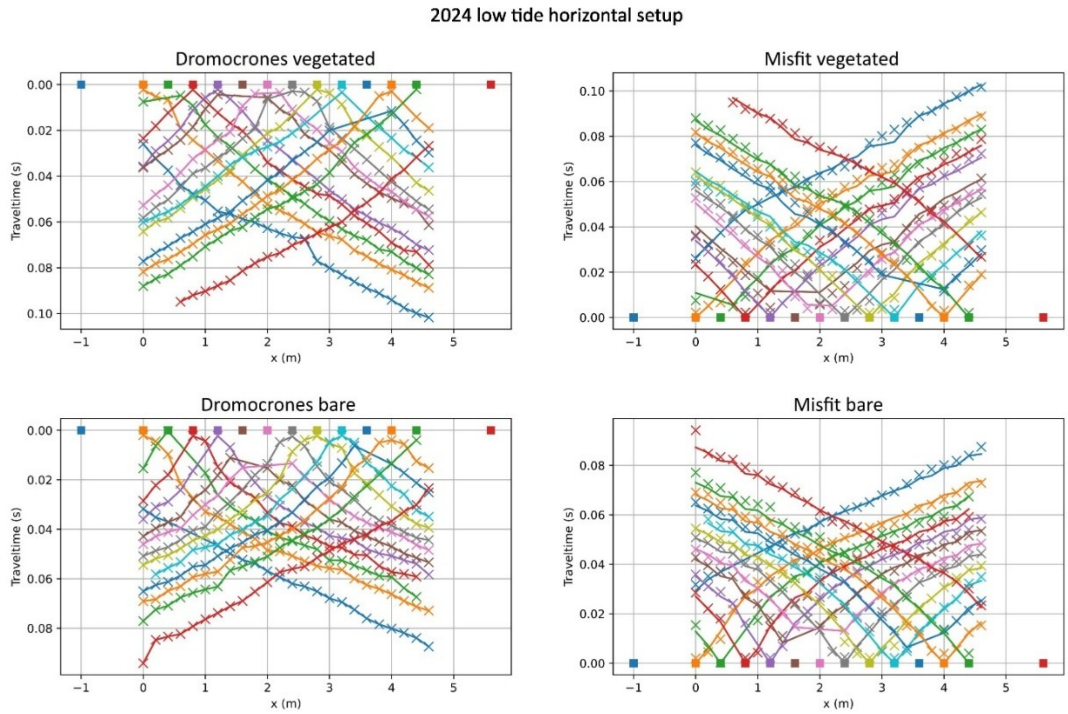

Figure 4.7: Dromocrones and data misfit for 2024 vegetated and non-vegetated during low tide, horizontal geophones setup. In the misfit images, crosses represent the manually picked first arrivals, solid lines the modelled travel times.

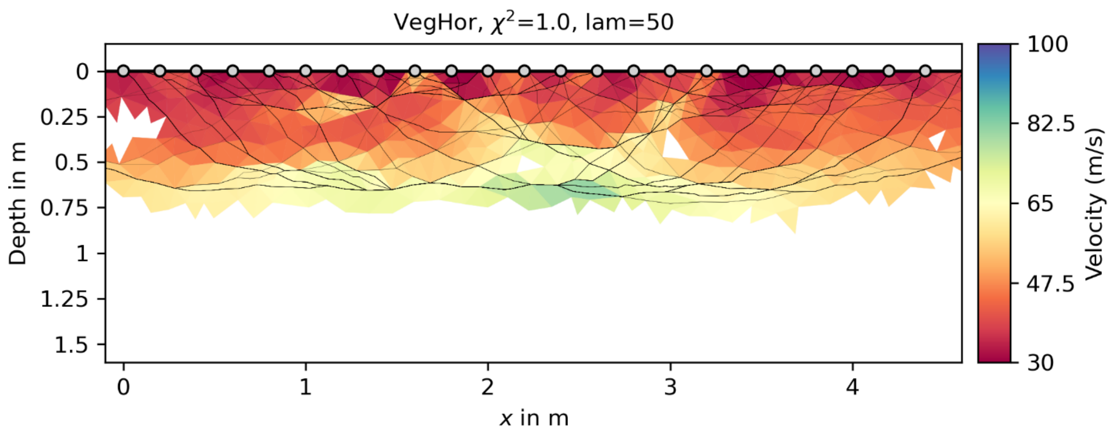

Figure 4.8: SH-wave seismic velocity model of vegetated soil at low tide (2024). The model shows velocity variations with depth, with χ^2=1.0 and λ=50. Grey dots indicate geophone positions, and black solid lines represent the ray paths. On the right is the velocity scale in m/s.

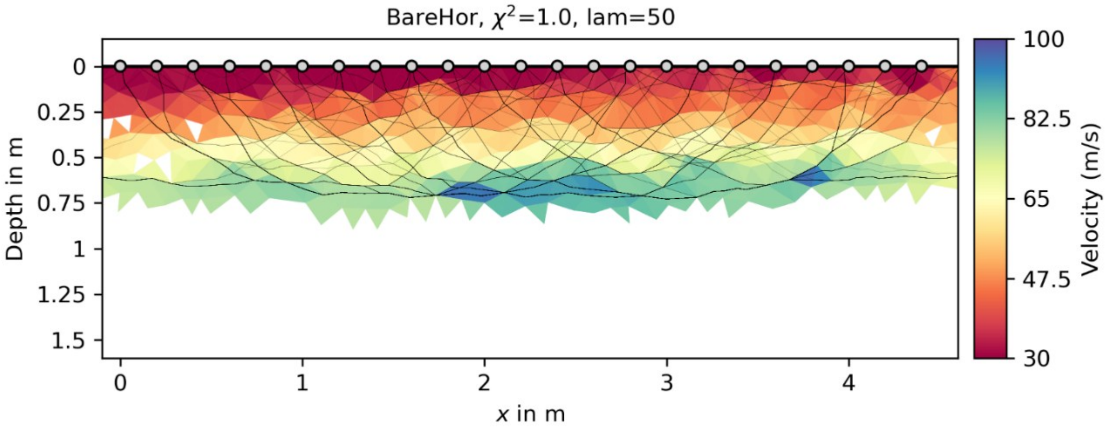

Figure 4.9: SH-wave seismic velocity model of non-vegetated soil at low tide (2024). The model shows velocity variations with depth, with χ^2=1.0 and λ=50. Grey dots indicate geophone positions, and black solid lines represent the ray paths. On the right is the velocity scale in m/s.

Figure 4.7 shows the dromocrones and corresponding misfits for vegetated and non-vegetated soils at low tide in 2024 for the case of horizontal geophones. The dromocrones show a steep trend across the entire time window in vegetated and bare soil cases. The misfit panel reflects these patterns and shows the differences between observed and modelled arrivals. The coupling between picked first arrivals and modelled travel time is satisfactory.

Figure 4.8 shows the velocity model of the vegetated soil, while Figure 4.9 shows the velocity model of the bare soil in the low tide and horizontal geophone case. Comparing the two images, the vegetated soil appears to have a lower wave velocity propagation at a depth of 0.75 m than the bare soil.

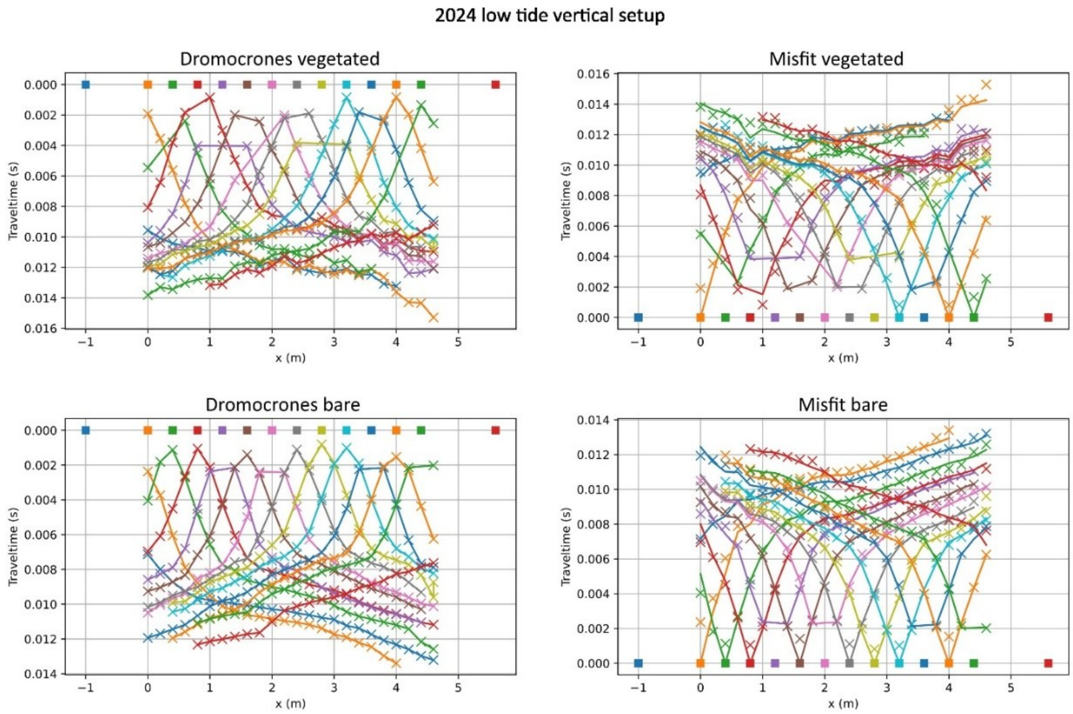

Figure 4.10: Dromocrones and data misfit for 2024 vegetated and non-vegetated during low tide, vertical geophones setup. In the misfit images, crosses represent the manually picked first arrivals, solid lines the modelled travel times.

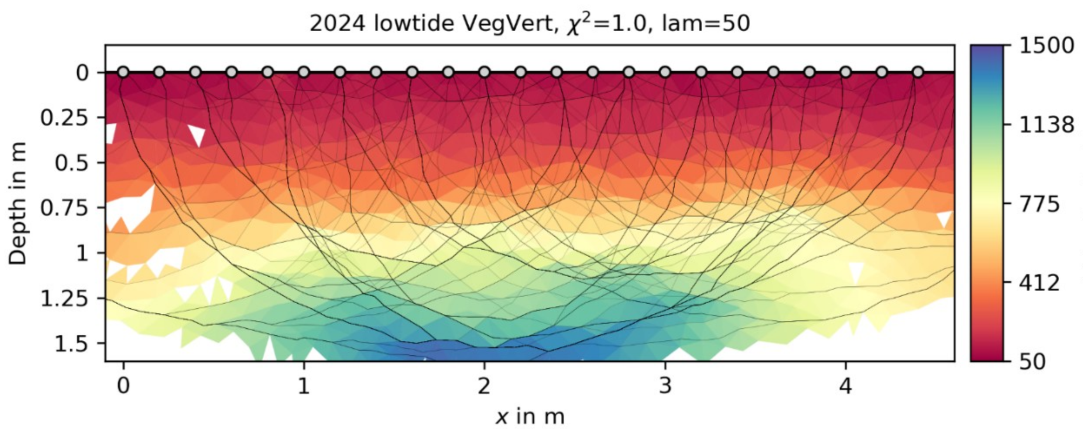

Figure 4.11: P-wave seismic velocity model of vegetated soil at low tide (2024). The model shows velocity variations with depth, with χ^2=1.0 and λ=50. Grey dots indicate geophone positions, and black solid lines represent the ray paths. On the right is the velocity scale in m/s.

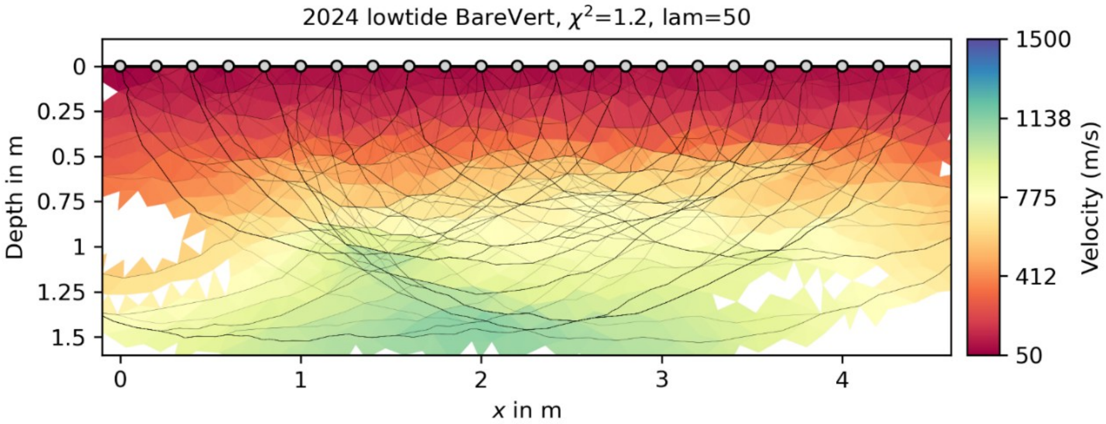

Figure 4.12: P-wave seismic velocity model of non-vegetated soil at low tide (2024). The model shows velocity variations with depth, with χ^2=1.2 and λ=50. Grey dots indicate geophone positions, and black solid lines represent the ray paths. On the right is the velocity scale in m/s.

Figure 4.10 shows the dromocrones and corresponding misfits for vegetated and non-vegetated soils at low tide in 2024 for the case of vertical geophones. In both the vegetated and bare soil cases, the dromocrones show two trends: a steeper increase within the first 0.008 s and a more gradual one towards 0.014 s. In the bare soil, the curves show a steeper trend than in the vegetated one. The misfit panel reflects these patterns and shows the differences between observed and modelled arrivals. Also, the coupling between picked and modelled travel times is adequate.

Figure 4.11 shows the velocity model of the vegetated soil, while Figure 4.12 shows the velocity model of the bare soil in the low tide case. Comparing the two images, it is possible to affirm that the bare soil has a higher wave propagation velocity than the vegetated soil in the first metre. In comparison, the vegetated soil has a higher wave propagation velocity at lower depths.

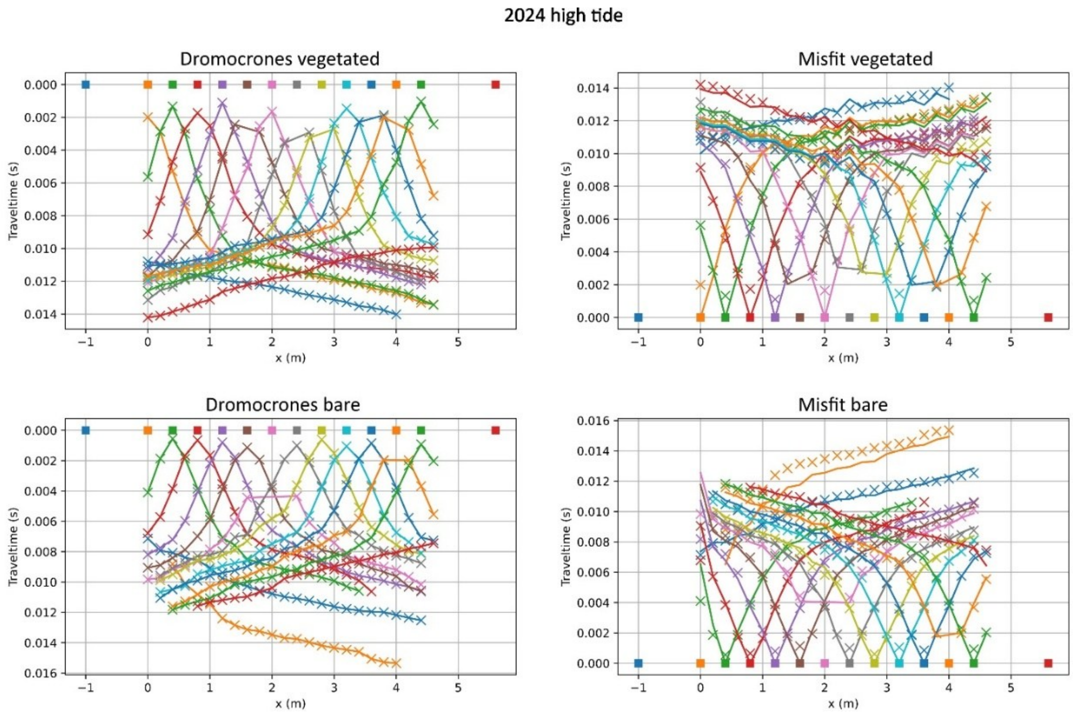

Figure 4.13: Dromocrones and data misfit for 2024 vegetated and non-vegetated during high tide. In the misfit images, crosses represent the manually picked first arrivals, solid lines the modelled travel times.

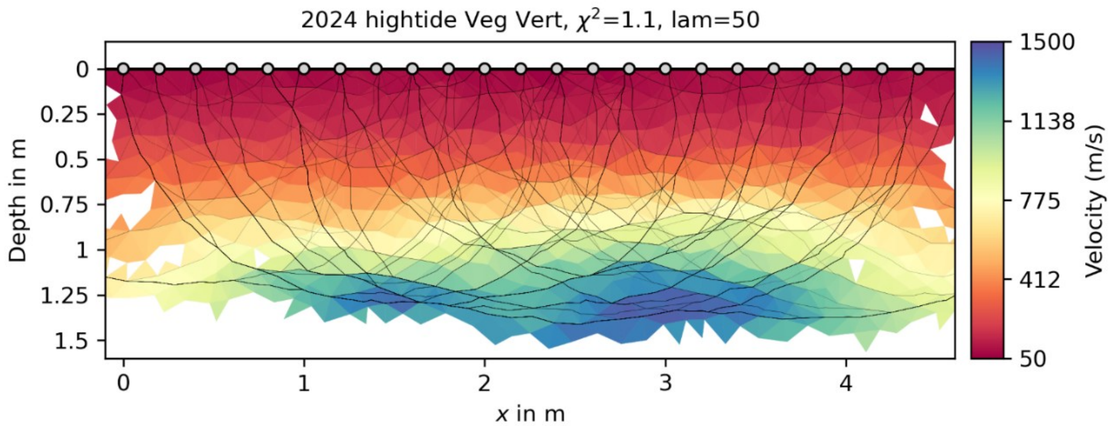

Figure 4.14: P-wave seismic velocity model of vegetated soil at high tide (2024). The model shows velocity variations with depth, with χ^2=1.1 and λ=50. Grey dots indicate geophone positions, and black solid lines represent the ray paths. On the right is the velocity scale in m/s.

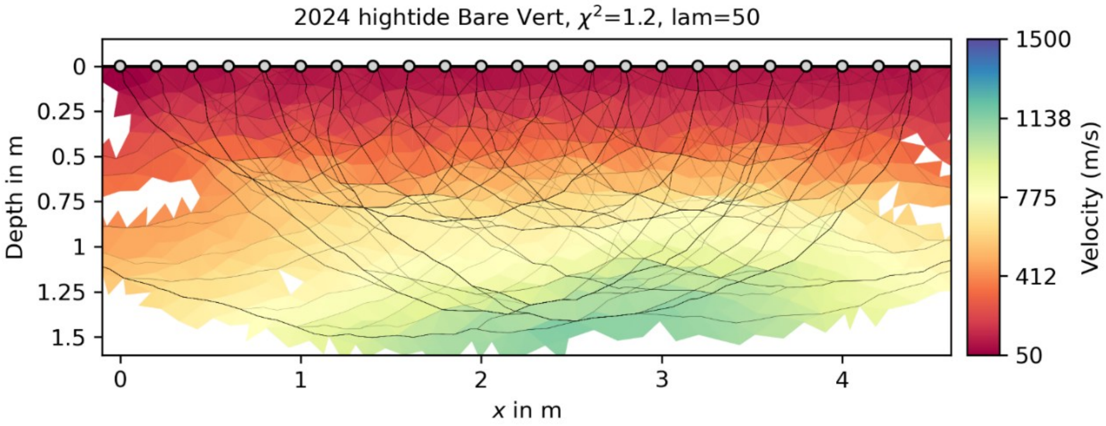

Figure 4.15: P-wave seismic velocity model of non-vegetated soil at high tide (2024). The model shows velocity variations with depth, with χ^2=1.0 and λ=50. Grey dots indicate geophone positions, and black solid lines represent the ray paths. On the right is the velocity scale in m/s.

Figures 4.13, 4.14, and 4.15 show the dromocrones and corresponding misfits for vegetated and non-vegetated soils at high tide in 2024 and the respective velocity models. The behaviour of the graphs and images mirrors what was described for the low tide case and vertical geophone setup.

Figure 4.14 shows a lower velocity than Figure 4.13 at lower depths. The same conduct can be observed comparing figures 4.15 and 4.12. This is probably due to the presence of water during high tide.

4.2 Remote Sensing

The geospatial analyses performed using Google Earth Pro and QGIS revealed areal and morphological changes in the San Felice salt marsh and its associated channels between 2004 and 2024. The results are presented in two main sections: variations in the salt marsh's surface area and bank migration dynamics of selected channels. All results are based on shapefiles derived from visual interpretation of satellite imagery, corrected for georeferencing uncertainty, and aggregated by year or time interval.

Between 2004 and 2024, the San Felice salt marsh experienced a progressive reduction in surface area. The total area decreased from approximately 726700 m^2 to about 711050 m^2 in 2024, indicating a net loss of nearly 15650 m^2 - or 1.56 hectares - over the 20 years.

This trend is illustrated in Figure 4.16, which shows a linear regression of annual area values. The regression line highlights a consistent and nearly linear decrease in surface extent, with a coefficient of determination (R^2) of 0.98, suggesting a strong temporal correlation (Table 4.1 reports the exact annual surface values used in the regression analysis).

Table 4.1: Annual surface values of the San Felice salt marsh.

Date	Area [m^2]
31/07/2004	726688.2
08/06/2005	727037.6
13/09/2006	725030.8
22/09/2007	723678.6
14/03/2014	717257.2
28/06/2016	715733.6
26/06/2017	715825.4
02/04/2018	714709.1
05/09/2019	713430.2
25/03/2021	712315.2
21/03/2023	712004.5
12/04/2024	711050.4

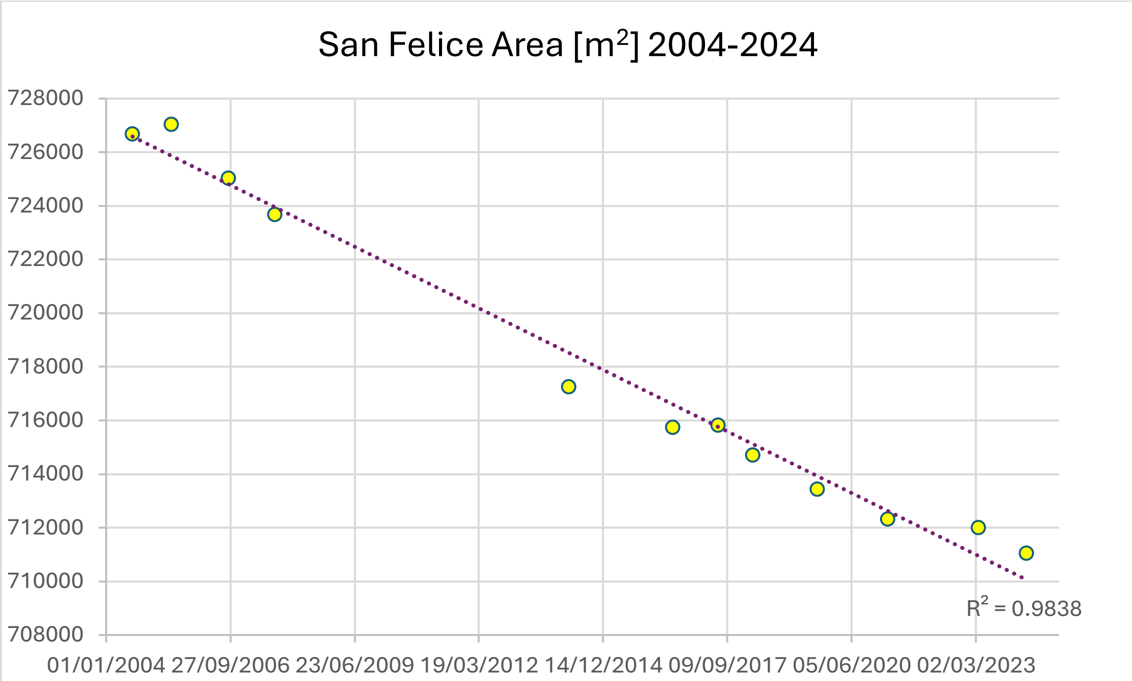

Figure 4.16: Linear regression of the San Felice salt marsh area between 2004 and 2024 (R^2=0.98).

The migration of channel banks between 2007 and 2024 was assessed for the Gaggian Channel, the San Felice Channel, an artificial channel, and the channel where seismic refraction surveys were performed. Each channel was analysed separately for both banks - left and right - and the results are shown as histograms illustrating the distribution of migration distances and migration rates, and a map showing where these retreats had been taking place. This was done for year pairs: 2007-2014 (Figures 4.17, 4.18), 2014-2017 (Figures 4.19, 4.20), 2017-2018 (Figures 4.21, 4.22), 2018-2019 (Figures 4.23, 4.24), 2019-2021 (4.25, 4.26), 2021-2024 (Figures 4.27, 4.28) and 2007-2024 (Figures 4.29, 4.30).

Across all channels, a general pattern of bank retreat is evident. The Gaggian and San Felice Channels exhibit the highest movement, with several displacements exceeding 10 m. Conversely, the artificial channel and the channel where seismic refraction surveys were performed show minimal migration, with most values remaining below 4 m.

Corresponding migration rates mirror these patterns and offer a standardised metric for comparing channel changes. Notably, higher migration values are associated with correspondingly higher rates, suggesting consistent displacement over time.

To ensure data reliability, each image's georeferencing error is reported and estimated based on the displacement of fixed reflectors highlighted in Table 3.4.

The same migration plots are presented in a larger format in Appendix B to enhance clarity.

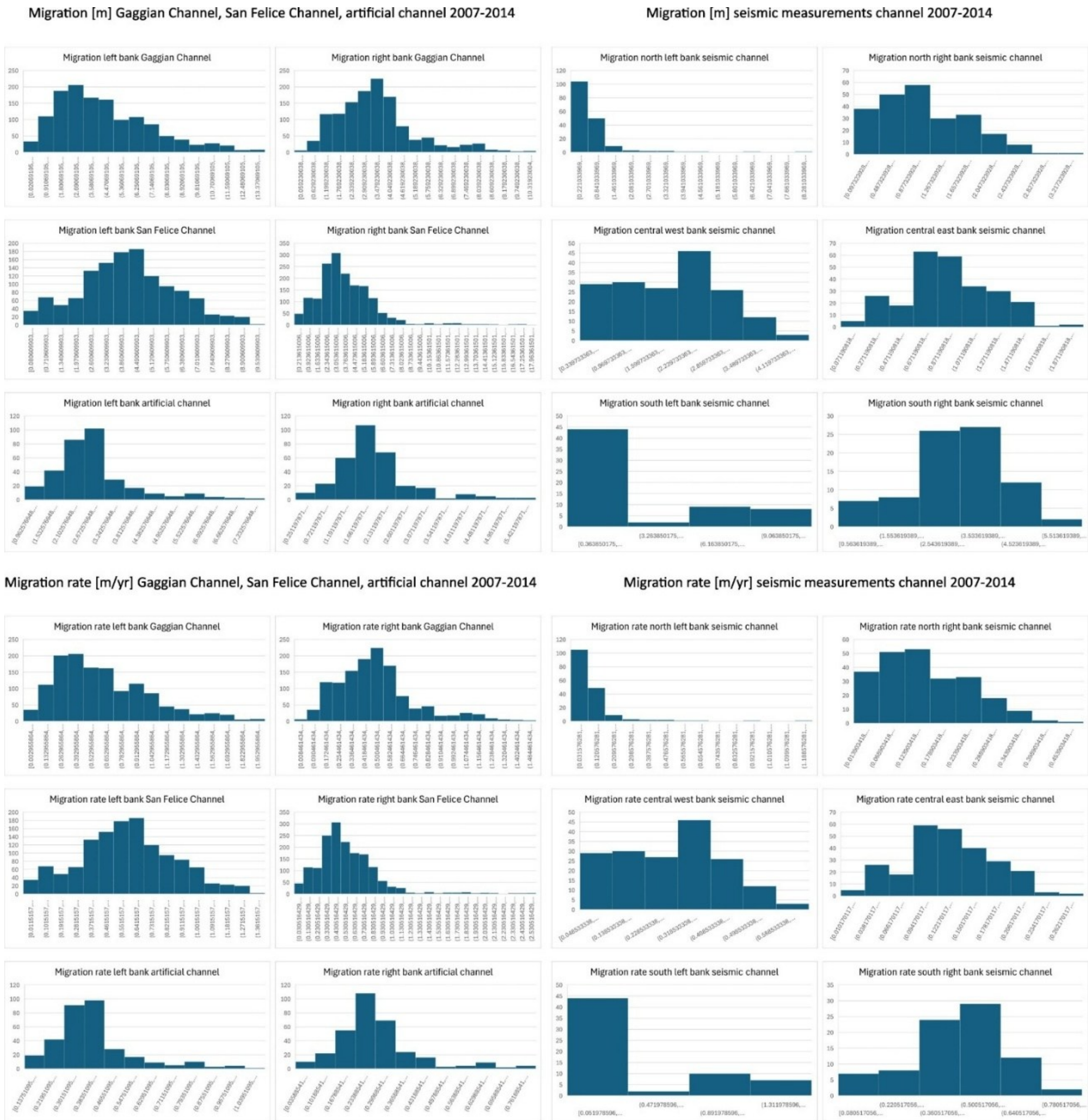

Figure 4.17: Distribution of channel migration distances (m) and rates (m/yr) for the left and right banks of the Gaggian Channel, San Felice Channel, the artificial channel, and for the seismic measurements channel banks subdivided into north, central, and south segments (2007–2014). Error: 1.87 m. For the enlarged version of this image, go to Appendix B, Figures B.1-B.4.

Figure 4.18: Spatial distribution of channel bank migration (in metres) in the San Felice salt marsh between 2007 and 2014. Colours represent the magnitude of lateral displacement along the banks. Data were derived from the Channel Migration plugin in QGIS and visualised on satellite imagery for contextual interpretation.

With a georeferencing error of 1.87 m, Figure 4.17 presents the distribution of channel migration distances (top panels) and migration rates (bottom panels) between 2007 and 2014 of the four channels investigated. For each one, both the left and right banks were analysed separately, and in the case of the seismic channel, further subdivisions were made into northern, central, and southern segments. This was done for each year pair for all the following images.

The histograms highlight the variability in migration intensity across different locations. In general, the Gaggian and San Felice channels exhibit higher migration values and broader distributions, especially on their right banks, with a mean distribution retreat between 2 and 4 m. Conversely, the artificial channel shows a more limited migration range: the left bank of the artificial channel has a mean retreat value between 2 and 2.7 m. In contrast, the right bank has 1.66 m. The seismic channel reveals spatial heterogeneity, with the central and southern segments showing a wider spread of migration distances and rates than the northern portion. The northern left bank has a migration distribution between 0.2 and 0.8 m, the northern right bank between 0.4 and 0.9 m. The central banks show the highest heterogeneity, with the western bank having a migration distribution reaching almost 3 m. Meanwhile, the east bank's values are between 0.6 and 1 m. The southern left bank shows less migration than the other banks, having a retreat of 0.4 m. The southern right bank has migration values between 2.5 and 4m.

Migration rates, expressed in metres per year, reflect the same patterns observed in the raw migration distances, adjusted for the time interval between observations. The left bank of the Gaggian Channel has a mean migration rate distribution between 0.25 and 0.40 m/yr, while the right bank is between 0.40 and 0.60 m/yr. The migration rate of the San Felice Channel is between 0.30 and 0.70 m/yr. The artificial channel has a mean migration rate distribution between 0.20 and 0.40 m/yr. The seismic measurements channel has a wide distribution of migration rates: the northern left bank is 0.03 m/yr, the northern right is between 0.06 and 0.17 m/yr. The central west bank has a wide migration rate distribution between 0.05 and 0.4 m/yr. The central east bank has a mean migration rate between 0.09 and 0.15 m/yr. The southern left bank has a migration rate of 0.05 m/yr, the right one between 0.36 and 0.64 m/yr.

Concerning the position of the retreat (Figure 4.18), the artificial and seismic measurements channel (with the exception of the left southern bank of the last one) show a homogeneous retreat in all the banks analysed. The left bank of the Gaggian Channel experiences a larger retreat in the southern part of the channel than its right counterpart. Vice versa, the northern part of the channel experiences a higher retreat on the right bank than on the left bank. Also, the San Felice Channel shows a similar pattern: the northern part of the channel has a higher retreat on the right bank, while the southern part has a higher retreat on the left bank.

Figure 4.19: Distribution of channel migration distances (m) and rates (m/yr) for the left and right banks of the Gaggian Channel, San Felice Channel, the artificial channel, and for the seismic measurements channel banks subdivided into north, central, and south segments (2014–2017). Error: 1.45 m. For the enlarged version of this image, go to Appendix B, Figures B.5-B.8.

Figure 4.20: Spatial distribution of channel bank migration (in metres) in the San Felice salt marsh between 2014 and 2017. Colours represent the magnitude of lateral displacement along the banks. Data were derived from the Channel Migration plugin in QGIS and visualised on satellite imagery for contextual interpretation.

With a georeferencing error of 1.45 m, Figure 4.19 presents the distribution of channel migration distances and rates between 2014 and 2017.

Like the previous case, the Gaggian and San Felice Channels have the highest migration values and rates. Observing the histogram and Figure 4.20, it is possible to affirm that the left bank of the Gaggian Channel has a higher retreat than the right bank, values between 0.7 and 1.5 m against 0.4 and 1 m for migration, between 0.25 and 0.5 m/yr and 0.11 and 0.33 m/yr for migration rate, respectively. A similar behaviour is observable in the San Felice Channel: the left bank has migration values between 1 and 2 m, the right one between 0.03 and 1 m. The migration rates are between 0.3 and 0.6 m/yr for the left bank and between 0.01 and 0.3 m/yr for the right bank.

The left bank of the artificial channel has a migration distribution between 0.6 and 1.3 m and a migration rate between 0.3 and 0.45 m/yr, the right one between 0.2 and 1.1 m and between 0.08 and 0.35 m/yr.

The seismic measurements channel's migration is as follows: the northern left bank has a migration distribution between 0.5 and 1.4 m, the northern right bank between 0.6 and 1 m, the central western bank between 0.05 and 1 m, and the eastern bank between 0.7 and 1.3 m. The southern left bank shows less migration than the other banks, retreating at 0.05 m. The southern right bank has migration values between 0.2 and 1m. The migration rates mirror this behaviour.

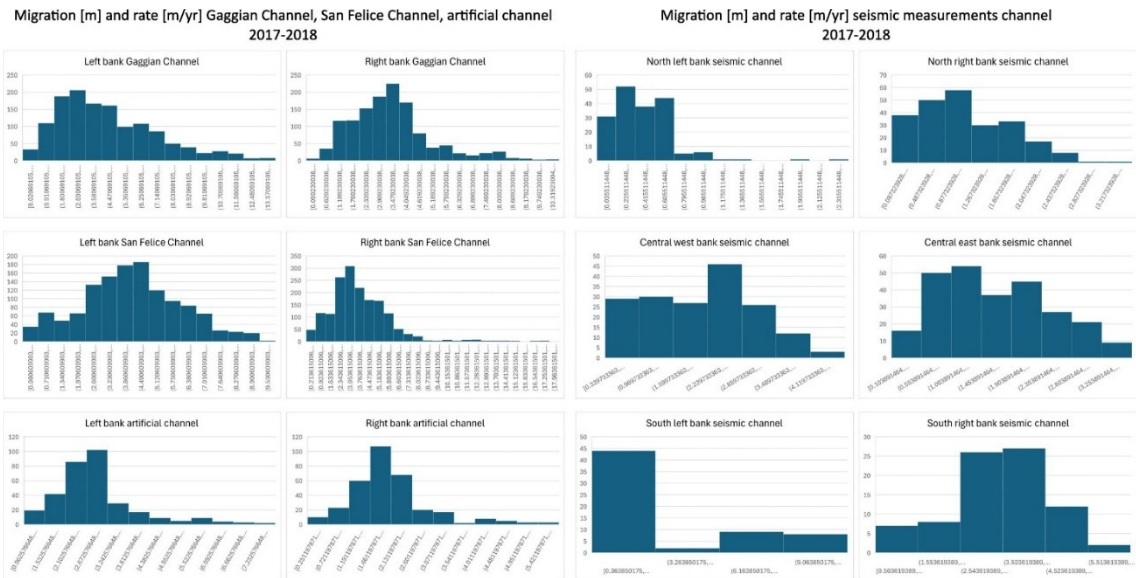

Figure 4.21: Distribution of channel migration distances (m) and rates (m/yr) for the left and right banks of the Gaggian Channel, San Felice Channel, the artificial channel, and for the seismic measurements channel banks subdivided into north, central, and south segments (2017–2018). Error: 0.92 m. For the enlarged version of this image, go to Appendix B, Figures B.9-B.10.

With a georeferencing error of 0.92 m, Figure 4.21 shows migration and migration rates of the channel banks studied between 2017 and 2018. The left bank of the Gaggian Channel has values between 1 and 5, and the right bank has values between 1 and 4. The San Felice Channel has migration and rate values between 2 and 4.5. The left bank of the artificial channel has values between 2 and 3, and the right bank has values between 1.6 and 2.

As in the previous cases, the seismic measurements channel shows significant heterogeneity. The northern left bank has migration and migration rate values between 0.05 and 0.7, the right bank between 0.1 and 1.2. The central banks have values between 0.3 and 2.5. The southern left bank has a mean value of 0.36, and the right bank has a mean value between 2.5 and 4.5.

Figure 4.22: Spatial distribution of channel bank migration (in metres) in the San Felice salt marsh between 2017 and 2018. Colours represent the magnitude of lateral displacement along the banks. Data were derived from the Channel Migration plugin in QGIS and visualised on satellite imagery for contextual interpretation.

Figure 4.22 shows where the migration happened between 2017 and 2018. As in the previous cases, the southern part of the left bank of the Gaggian Channel shows higher migration values than its right counterpart; vice versa, the right bank has higher migration values than the left bank in the northern part of the channel. A similar pattern can be observed in the San Felice Channel. The artificial and seismic measurements channels show more homogeneous behaviour than the Gaggian and San Felice channels.

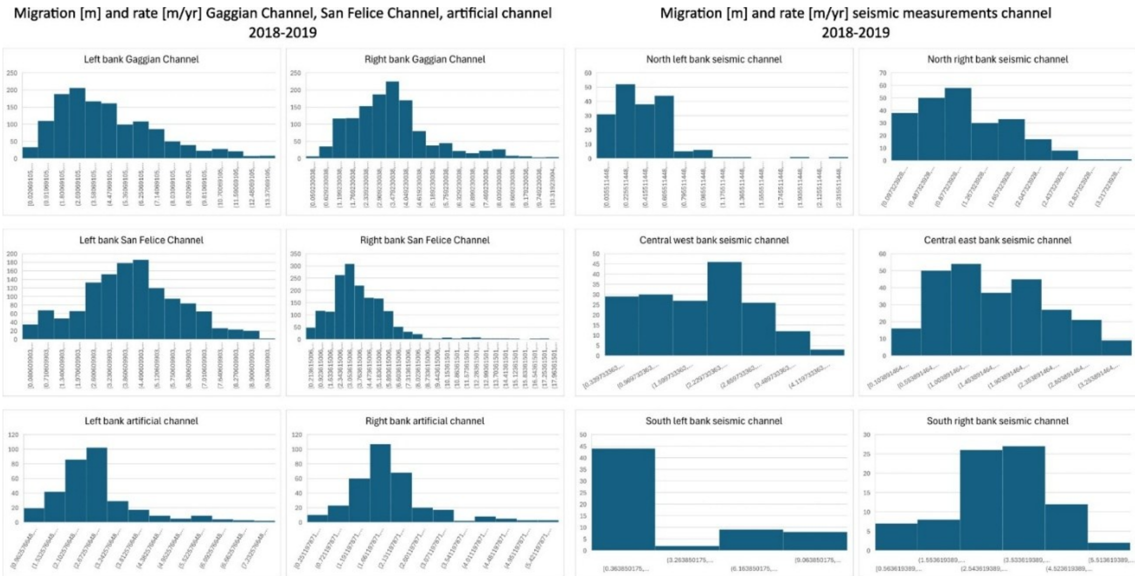

Figure 4.23: Distribution of channel migration distances (m) and rates (m/yr) for the left and right banks of the Gaggian Channel, San Felice Channel, the artificial channel, and for the seismic measurements channel banks subdivided into north, central, and south segments (2018–2019). Error: 1.22 m. For the enlarged version of this image, go to Appendix B, Figures B.11-B.12.

With a georeferencing error of 1.22 m, Figure 4.23 shows the migration distances and rates of the channel between 2018 and 2019. Gaggian's left bank has values between 1 and 5, and the right one has values between 1.8 and 4.5. San Felice Channel has values approximately between 2 and 4.5. The left bank of the artificial channel has values between 2 and 3, and the right bank between 1.2 and 2.

The seismic measurements channel shows heterogeneous retreat among its banks. The northern left bank has values between 0.2 and 0.7, and the northern right bank has values between 0.4 and 0.9. The central west bank has values between 0.4 and 2.8, and the east one between 0.5 and 2.3. The southern left bank has a mean value of 0.36, and the right bank has values between 2.5 and 4.5.

Figure 4.24: Spatial distribution of channel bank migration (in metres) in the San Felice salt marsh between 2018 and 2019. Colours represent the magnitude of lateral displacement along the banks. Data were derived from the Channel Migration plugin in QGIS and visualised on satellite imagery for contextual interpretation.

Similarly to the previous cases, Figure 4.24 shows that the southern part of the left bank of the Gaggian Channel has higher migration values than the right bank, and the opposite can be observed in the northern part of the channel. The San Felice Channel mirrors this pattern. The artificial and seismic measurements channels exhibit homogeneous behaviour in all their banks.

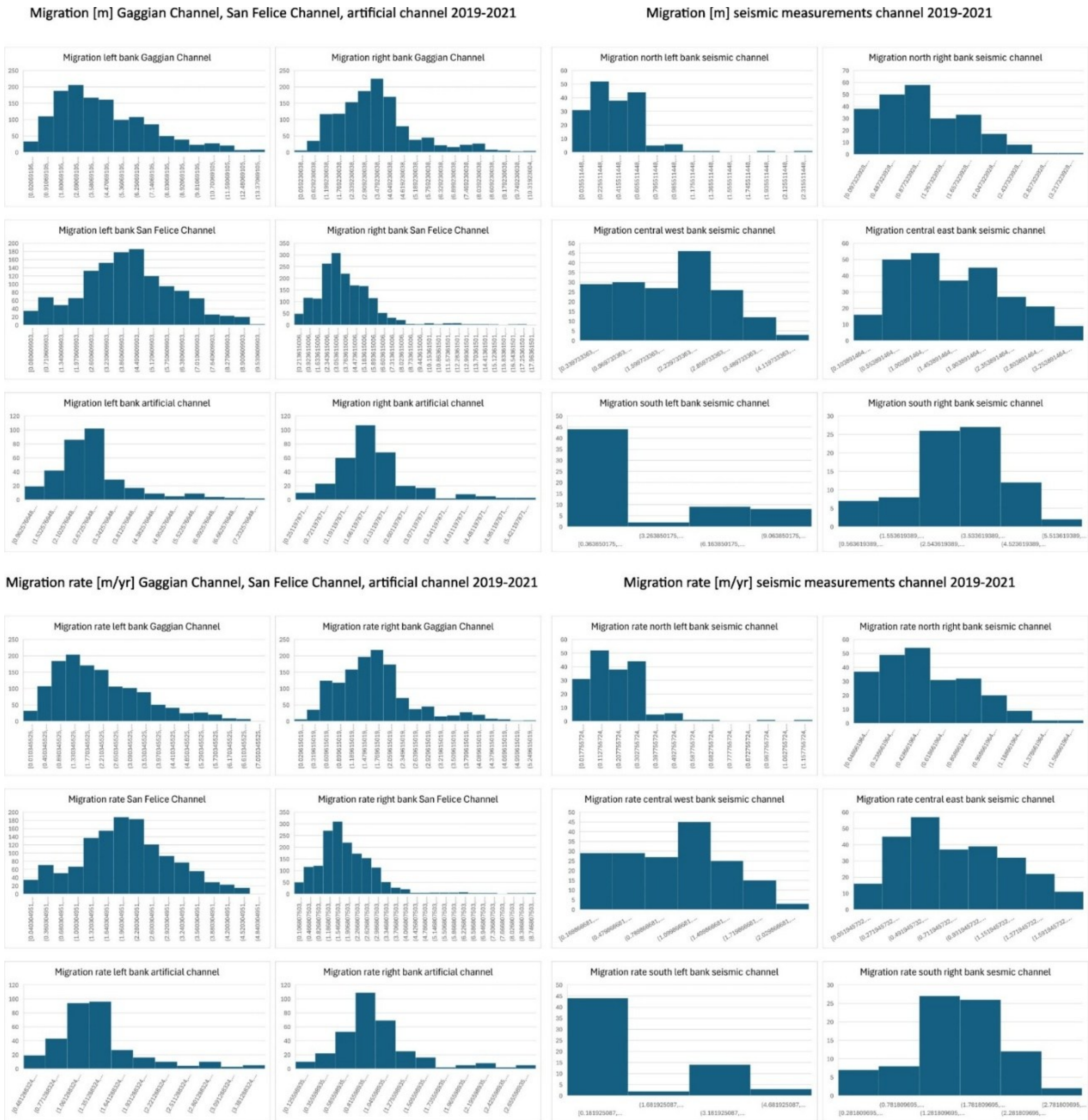

Figure 4.25: Distribution of channel migration distances (m) and rates (m/yr) for the left and right banks of the Gaggian Channel, San Felice Channel, the artificial channel, and for the seismic measurements channel banks subdivided into north, central, and south segments (2019–2021). Error: 1.13 m. For the enlarged version of this image, go to Appendix B, Figures B.13-B.16.

Figure 4.25 shows migration and migration rate distributions between 2019 and 2021, with a georeferencing error of 1.13 m. The left bank of the Gaggian Channel has a migration distribution between 1 and 4.4 m and a migration rate distribution between 0.5 and 2.2 m/yr. The right bank has a migration distribution between 1.8 and 4.5 m and a migration rate between 0.9 and 2.2 m/yr. The San Felice Channel has a mean migration distribution between 2 and 4.5 m and a mean migration rate between 1.2 and 2.2 m/yr.

The artificial channel shows a migration between 2 and 3 m on the left bank and between 1.5 and 2 m on the right bank. The migration rates are between 1 and 1.6 m/yr for the left bank and between 0.8 and 1 m/yr for the right bank.

The migration of the northern left bank of the seismic measurements channel is between 0.2 and 0.7 m, and the migration rate is between 0.1 and 0.3 m/yr; for the right bank, it is between 0.4 and 1.2 m, and 0.2 and 0.6 m/yr. The migration for the central west bank is between 1 and 3 m, while for the central east, it is between 0.5 and 2.3 m. The migration rates are between 0.5 and 1.5 m/yr and between 0.2 and 1.1 m/yr respectively. The southern banks show the most significant difference, with the left bank migrating approximately 0.4 m (migration rate 0.2 m/yr) and the right bank between 2.5 and 4 m (migration rate between 1.2 and 2 m/yr).

Figure 4.26: Spatial distribution of channel bank migration (in metres) in the San Felice salt marsh between 2019 and 2021. Colours represent the magnitude of lateral displacement along the banks. Data were derived from the Channel Migration plugin in QGIS and visualised on satellite imagery for contextual interpretation.

Figure 4.26 shows again the aforementioned pattern, with the left banks of Gaggian and San Felice Channel retreating more than their right counterparts in the southern parts of the channels and vice versa in the northern parts. The other two channels show a heterogeneous behaviour along their banks.

Figure 4.27: Distribution of channel migration distances (m) and rates (m/yr) for the left and right banks of the Gaggian Channel, San Felice Channel, the artificial channel, and for the seismic measurements channel banks subdivided into north, central, and south segments (2021–2024). Error: 1.73 m. For the enlarged version of this image, go to Appendix B, Figures B.17-B.20.

Figure 4.28: Spatial distribution of channel bank migration (in metres) in the San Felice salt marsh between 2021 and 2024. Colours represent the magnitude of lateral displacement along the banks. Data were derived from the Channel Migration plugin in QGIS and visualised on satellite imagery for contextual interpretation.

Figure 4.27 shows the migration and migration rates of the four studied channels between 2021 and 2024, with a georeferencing error of 1.73 m. The left bank of the Gaggian Channel has a migration distribution between 0.5 and 1.5 m, resulting in a migration rate between 0.2 and 0.7 m/yr. The right bank of the Gaggian Channel has a migration distribution between 0.3 and 1 m (migration rate between 0.1 and 0.3 m/yr). Looking at Figure 4.28, it is possible to observe the described behaviour, with Gaggian's left bank retreating more than the right bank. The same can be said for the San Felice Channel, where the left bank has a migration between 1 and 2 m (migration rate between 0.3 and 0.6 m/yr), and the right bank between 0.02 and 1 m (migration rate reaching 0.4 m/yr). The migration for the artificial channel is between 0.6 and 1.2 m (0.2-0.4 m/yr) for the left bank and between 0.2 and 1 m (0.08-0.4 m/yr) for the right bank.

The seismic measurements channel shows retreat heterogeneity among the different banks: the northern left bank has a migration between 0.5 and 0.9 m (0.2-0.3 m/yr), the right bank between 0.6 and 1 m (0.2-0.3 m/yr). The central banks' migrations for the east and west are between 0.05 and 1 m (0.02-0.3 m/yr) and between 0.8 and 1.3 m (0.2-0.5 m/yr). The southern left bank has a migration between 0.05 and 3 m (0.02-1 m/yr), the right bank between 0.25 and 1.2 m (0.08-0.4 m/yr).

Figure 4.29: Distribution of channel migration distances (m) and rates (m/yr) for the left and right banks of the Gaggian Channel, San Felice Channel, the artificial channel, and for the seismic measurements channel banks subdivided into north, central, and south segments (2007–2024). Error: 1.67 m. For the enlarged version of this image, go to Appendix B, Figures B.21-B.24.

Figure 4.30: Spatial distribution of channel bank migration (in metres) in the San Felice salt marsh between 2007 and 2024. Colours represent the magnitude of lateral displacement along the banks. Data were derived from the Channel Migration plugin in QGIS and visualised on satellite imagery for contextual interpretation.

The migration and migration rates between 2007 and 2024 are shown as a final and complete representation. Figure 4.29 shows the histograms, and Figure 4.30 shows the migration map with a georeferencing error of 1.67 m.

The left bank of the Gaggian Channel has a migration distribution between 1 and 5 m and a migration rate between 0.1 and 0.3 m/yr. The migration for the right bank is between 2 and 4 m (0.1-0.25 m/yr). The southern portion of the left bank of this channel shows higher migration values than the right one, while the opposite is true in the northern part.

The San Felice Channel has migration values between 2 and 5 m, hence migration rates between 0.1 and 0.3 m/yr. Also, in this case, the southern part of the channel has higher migration values on the left than on the right; it is the opposite in the northern portion.

The migration for the left bank of the artificial channel is between 2 and 3 m (0.1-0.2 m/yr), and for the right bank, it is between 1.2 and 2 m (0.06-0.1 m/yr). The map also shows that the left bank has a higher retreat than the right one.

The channel where seismic measurements were conducted shows prominent differences between the left and right banks of the northern and southern portions. The northern left bank has migration values between 0.2 and 0.7 m (0.01-0.04 m/yr), the northern right bank between 0.4 and 1 m (0.02-0.07 m/yr). The central banks show similar distances, with migration values between 0.5 and 2.8 m (0.03 and 0.2 m/yr). The migration for the southern left bank is between 0.3 and 3 m (0.02-0.2 m/yr), while it is between 2.5 and 4.5 m (0.14-0.15 m/yr) for the southern right bank.

4.3 Wind Wave-Tidal Model

This section presents the visualised outputs of the combined wind wave-tidal model for 2020 (Figure 4.31), 2021 (Figure 4.32), 2022 (Figure 4.33), 2023 (Figure 4.34), and May 2024 (Figure 4.35). The corresponding figures illustrate the temporal evolution of three key parameters: the water level, the wave height, and the total bottom shear stress at two different positions. The water level data exhibit the oscillatory behaviour characteristic of the tidal cycle. At the same time, the wave height and shear stress profiles reflect the influence of both hydrodynamic conditions and meteorological forcing. The blue line is the measured data, and the red dotted line is the relative linear trend, considering each measure (every half hour for every day of each year).

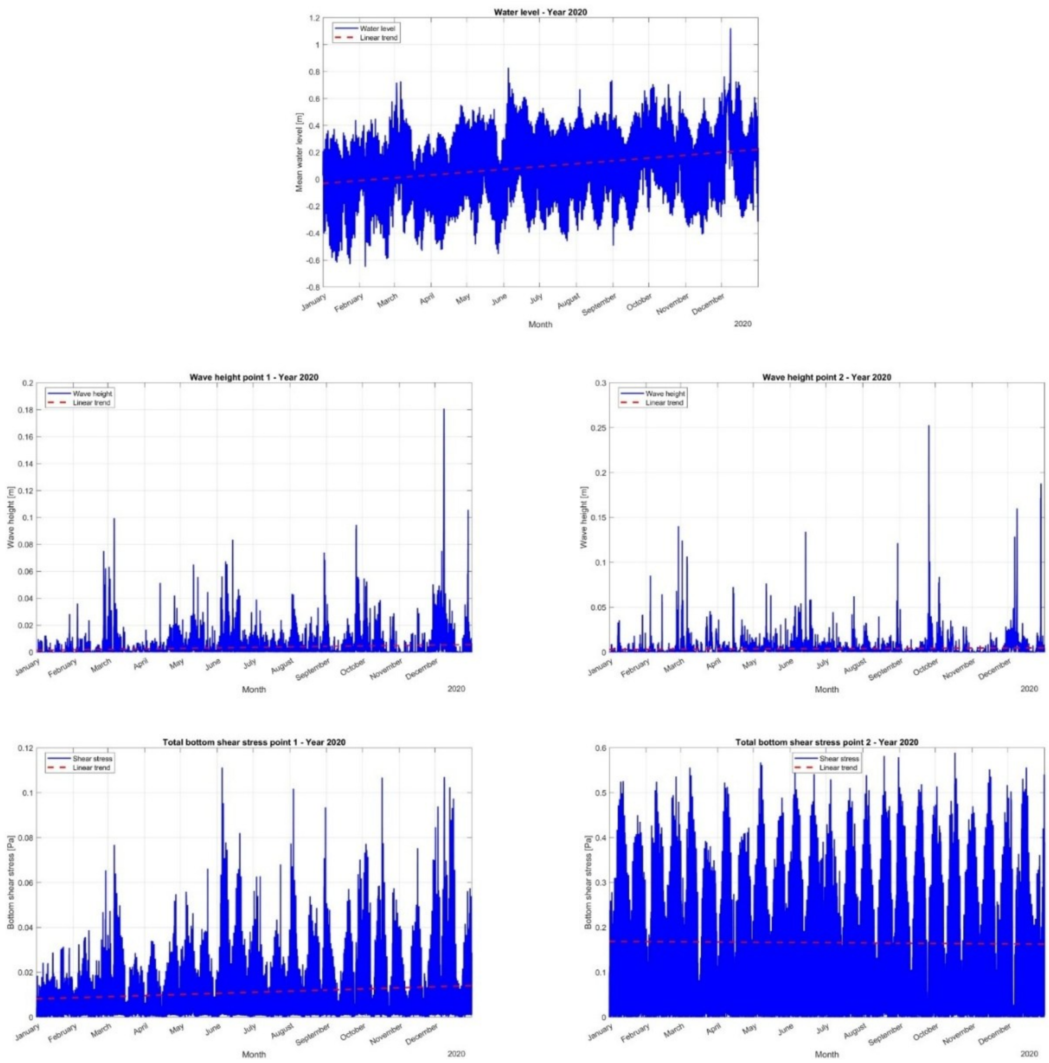

Figure 4.31: Modelled water level (top section), wave height (central section) and total bottom shear stress (bottom section) for both investigated points in 2020. In the abscissa, the months between January and December, in the ordinate, the analysed parameter. The red dotted line represents the relative linear trend.

The top panel of Figure 4.31 shows the water level, expressed in metres, for 2020. This parameter varies between -0.4 and 0.6 m, with peaks reaching -0.6, 0.8, and 1 m. The relative linear trend shows an increment of the water level between 0 and 0.1 m between January and December.

The central panels show the wave height for points 1 (in the seismic measurements channel) and 2 (in the San Felice Channel). The general behaviour is similar: the wave height is concentrated below 0.05 m, the main difference is that the majority of the peaks for point 1 are concentrated below 0.08 m, with a few cases exceeding this threshold; in point 2, they reach peaks higher than 0.1 m, with the highest peak arriving at 0.25 m.

The bottom shear stress, pictured in the bottom panels, shows a difference of one order of magnitude between the two points: only four peaks exceed the threshold of 0.1 Pa in point one, while in point two, many reach and exceed 0.5 Pa. The linear trend is congruent with the water level in all four cases.

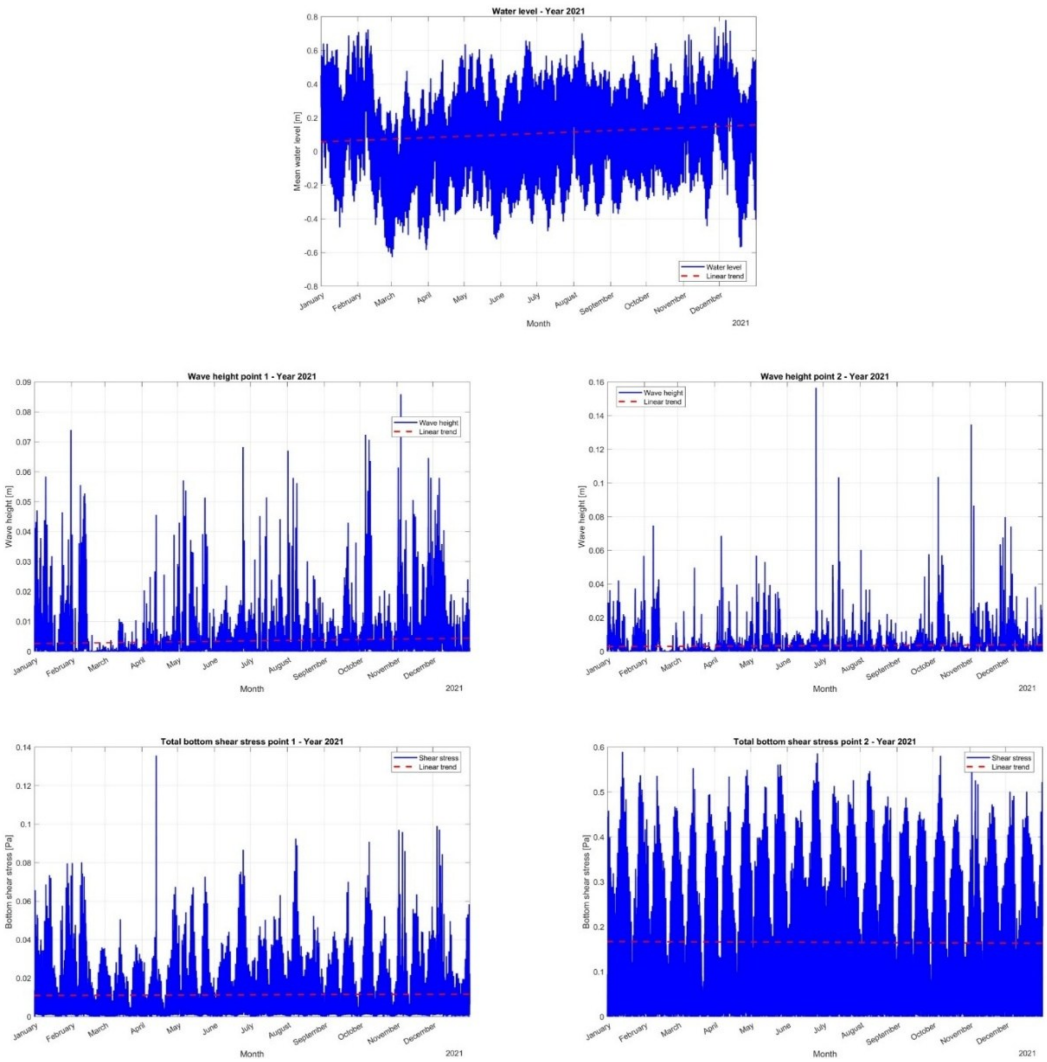

Figure 4.32: Modelled water level (top section), wave height (central section) and total bottom shear stress (bottom section) for both investigated points in 2021. In the abscissa, the months between January and December, in the ordinate, the analysed parameter. The red dotted line represents the relative linear trend.

The top panel of Figure 4.32 shows the water level, expressed in metres, for 2021. In this case, the variation is generally between -0.4 and 0.5 m, with peaks reaching -0.6 and 0.7 m. The relative linear trend shows an increment of the water level between 0.05 and 0.1 m between January and December.

The wave height for point one generally has a behaviour that exceeds 0.01 m, except in March and April, where the wave height is usually below. Only four peaks exceed the height of 0.07 m, never reaching 0.09 m. Point two’s wave height varies between 0.02 and 0.04 m, with peaks reaching values between 0.06 and 0.15 m.

The bottom shear stress, pictured in the bottom panels, shows a difference of one order of magnitude between the two points: only one peak exceeds the threshold of 0.1 Pa in point one, while the values vary between 0.1 and 0.5 Pa in point two. The linear trend is almost flat in all four cases.

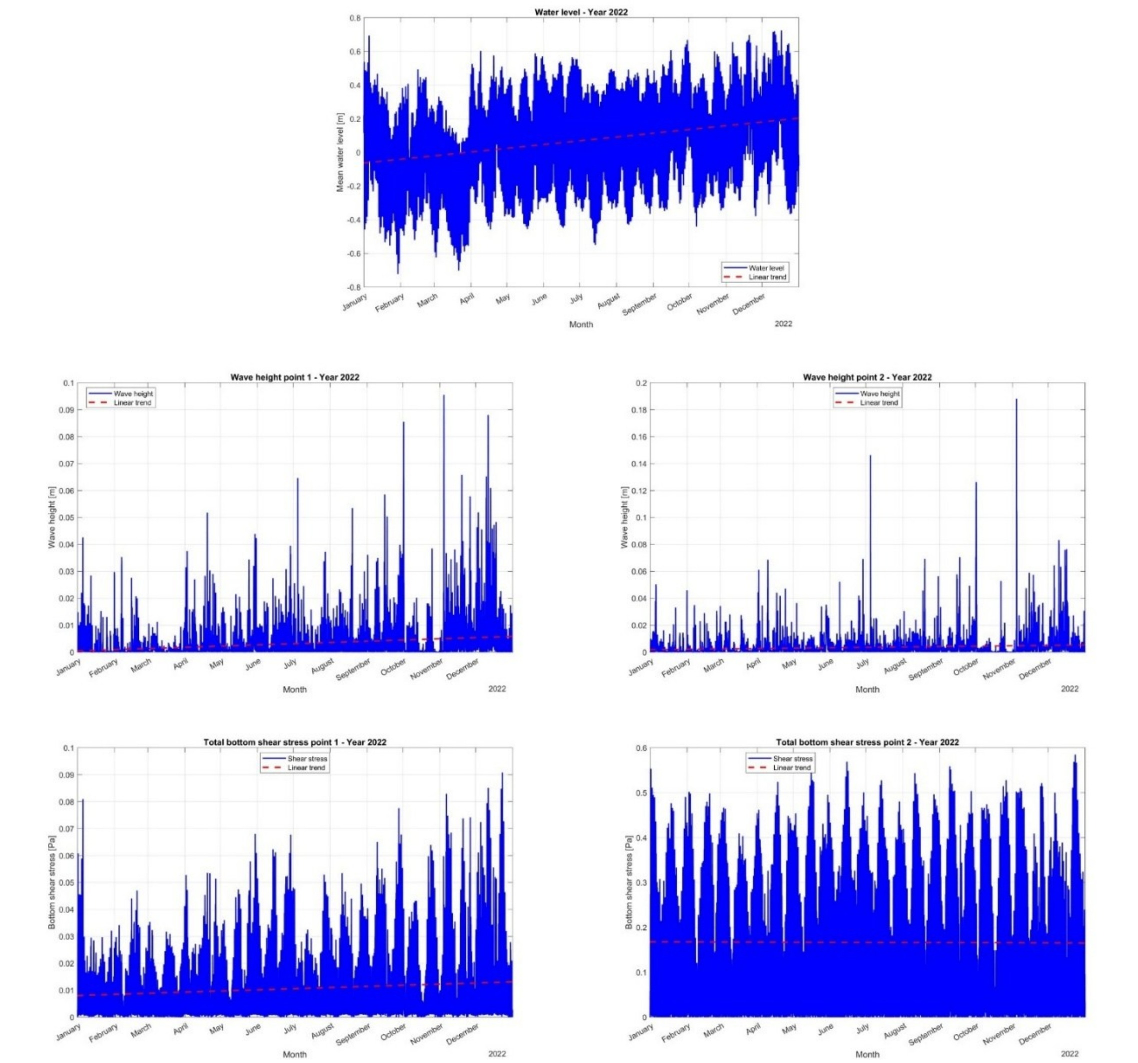

Figure 4.33: Modelled water level (top section), wave height (central section) and total bottom shear stress (bottom section) for both investigated points in 2022. In the abscissa, the months between January and December, in the ordinate, the analysed parameter. The red dotted line represents the relative linear trend.

The top panel of Figure 4.33 shows the water level, expressed in metres, for 2022. The variation is generally between -0.4 and 0.4 m, with peaks exceeding -0.6 and 0.6 m. The relative linear trend shows an increment of the water level between -0.05 and 0.2 m between January and December.

The wave height for point one generally has a behaviour that varies between 0.01 m and 0.04 m, except in March and April, where the wave height is usually below 0.01 m. Three peaks exceed the height of 0.08 m, almost reaching 0.1 m. Point two's wave height varies between 0.01 and 0.04 m, with peaks reaching values between 0.06 and 0.18 m.

The bottom shear stress, pictured in the bottom panels, shows a difference of one order of magnitude between the two points: in point one, the variation is between 0.01 and 0.08 Pa, while the values vary between 0.1 and 0.55 Pa in point two. The relative linear trend increases in all four cases.

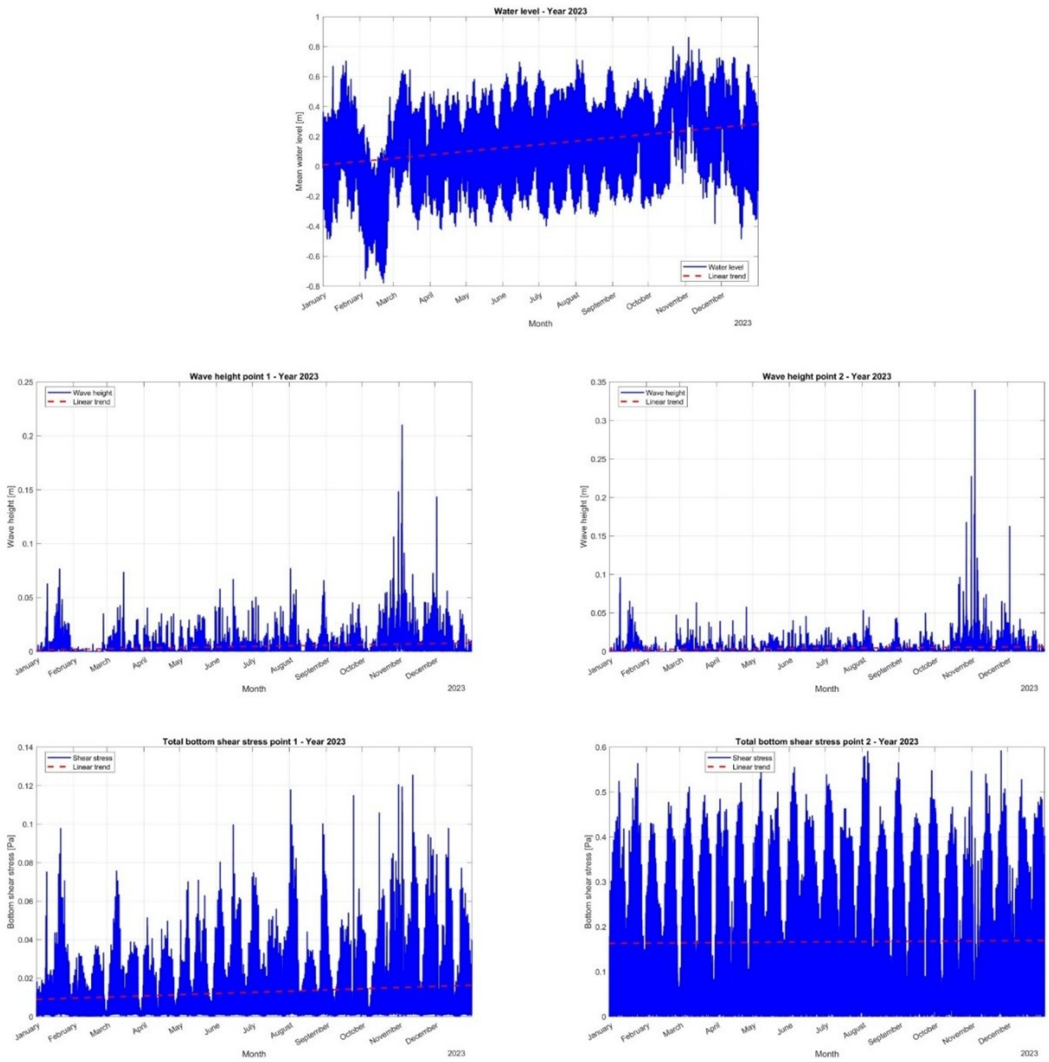

Figure 4.34: Modelled water level (top section), wave height (central section) and total bottom shear stress (bottom section) for both investigated points in 2023. In the abscissa, the months between January and December, in the ordinate, the analysed parameter. The red dotted line represents the relative linear trend.

The top panel of Figure 4.34 shows the water level, expressed in metres, for 2023. The variation is generally between -0.4 and 0.6 m, except between February and March, when the water level is below 0 m and reaches -0.8 m. The relative linear trend shows an increment of the water level between 0 and 0.2 m between January and December.

The wave height behaves similarly for both points, usually below 0.05 m. Between October and December, an increment can be observed for point one, with values between 0.05 and 0.2 m. The same can be observed for point two, with peaks exceeding 0.2 m.

The bottom shear stress, pictured in the bottom panels, shows that in point one, the variation is between 0.02 and 0.06 Pa, with a few peaks exceeding 0.1 Pa, while the values vary between 0.1 and 0.5 Pa in point two. An increasing relative linear trend can be observed in all four cases.

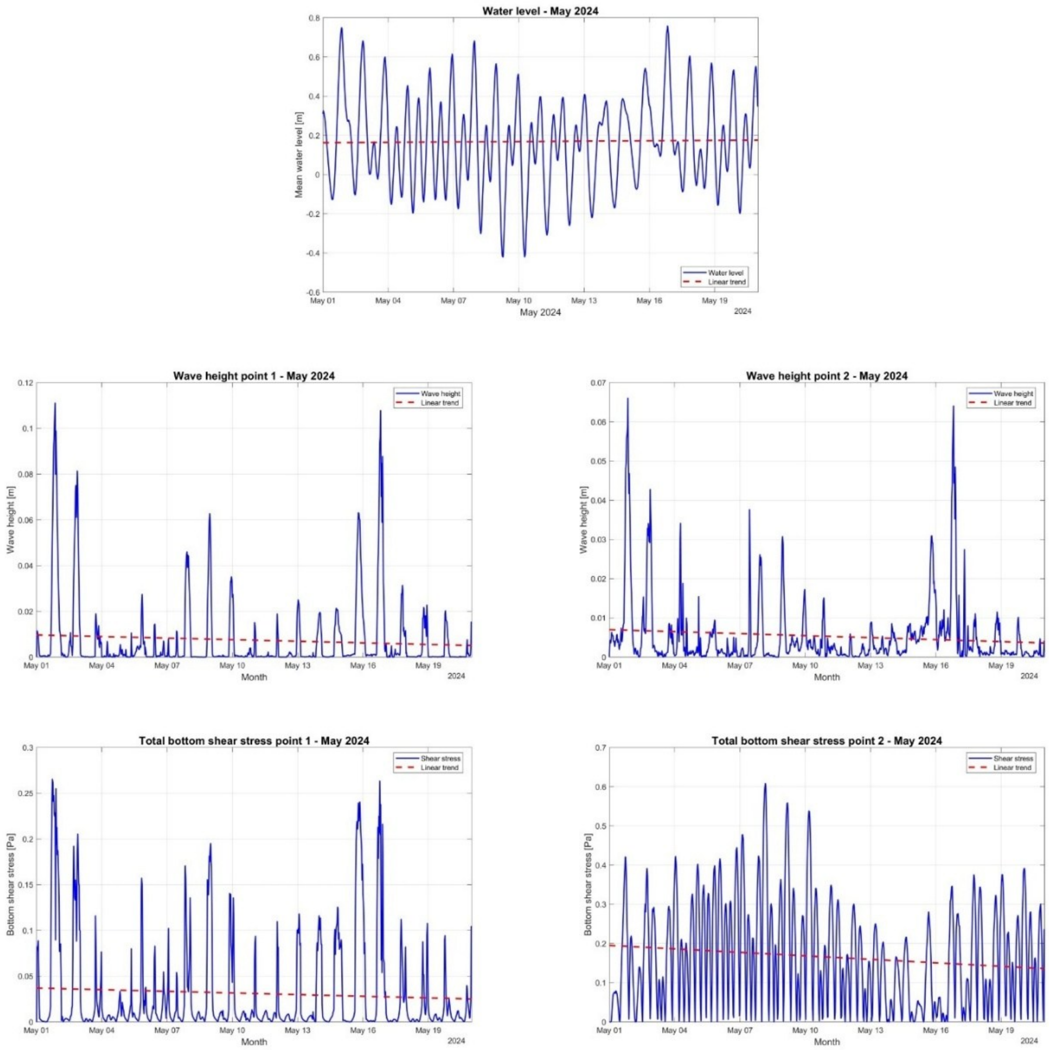

Figure 4.35: Modelled water level (top section), wave height (central section) and total bottom shear stress (bottom section) for both investigated points in May 2024. In the abscissa, the month of May, in the ordinate, the analysed parameter. The red dotted line represents the relative linear trend.

The top panel of Figure 4.35 shows the water level, expressed in metres, for May 2024. The variation is generally between -0.2 and 0.4 m, with peaks exceeding -0.4 and 0.6 m. The relative linear trend is flat for the whole duration of the month.

In contrast with the other graphs, the wave height for point one reaches higher peak values than for point two, with the threshold being 0.06 m, where point one has higher values and point two has lower values. Generally, point two has higher wave heights than point one: point one's values vary between 0 and 0.02 m, point two between 0.01 and 0.02 m.

The bottom shear stress, pictured in the bottom panels, varies between 0 and 0.1 Pa in point one, and the variation is between 0.1 and 0.4 Pa in point two. A decreasing relative linear trend can be observed in all four cases.

4.4 Soil Core Analysis

The following pages report the visual representations and tables of the results obtained from core sampling processing (Tables 4.2-4.6, Figures 4.36-4.39).

Each graph shows the water content (on the left) and LOI (on the right), both plotted against depth (in cm). The data points follow a decreasing trend with depth, indicating that the water and organic content are highest near the surface and diminish as depth increases. Water content and LOI seem to follow approximately the same trend.

It is important to note that the organic matter content of the vegetated samples is almost twice that of the non-vegetated samples within the first 30 cm; beyond this depth, they are all quite similar. The water content increases or decreases alongside the organic matter content. Hence, there is more water in the vegetated samples in the first 30 cm compared to the non-vegetated ones.

Table 4.2: Values of water content and LOI for core sample 1 (non-vegetated), both in g/g and %.

DEPTH [cm]	Non-vegetated (1)			
	Water content [g/g]	Water content [%]	LOI [g/g]	LOI [%]
0	0.367929511	36.79295115	0.042027463	4.202746342
5	0.330520282	33.05202815	0.040965653	4.096565279
10	0.338312053	33.83120526	0.036780994	3.67809936
15	0.287892702	28.7892702	0.023213722	2.321372178
20	0.255693146	25.56931465	0.019105439	1.910543906
25	0.243895561	24.38955606	0.017066583	1.706658343
30	0.23937363	23.93736304	0.015952266	1.595226584
35	0.234075295	23.40752954	0.01190782	1.190781973
40	0.230602954	23.06029538	0.012156381	1.215638096
45	0.234528346	23.45283461	0.011221976	1.122197648
50	0.223972099	22.39720986	0.012498069	1.249806945
70	0.226425131	22.64251307	0.011251023	1.125102282
90	0.211175763	21.11757634	0.009434123	0.943412311

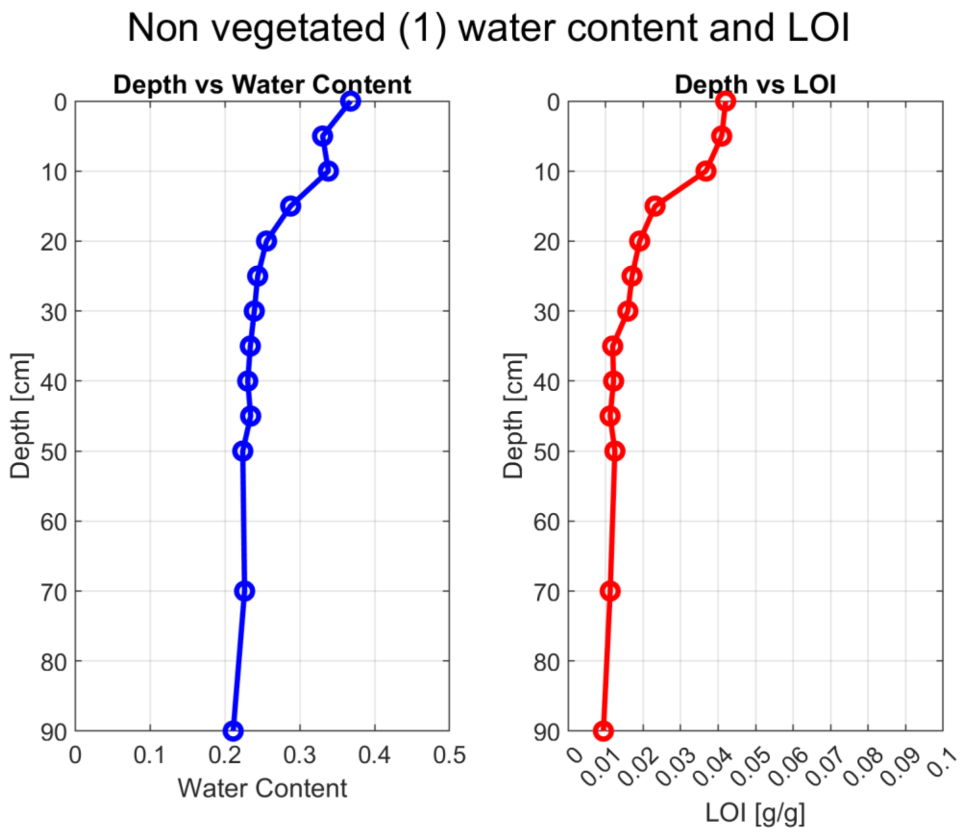

Figure 4.36: Visual representation of water content and LOI (g/g) of core sample 1 (non-vegetated).

Table 4.3: Values of water content and LOI for core sample 2 (vegetated), both in g/g and %.

DEPTH [cm]	Vegetated (2)			
	Water content [g/g]	Water content [%]	LOI [g/g]	LOI [%]
0	0.40154845	40.15484495	0.080153226	8.015322645
5	0.416827986	41.68279862	0.073007394	7.30073942
10	0.472875049	47.28750485	0.086276014	8.627601419
15	0.351094754	35.10947541	0.038956147	3.895614708
20	0.343901895	34.39018954	0.039193713	3.919371312
25	0.296307204	29.63072043	0.032447729	3.244772855
30	0.266545561	26.65455609	0.025817658	2.581765824
35	0.255358318	25.53583183	0.022317324	2.231732414
40	0.245475784	24.5475784	0.018540555	1.854055537
45	0.235310758	23.5310758	0.019012583	1.901258299
50	0.233726837	23.37268375	0.018486888	1.848688817
70	0.218450156	21.84501558	0.012493685	1.249368503
90	0.217203553	21.72035529	0.01361002	1.361002037

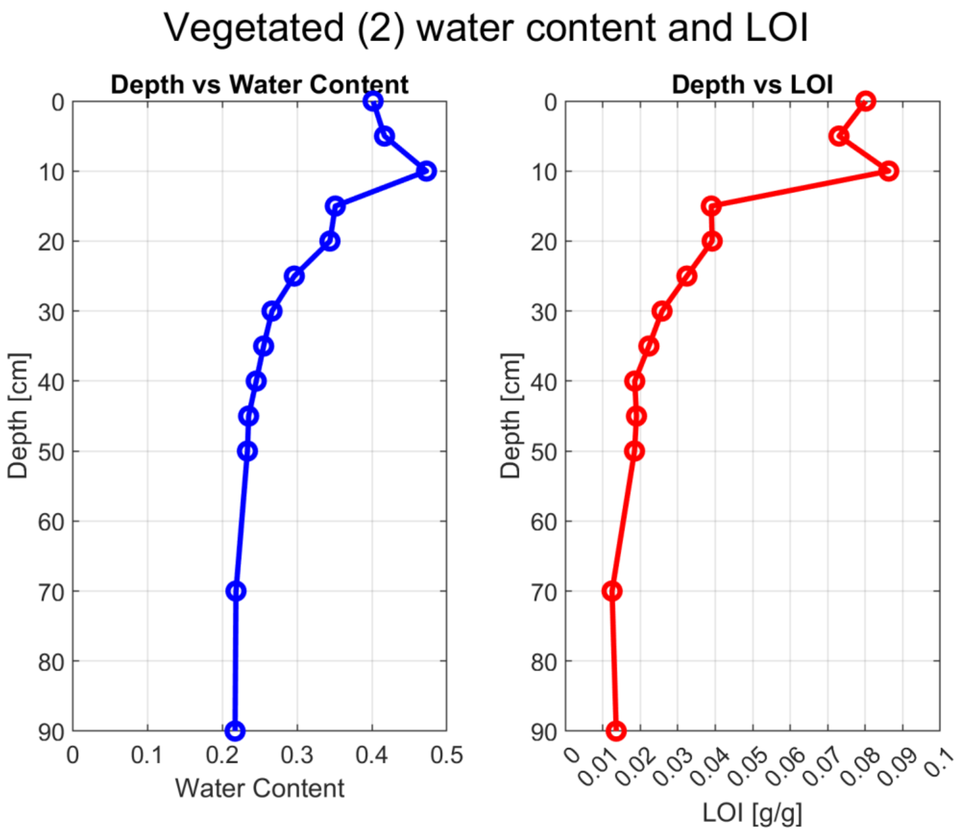

Figure 4.37: Visual representation of water content and LOI (g/g) of core sample 2 (vegetated).

Table 4.4: Values of water content and LOI for core sample 3 (non-vegetated), both in g/g and %.

DEPTH [cm]	Non-vegetated (3)			
	Water content [g/g]	Water content [%]	LOI [g/g]	LOI [%]
0	0.244409567	24.44095673	0.030114657	3.011465672
5	0.265770362	26.57703622	0.031211445	3.121144462
10	0.222808866	22.28088659	0.022206873	2.220687287
15	0.243071676	24.3071676	0.023421334	2.342133398
20	0.251591408	25.15914076	0.021779554	2.177955428
25	0.235366971	23.53669706	0.018304689	1.830468921
30	0.245507024	24.5507024	0.020755698	2.075569769
35	0.242806406	24.28064064	0.019496207	1.949620679
40	0.243507559	24.35075587	0.019755947	1.975594674
45	0.22972941	22.97294095	0.019341775	1.934177494
50	0.228911938	22.89119385	0.019468092	1.946809197
70	0.233600948	23.36009482	0.01947552	1.947552001
90	0.232724553	23.27245531	0.016623228	1.662322814

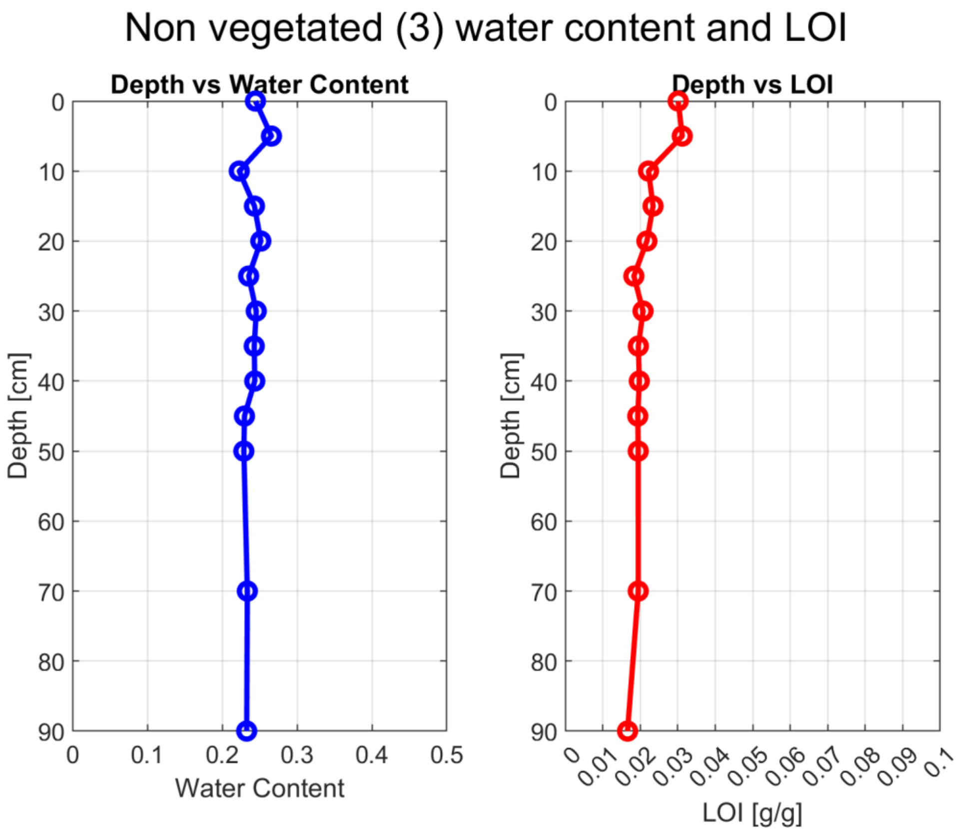

Figure 4.38: Water content and LOI (g/g) of core sample 3 (non-vegetated).

Table 4.5: Values of water content and LOI for core sample 4 (vegetated), both in g/g and %.

DEPTH [cm]	Vegetated (4)			
	Water content [g/g]	Water content [%]	LOI [g/g]	LOI [%]
0	0.403581715	40.35817146	0.05736316	5.736315982
5	0.354240273	35.42402725	0.043148506	4.314850573
10	0.284079695	28.40796952	0.02851769	2.851769012
15	0.313546618	31.35466182	0.035895128	3.589512849
20	0.300697084	30.06970838	0.028871602	2.887160157
25	0.257944519	25.79445189	0.017906202	1.790620177
30	0.259526485	25.95264853	0.019621363	1.962136305
35	0.257202657	25.72026573	0.020948736	2.094873634
40	0.248367944	24.83679444	0.01425034	1.425034017
45	0.278023715	27.80237149	0.02080521	2.080521026
50	0.267218869	26.72188686	0.020816595	2.081659484
70	0.226737347	22.67373473	0.014521839	1.45218385
90	0.240572867	24.05728666	0.015199264	1.519926402

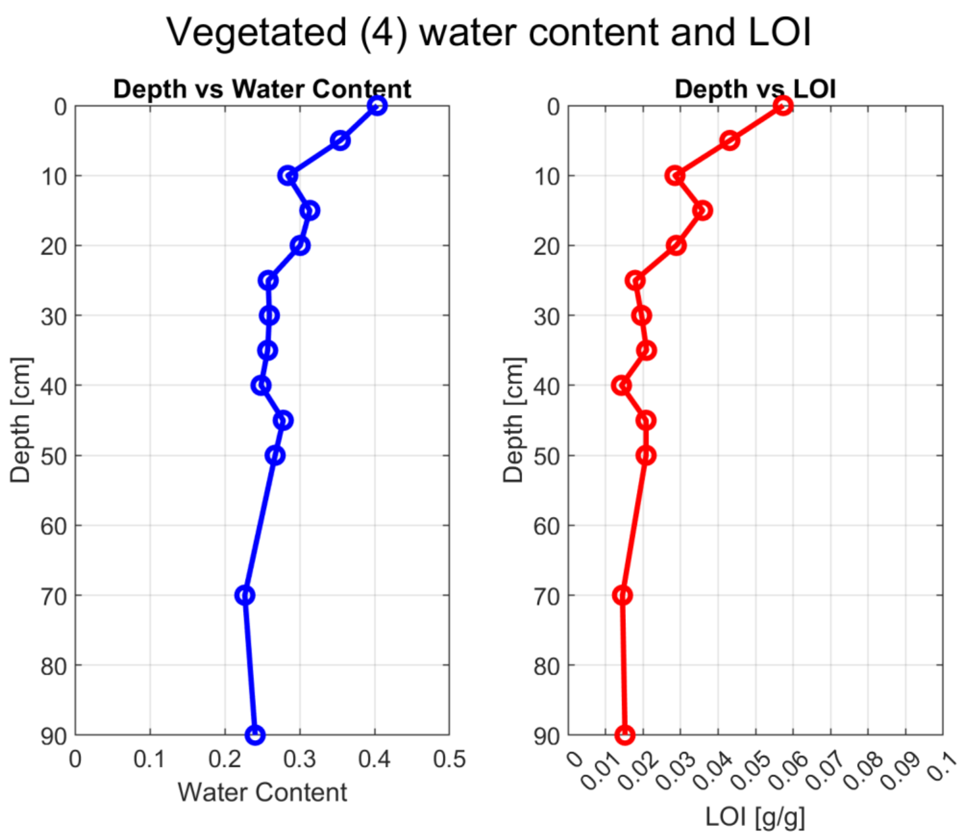

Figure 4.39: Water content and LOI (g/g) of core sample 4 (vegetated).

5 DISCUSSION

This thesis aims to understand the role of plants in preventing salt marsh retreat. Four different methods were employed to support this research, which have been proven valuable in comprehending such a unique environment as salt marshes and appreciating their evolution.

Geophysical surveys were conducted using the seismic refraction method in 2023 and 2024. During both years, measurements on vegetated and non-vegetated soils at low and high tide were taken with vertical geophones (P-wave velocity). In 2024, horizontal geophones were also employed at low tide (SH-wave velocity). The measurements were then observed with FrontEnd Express to do the first break picking and pyGIMLi to obtain each configuration's seismic velocity model.

From the 2023 survey, four models were obtained. Each model shows an increasing velocity gradient with depth. The models for bare soil provide information only for depths of 1 m (low tide) and 0.5 m (high tide), while the model for vegetated soil reaches the computing domain of 1.5 m. The main difference is that the low tide models exhibit higher velocities than the high tide models. This suggests that water infiltrated the subsurface, altering the soil propagation velocities during high tide. It is important to note that each measurement was taken close to the edge of the channel. Therefore, the water infiltration process occurs relatively quickly.

Six models were obtained from the 2024 survey: four during low tide (vertical and horizontal configurations) and two during high tide. In this case, as with the 2023 instance, each model also demonstrates an increasing velocity gradient with depth. The models for the horizontal setup achieve depths of 0.75 m, providing insight into the soil characteristics in its most superficial layer. In the first 75 cm, the bare soil model records higher velocities than the vegetated one. The same behaviour is evident in the vertical configuration. Up to a depth of 1 m, the non-vegetated soil exhibits higher velocities than the vegetated soil at the same depth. This trend reverses at greater depths: the vegetated soil shows higher velocities than the bare soil below 1 m, reaching 1500 m/s compared to 1000 m/s at 1.5 m. These two different behaviours are also observable in the high tide regime. The difference with the 2023 models is that the 2024 high tide models do not differ significantly from their low tide counterparts. This may be because the measurements were taken too soon after the tidal regime transitioned to high tide.

To summarise the trend in the seismic models, the vegetated models exhibit lower velocities in the first metre and higher velocities at greater depths compared to the bare models. This may be due to roots fracturing the soil in the upper layer of the subsurface, resulting in a non-compact layer; hence, the lower velocities. The bare soil is more compact than the vegetated soil, as non-vegetated patches serve as access points for boats descending onto the marsh. The compaction may have resulted from the stamping of people walking in the area. The interesting part is at depths greater than 1 m. A significant difference between bare and vegetated soil suggests that a mechanism of pore water extraction (root suction) might be taking place, as Boaga et al. (2014) suggested. This can be affirmed because the 2024 measurements were taken during the plant's activity in May.

Secondly, a geospatial analysis was conducted using Google Earth Pro for sampling and QGIS for processing and analysis. The initial result obtained was a progressive reduction in the surface area of the San Felice salt marsh between 2004 and 2024. Over 20 years, the total area experienced a nearly linear net loss of 15650 m^2 (1.56 hectares). This may indicate a coupled degradation process: the physical erosion from wind wave action on the marsh margins and land subsidence have contributed to the shrinkage of the marsh area.

The second analysis of the remote sensing method consisted of calculating each bank's migration and migration rate of four different channels: the Gaggian Channel, the San Felice Channel, an artificial channel in the San Felice salt marsh, and the natural channel where geophysical surveys were conducted. The migration was completed for seven-year pairs between 2007 and 2024. A good estimation of the total loss of channel margins can be observed for the pairs 2007-2014 and 2007-2024; the other pairs show there has been soil loss, but quantifying it might be challenging due to georeferencing errors.

Observing Figure 4.30, it is possible to affirm that the southern left bank of the Gaggian Channel experiences higher migration (and hence migration rates) than the southern right bank. The opposite is true for the northern section of the channel, suggesting that the erosion power is stronger on the bank's parts with higher migration values. This suggests that the degradation process in action is due to channel currents and wind waves.

A similar behaviour can be observed for the San Felice Channel: in the southern part of the channel, the left bank has higher migration values than the right bank, and the opposite holds true for the northern part. This may be attributed, once again, to currents and wind wave erosion processes.

It is interesting to observe the artificial and seismic measurements channels, which clearly show higher migration values near the apertures to the San Felice Channel than in other parts of the marsh. The channels that traverse the marsh are sheltered from wind waves, suggesting that the degradation process at work is essentially subsidence, with low migration values (< 3 m). Nonetheless, these values reach 7 m near the San Felice Channel, suggesting that the degradation process also involves wind waves.

While these processes primarily control erosion, the specific mitigating effect of vegetation on channel migration could not be demonstrated unambiguously, mainly due to the absence of non-vegetated marsh surfaces at comparable elevations, which prevented a direct comparison.

The visualised outputs of the combined wind wave-tidal model developed by Carniello et al. (2005, 2011) were presented for 2020, 2021, 2022, 2023 and May 2024 at two different locations (San Felice Channel and the seismic measurements channel). For each year, it is possible to observe that the wave height at each point correlates with the corresponding bottom shear stress: a tall wave height corresponds to great bottom shear stress, while a low wave height is associated with low bottom shear stress. This correlation is also evident in the water level component. All three parameters are interlinked. This indicates that water height is generally associated with similar bottom shear stress, increasing erosion potential. If combined with remote sensing, this could become a potent tool for correlating water level, wave height, and bottom shear stress to erosion rates and channel bank migrations. Furthermore, the sedimentation rate from both storm surges and fluvial inputs is significantly minimised due to the closure of the port branches and the elevation provided by the MOSE system during exceptional storm conditions. Hence, the erosion power surges over the aggradation process.

Four core samples gathered near the geophysical survey’s positions of 2023 and 2024 were the subject of a final analysis. The core samples were processed to assess the water and organic matter content of two vegetated and two non-vegetated marsh patches. The results clearly indicate that, expectably, the vegetated samples have higher organic matter content than non-vegetated samples in the first 70 cm. The water content below this depth is similar in all four samples. It is possible to affirm that the water content follows the organic matter content. Hence, high concentrations of organic matter have high water content. This might give us an ulterior motivation for why the vegetated soil velocity models have lower propagation velocities than bare soils in the first 70 cm.

6 CONCLUSIONS AND FUTURE WORKS

This study integrates geophysical surveys, remote sensing, numerical wave–tidal modelling, and laboratory analyses of soil cores to investigate the role of vegetation in preventing salt marsh retreat, focusing on the San Felice salt marsh in the Venice Lagoon.

The seismic surveys conducted in 2023 and 2024 revealed significant differences in the subsurface mechanical properties between vegetated and non-vegetated soils. In particular, the velocity models for vegetated areas demonstrated that lower velocities in the upper 1 m result from root-induced fracturing and reduced compaction in the shallow layer; higher velocities at greater depths (beyond 1 m) indicate enhanced consolidation and the effect of root suction, as suggested by Boaga et al. (2014).

These findings support the hypothesis that vegetation modifies the surface sediment structure and influences the mechanical behaviour of subsurface materials, potentially mitigating long-term erosion processes.

Geospatial analyses using Google Earth Pro and QGIS have identified a nearly linear decline in the salt marsh area between 2004 and 2024, resulting in a total net loss of 15650 m^2 (1.56 hectares). Detailed examinations of four channels (the Gaggian Channel, the San Felice Channel, an artificial channel, and the channel where geophysical surveys were conducted) indicate differing migration dynamics between the banks of each channel. These variations are likely driven by hydrodynamic forces such as currents, wind waves, and subsidence to a lesser extent. While these processes primarily control erosion, the specific mitigating effect of vegetation on channel migration could not be demonstrated unambiguously, mainly due to the absence of non-vegetated marsh surfaces at comparable elevations, which prevented a direct comparison. Nevertheless, the coherent indications emerging from the integrated analyses suggest that vegetation – and in particular root-induced suction – may contribute to increasing soil mechanical resistance, potentially playing a protective role.

The combined wind wave-tidal model provided the temporal evolution of key parameters (water level, wave height, and total bottom shear stress) at two strategic locations. The outputs demonstrated a strong coupling between water level, wave height, and bottom shear stress, indicating that high tides are associated with elevated wave action and increased erosion potential.

Laboratory processing of soil cores from vegetated and non-vegetated areas revealed that the surface layers (up to 30-40 cm) in vegetated patches contain nearly double the organic matter content compared to non-vegetated areas. The water content exhibits a similar trend, reinforcing the observation that a high concentration of organic matter is associated with higher water content. These findings may help explain the lower seismic velocities observed in the upper layers of vegetated soil models.

The study demonstrates that salt marsh vegetation can alter the subsurface mechanical properties. However, the erosion of channel banks, observed through remote sensing, appears to be governed mainly by hydrodynamic forces rather than by the presence of vegetation.

While the outcomes of this research provide valuable insights into salt marsh dynamics and the potential protective role of vegetation, several possibilities for further study remain. One suggestion is to increase the number of geophones to obtain higher-resolution seismic models and better characterise subsurface layering, along with electrical resistivity tomography (ERT), as Boaga et al. (2014) proposed.

For the remote sensing investigation, it would be intriguing to equip the area with georeferenced reflectors, commence drone surveys, and apply time-series analysis to the results obtained from each yearly survey. This could prevent georeferencing errors and simultaneously achieve very high resolution. It could also help monitor the vegetative changes in the marsh. Furthermore, it would be interesting to correlate the results obtained with remote sensing to the wind wave-tidal model, in order to understand when stronger erosional power takes action.

Realising analogue models and conducting controlled laboratory experiments could be the key to further investigating the interactions between vegetation, sediments, and wave action, particularly focusing on root suction and mechanical stabilisation at various depths – processes that, based on the current results, appear promising and consistent across the different methods employed. Moreover, the development and validation of numerical models that integrate vegetation dynamics (growth, regeneration, stress responses) with morphodynamic evolution of the marsh could be effective.

All these ideas should be extended to the other salt marshes in the Venice Lagoon and other parts of the world to assess whether the observed dynamics are generalisable or specific to local conditions, thereby providing a broader context for the protective role of vegetation.

In summary, this work provides an integrated and quantitative overview of the processes contributing to salt marsh retreat, highlighting the protective role that vegetation may play in increasing soil mechanical resistance and potentially mitigating erosion. The consistency of results across different methods – field observations, remote sensing data analyses, geophysical surveys with numerical modelling, hydrodynamic modelling, and sediment core analysis – supports this hypothesis. Nevertheless, the inherent complexity of these systems and the difficulty of performing direct comparisons with non-vegetated marshes call for further interdisciplinary research to consolidate these findings and translate them into sustainable coastal management practices

APPENDIX A

The following pages describe the plants in the San Felice salt marsh area. All the descriptions refer to the book of Anoè et al., 1984.

Table A.1: Abbreviations used.

fi	fr	in	rad	ra	se	sp
fiore/ flower	frutto/ fruit	infiorescenza/ inflorescence	radice/ root	ramo/ branch	seme/ seed	spighetta/ spikelet

INULA CRITHMOIDES Perennial (hemicryptophyte) plant 40 to 70 cm tall, with a woody stem at the base. The leaves are fleshy, glabrous, and linear-obtuse, with the tips featuring three characteristic small teeth. The yellow flowers are gathered in flower heads (3 cm in diameter) borne on hollow, thickened peduncles covered by scale-like bracts. The fruits are achenes provided with a reddish pappus. It blooms from June to October–November.	

LIMONOIUM NARBONENSE

It is a perennial (hemicryptophyte) plant, 30 to 70 cm tall, with elongated basal leaves arranged in a rosette. The small purple flowers are grouped in a dense panicle, which is very showy during the flowering period from June to September.

SUÆDA MARITIMA

An annual plant (therophyte) with an erect or prostrate, striated stem and branches that droop towards the apex, reaching a 20–60 cm height. The fleshy leaves, semicircular in cross-section, change to a reddish-purple colour in autumn. The flowers are clustered in groups of 2–5 or can appear solitary in the axils of leaves on the upper branches of the plant.

The fruit is oval and compressed. It blooms from July to September.

JUNCUS MARITIMUS

It is a bushy perennial (geophyte) plant similar to *Juncus acutus*, but less prickly and smaller. The stems and leaves, which are green, are cylindrical, solid, and rigid. The inflorescence is also green, not very dense, with green or yellowish flowers. The fruit is an olive-brown capsule. It blooms from April to October.

HALIMIONE PORTULACOIDES

It is a perennial plant with a bushy habit (chamaephyte) that can reach a height of 20–50 cm. The stem is woody and prostrate. The leaves, 3 to 6 cm long and about 1 cm wide, are somewhat fleshy, glaucous, arranged oppositely, and their shape varies from lanceolate to spatulate. The small flowers are sessile and are grouped in panicles, sometimes intermixed with leaves. It blooms from June to July.

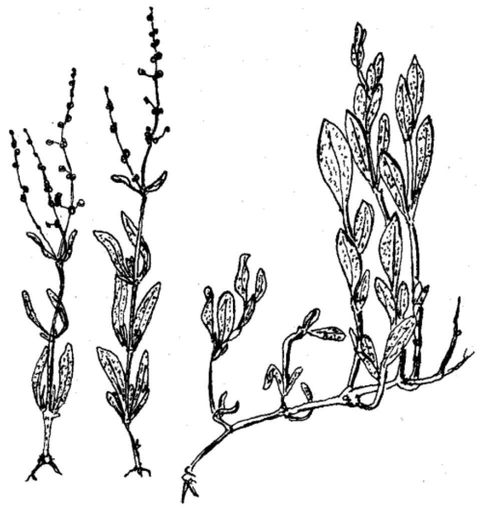

PUCCINELLIA PALUSTRIS

A bushy plant (hemicryptophyte) with numerous erect stems, reaching 20–60 cm. The leaves are convoluted and rush-like, measuring 2–4 mm. The flowers are arranged in a broad, pyramidal panicle, composed of violet spikelets. It blooms from June to September.

SARCOCORNIA FRUTICOSA

It is a small perennial shrub that can grow up to 1 metre. Its glaucous green colour changes to red in autumn. It branches profusely, with numerous stems arising opposite each other, and its overall shape vaguely resembles that of coral.

The stems and branches consist of cylindrical segments measuring a few millimetres long. The fleshy, cylindrical leaves—resembling the stem—are arranged in opposite pairs in a decussate pattern that alternates crosswise.

The flowers, which are pretty modest and barely visible, are arranged in groups of three, with the central one larger than the other two. They are located in the axils of certain leaves and appear to be nestled in small niches, requiring a good magnifying lens to observe them.

The flowering period spans from summer to autumn, a trait that aids in easily identifying the related species Arhrocnemum glaucum (Delile) Ung.-Sternb, which, in contrast, blooms from spring to summer.

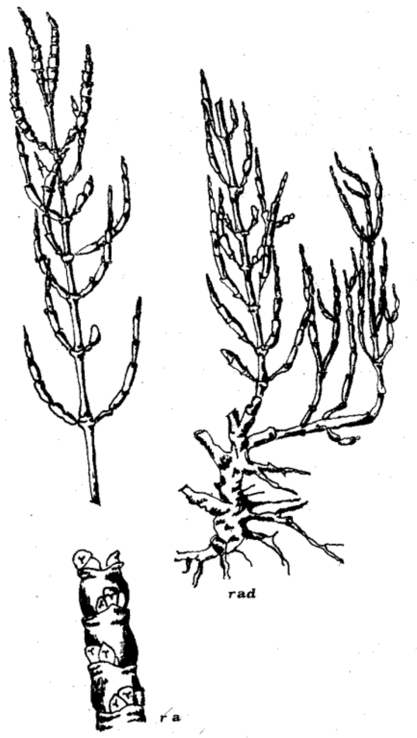

APPENDIX B

The enlarged version of the graphs presented in chapter 4.2 is reported on the following pages for better visualisation.

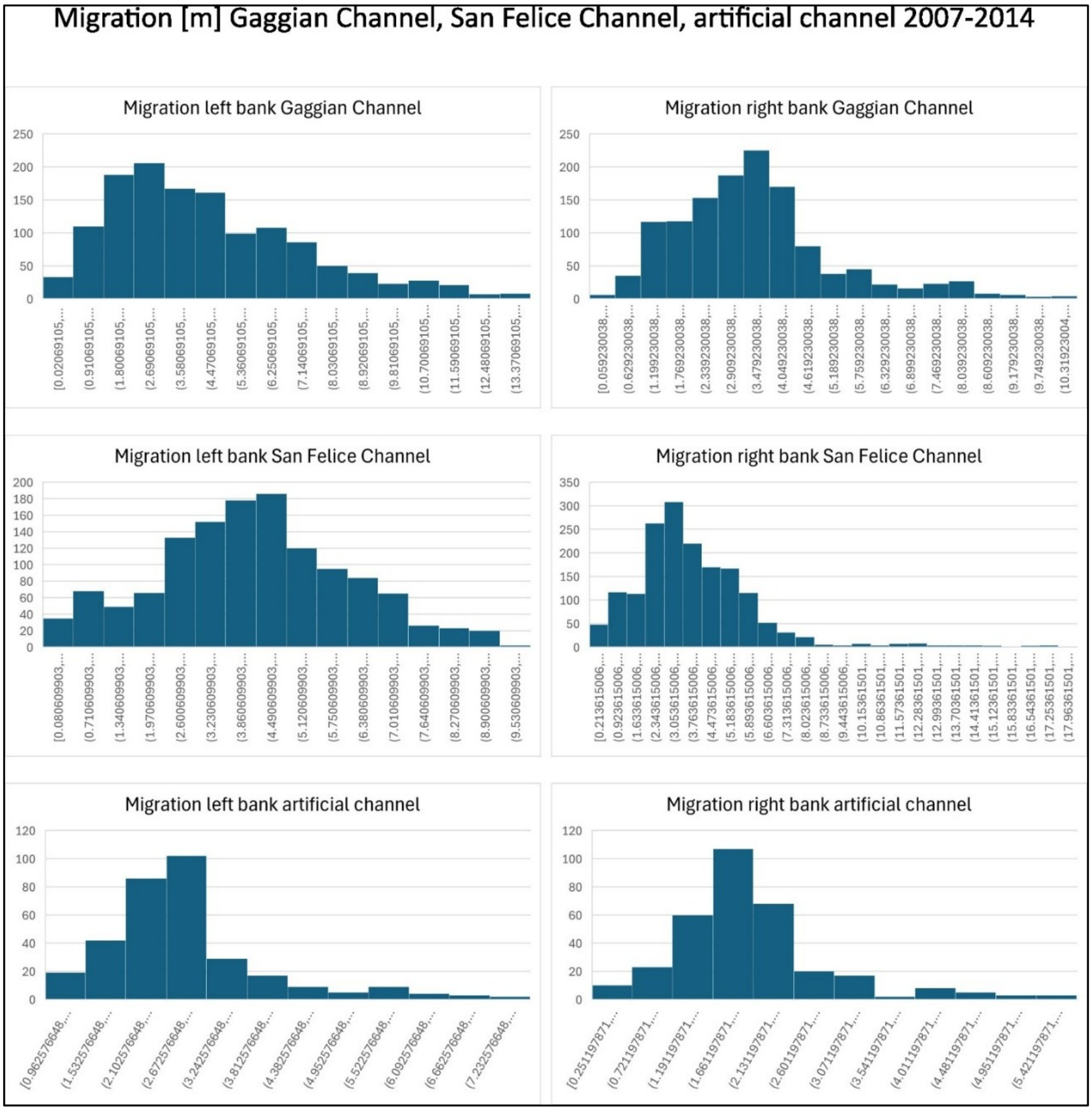

Figure B.1: Enlarged version of Figure 4.17, left top panel. Distribution of channel migration distances (m) for the left and right banks of the Gaggian Channel, San Felice Channel and the artificial channel (2007-2014). Error: 1.87 m.

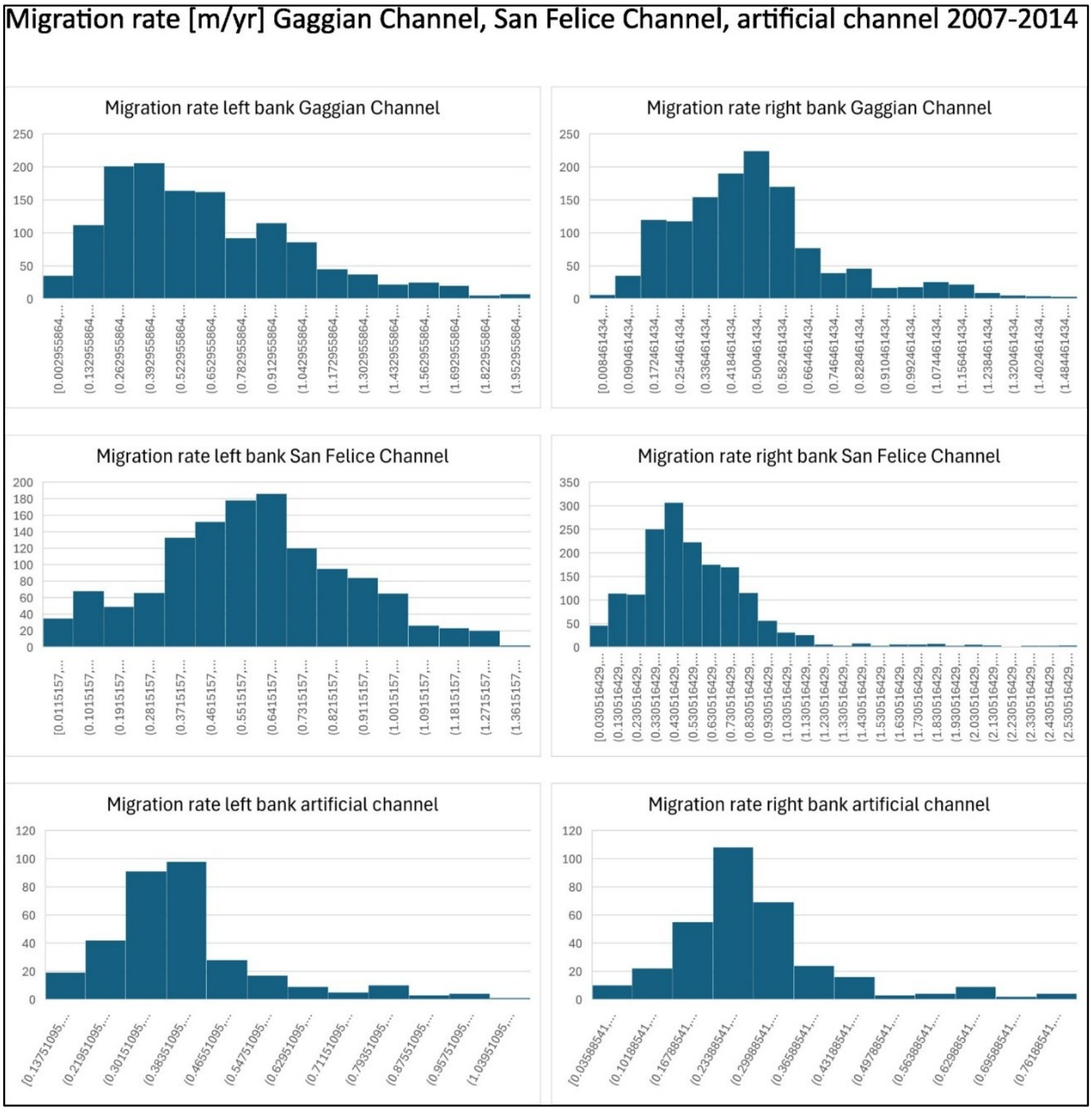

Figure B.2: Enlarged version of Figure 4.17, left bottom panel. Distribution of channel migration rates (m/yr) for the left and right banks of the Gaggian Channel, San Felice Channel and the artificial channel (2007-2014). Error: 1.87 m.

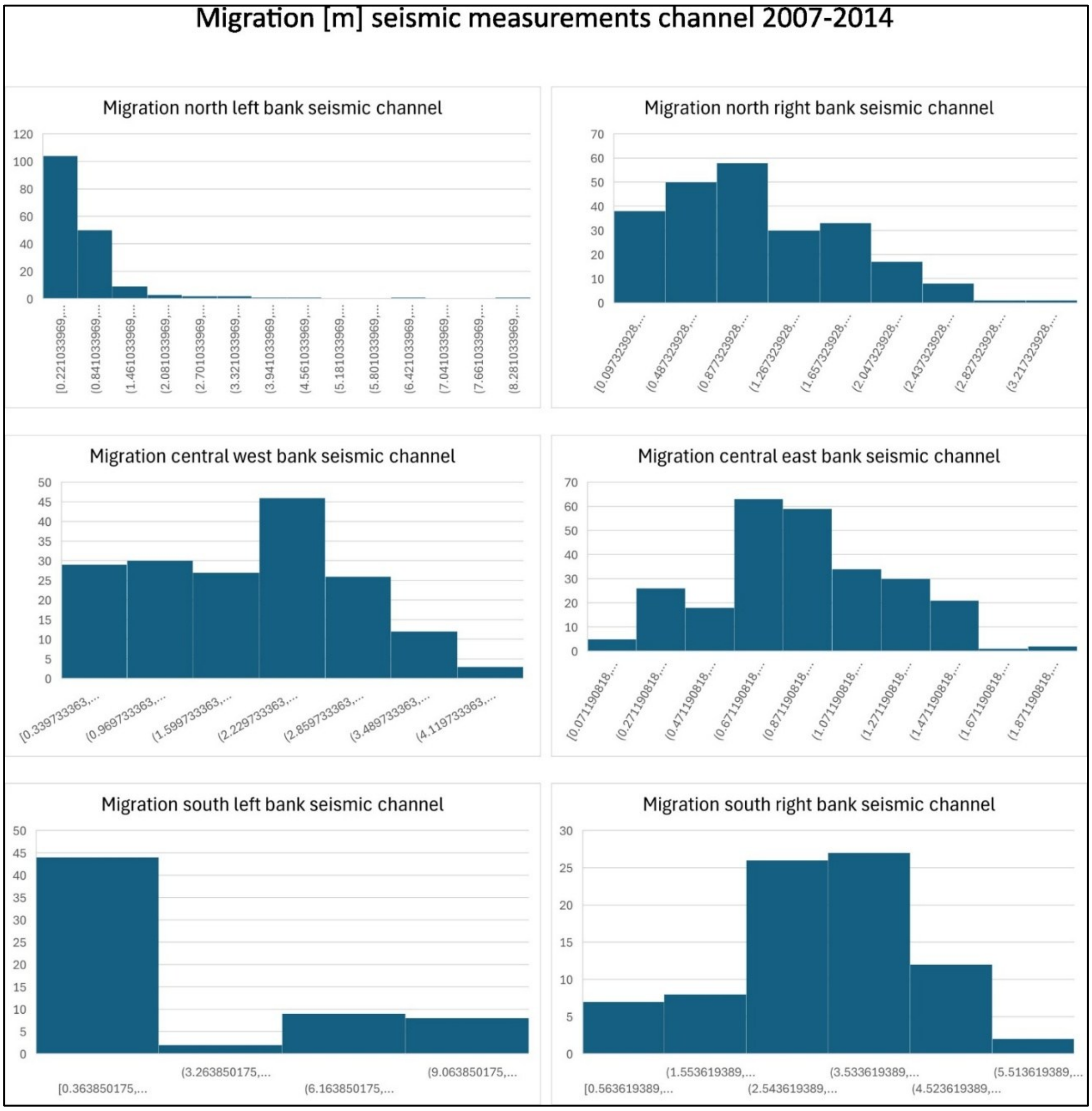

Figure B.3: Enlarged version of Figure 4.17, right top panel. Distribution of channel migration distances (m) for the seismic measurements channel banks subdivided into north, central, and south segments (2007-2014). Error: 1.87 m.

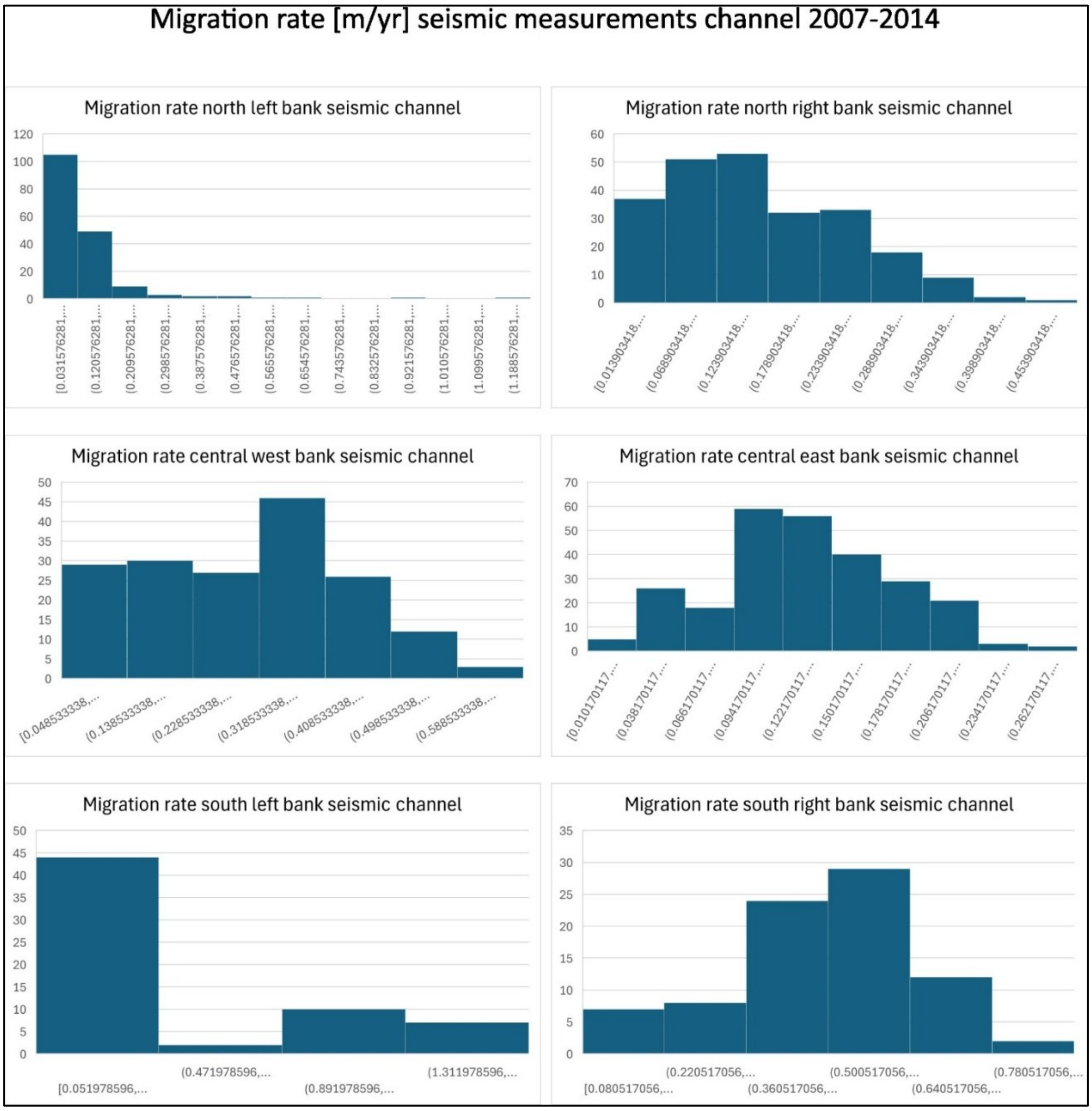

Figure B.4: Enlarged version of Figure 4.17, right bottom panel. Distribution of channel migration rates (m/yr) for the seismic measurements channel banks subdivided into north, central, and south segments (2007-2014). Error: 1.87 m.

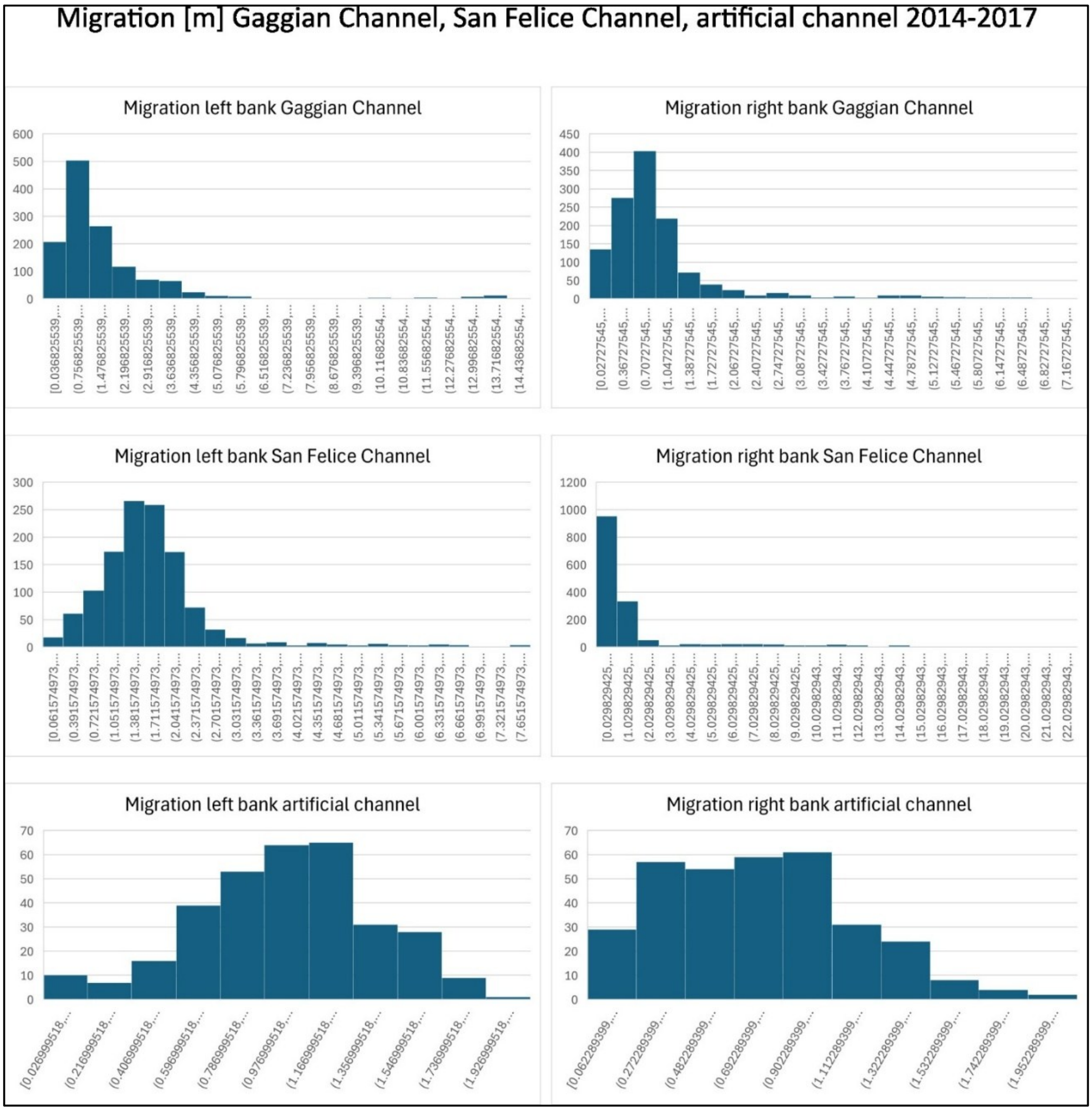

Figure B.5: Enlarged version of Figure 4.19, left top panel. Distribution of channel migration distances (m) for the left and right banks of the Gaggian Channel, San Felice Channel and the artificial channel (2014-2017). Error: 1.45 m.

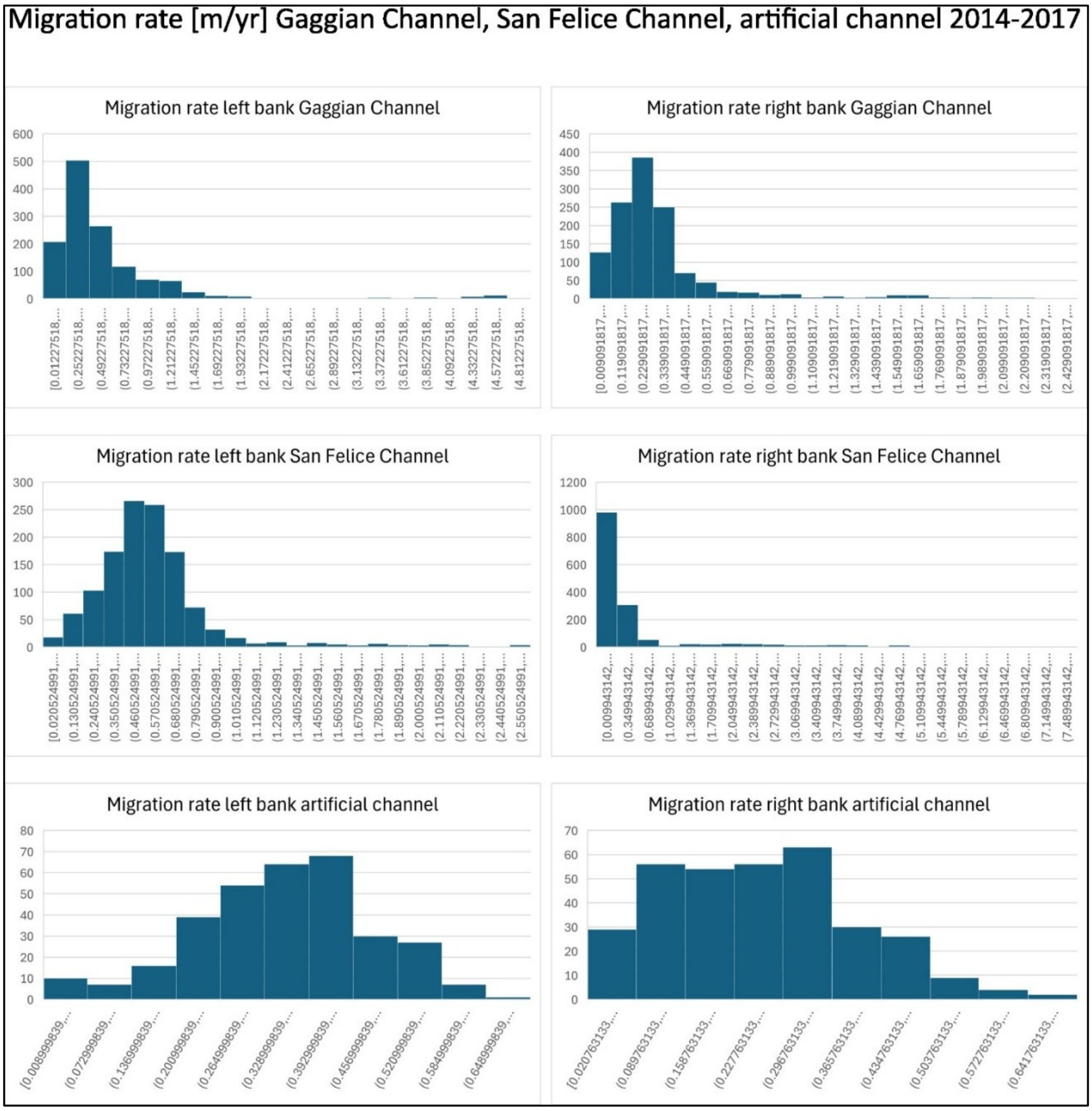

Figure B.6: Enlarged version of Figure 4.19, left bottom panel. Distribution of channel migration rates (m/yr) for the left and right banks of the Gaggian Channel, San Felice Channel and the artificial channel (2014-2017). Error: 1.45 m.

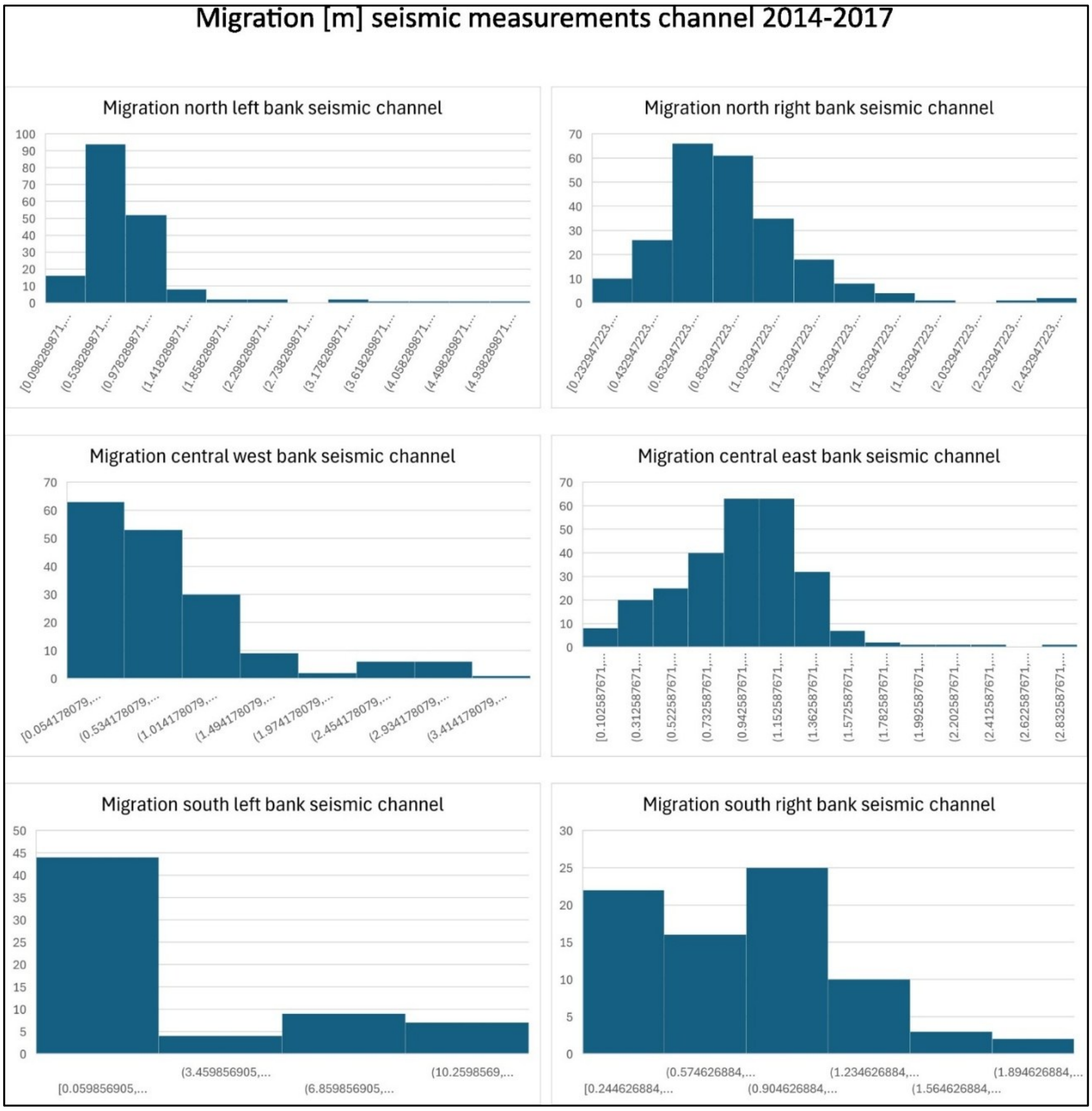

Figure B.7: Enlarged version of Figure 4.19, right top panel. Distribution of channel migration distances (m) for the seismic measurements channel banks subdivided into north, central, and south segments (2014-2017). Error: 1.45 m.

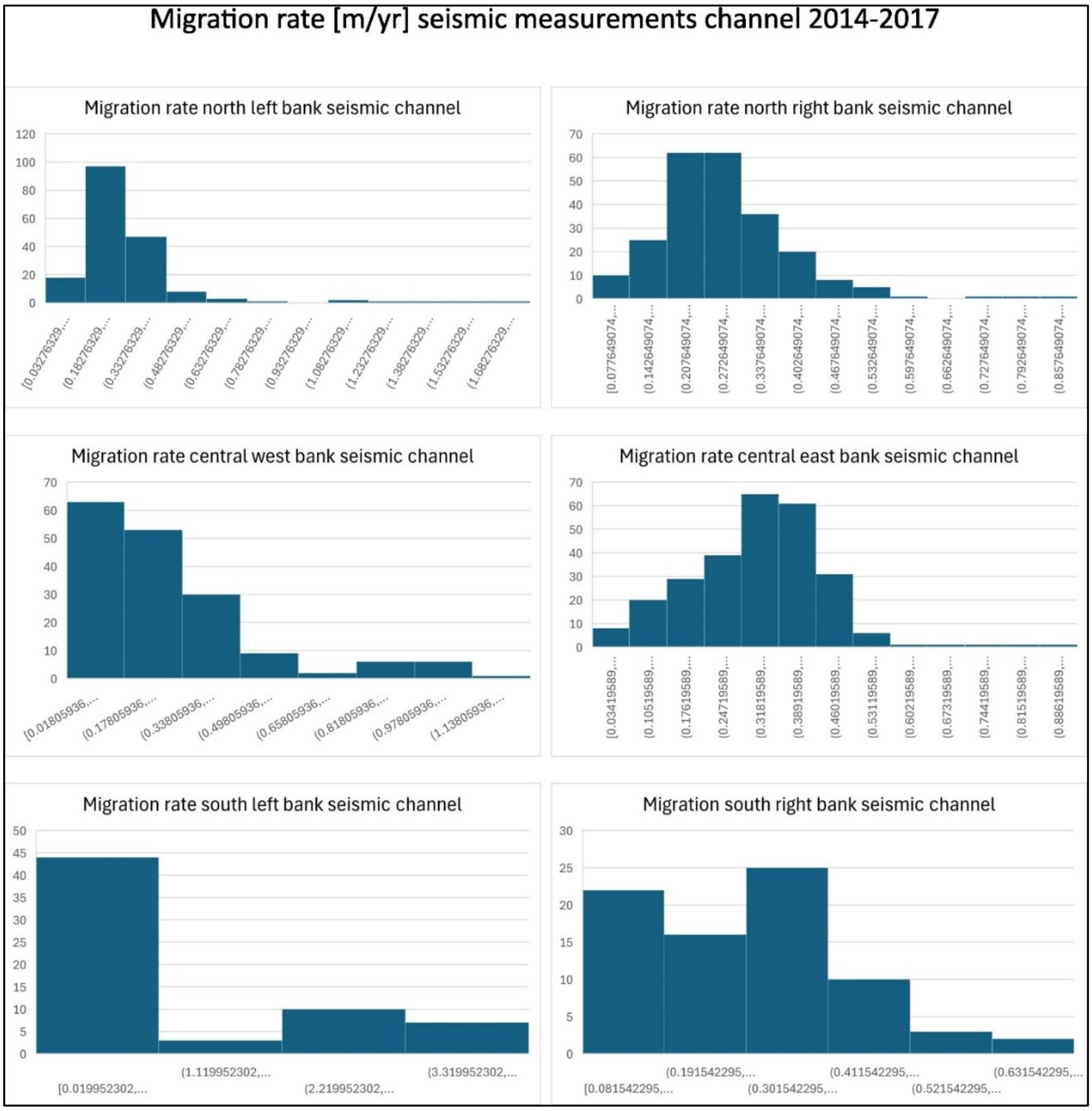

Figure B.8: Enlarged version of Figure 4.19, right bottom panel. Distribution of channel migration rates (m/yr) for the seismic measurements channel banks subdivided into north, central, and south segments (2014-2017). Error: 1.45 m.

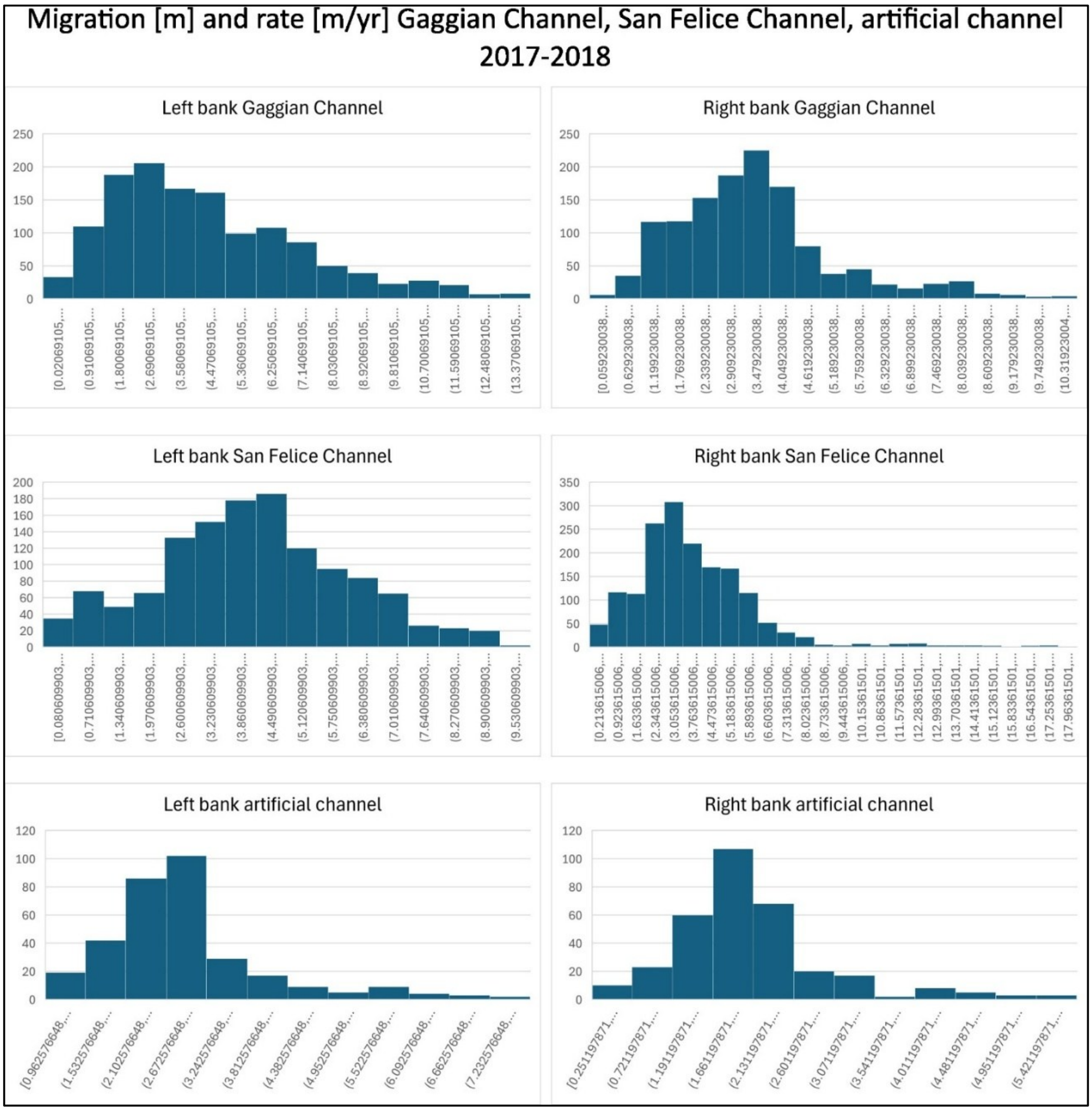

Figure B.9: Enlarged version of Figure 4.21, left panel. Distribution of channel migration distances (m) and rates (m/yr) for the left and right banks of the Gaggian Channel, San Felice Channel and the artificial channel (2017-2018). Error: 0.92 m.

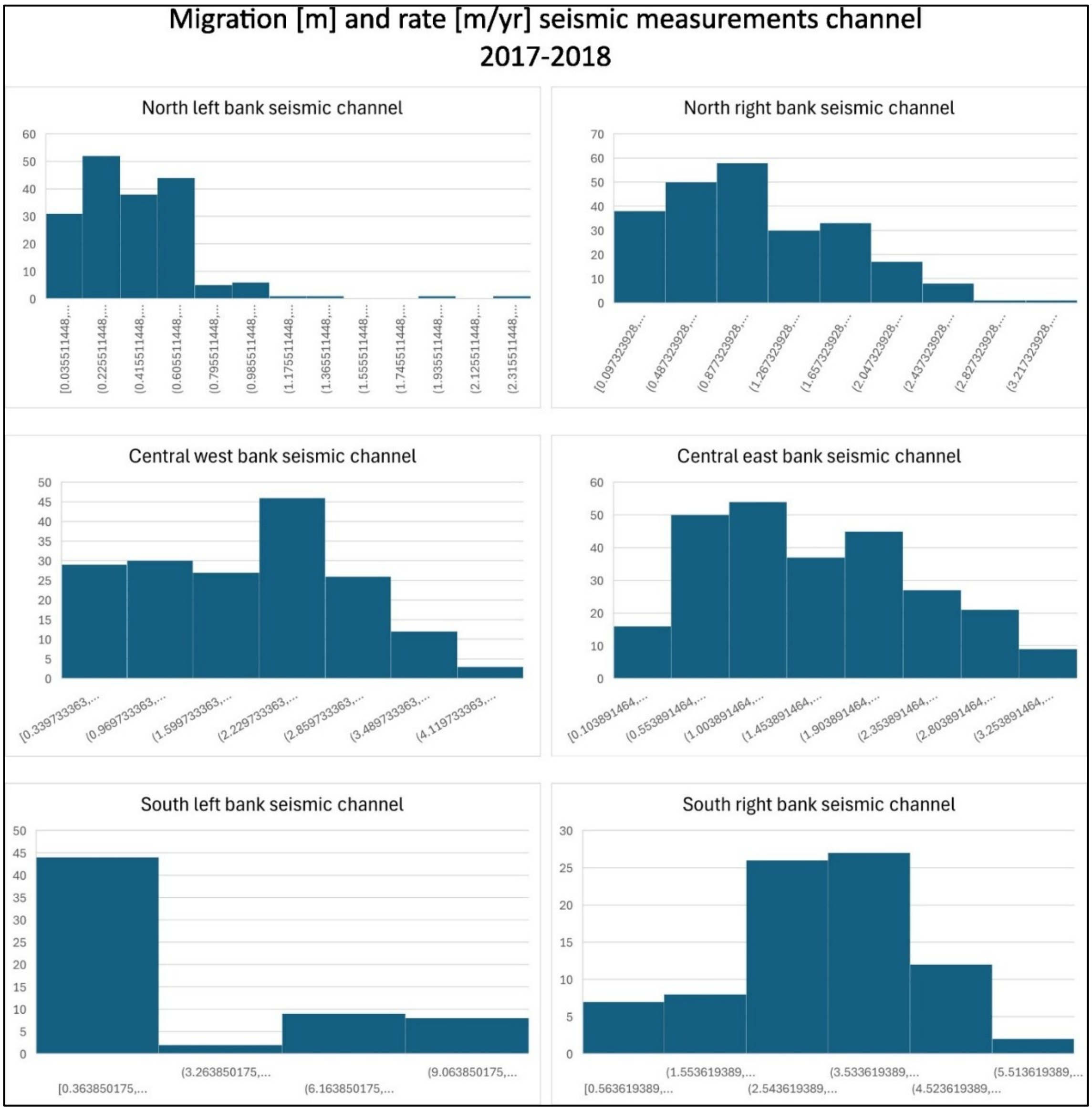

Figure B.10: Enlarged version of Figure 4.21, right panel. Distribution of channel migration distances (m) and rates (m/yr) for the seismic measurements channel banks subdivided into north, central, and south segments (2017-2018). Error: 0.92 m.

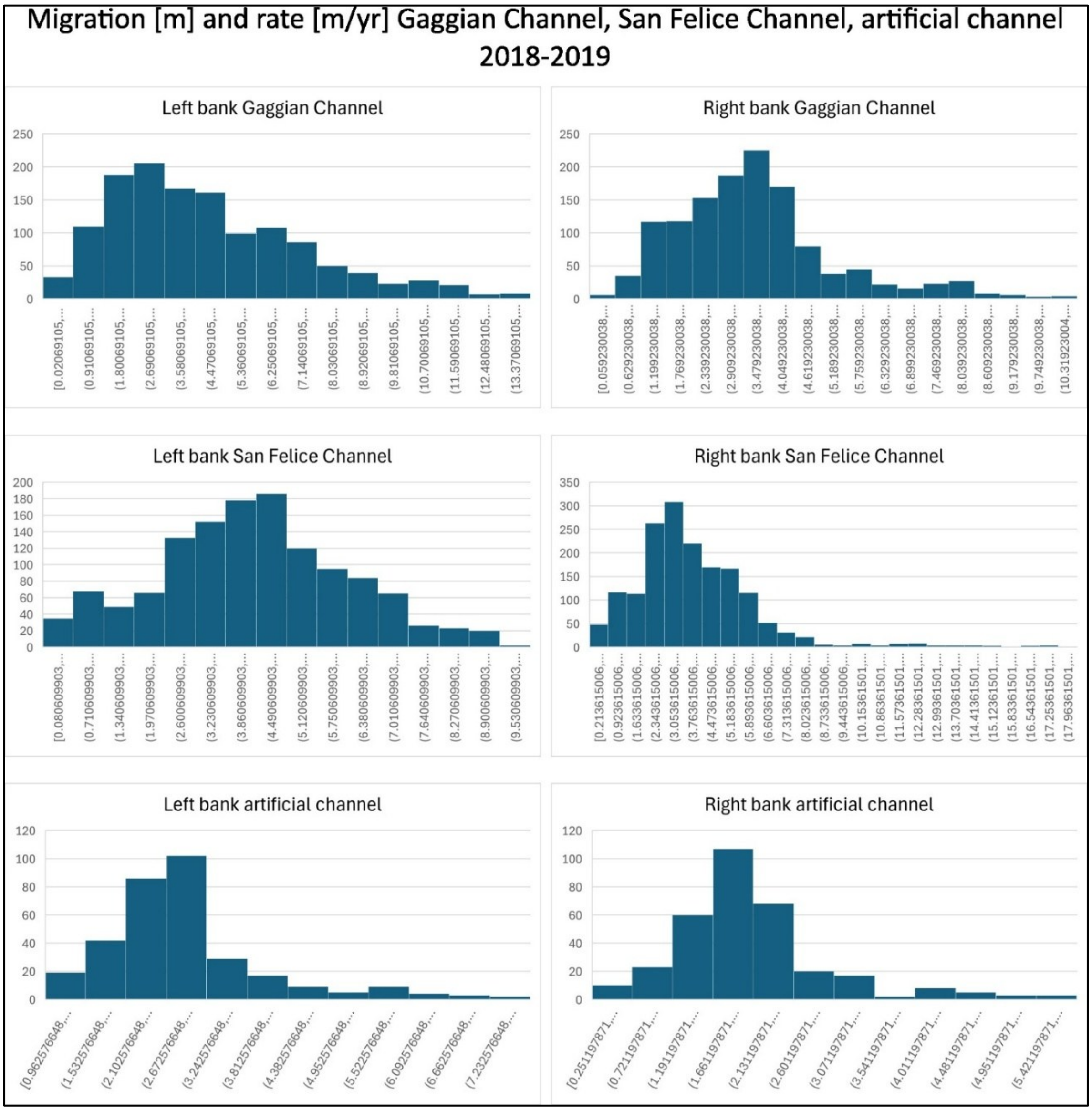

Figure B.11: Enlarged version of Figure 4.23, left panel. Distribution of channel migration distances (m) and rates (m/yr) for the left and right banks of the Gaggian Channel, San Felice Channel and the artificial channel (2018-2019). Error: 1.22 m.

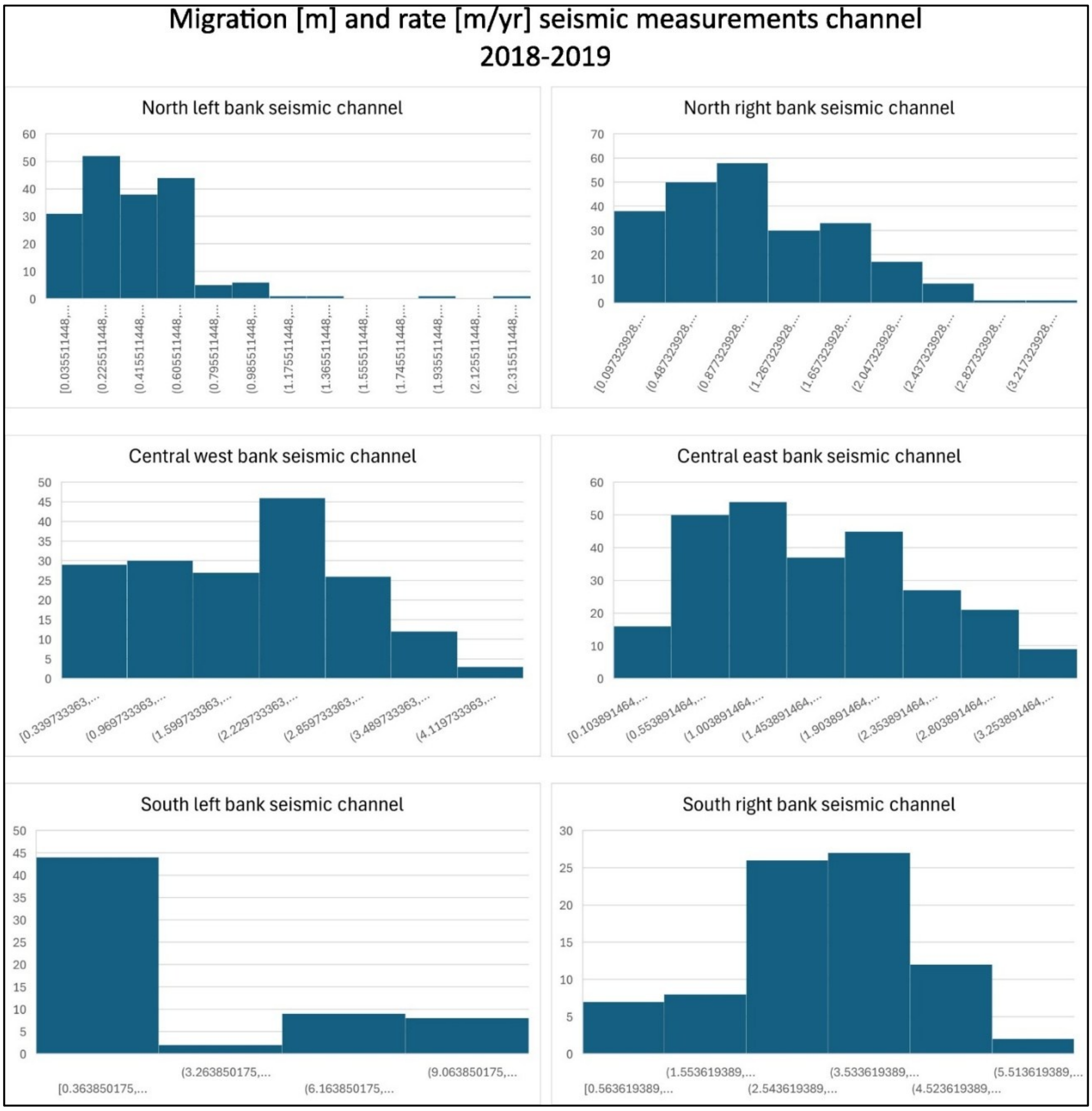

Figure B.12: Enlarged version of Figure 4.23, right panel. Distribution of channel migration distances (m) and rates (m/yr) for the seismic measurements channel banks subdivided into north, central, and south segments (2018-2019). Error: 1.22 m.

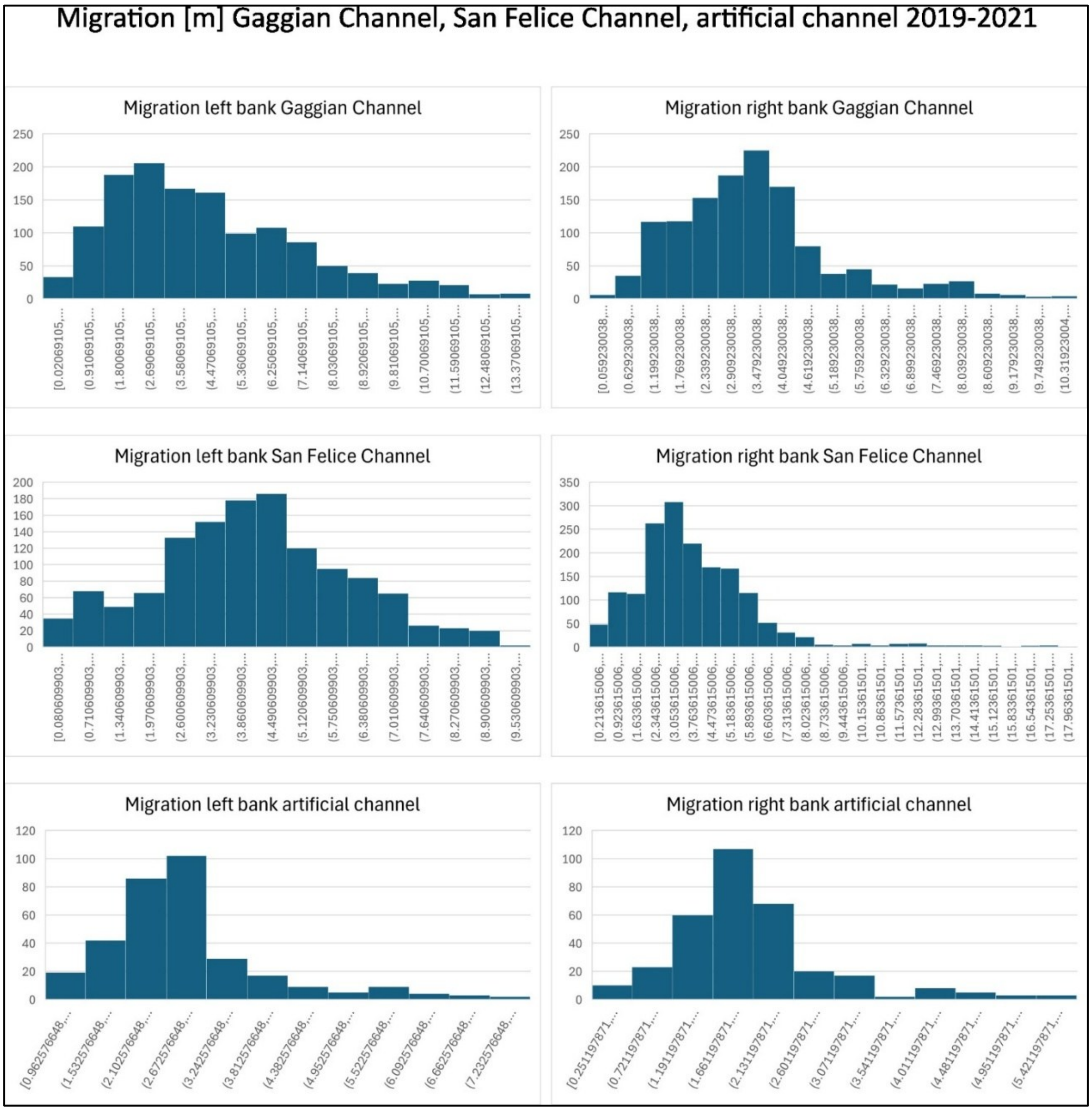

Figure B.13: Enlarged version of Figure 4.25, left top panel. Distribution of channel migration distances (m) for the left and right banks of the Gaggian Channel, San Felice Channel and the artificial channel (2019-2021). Error: 1.13 m.

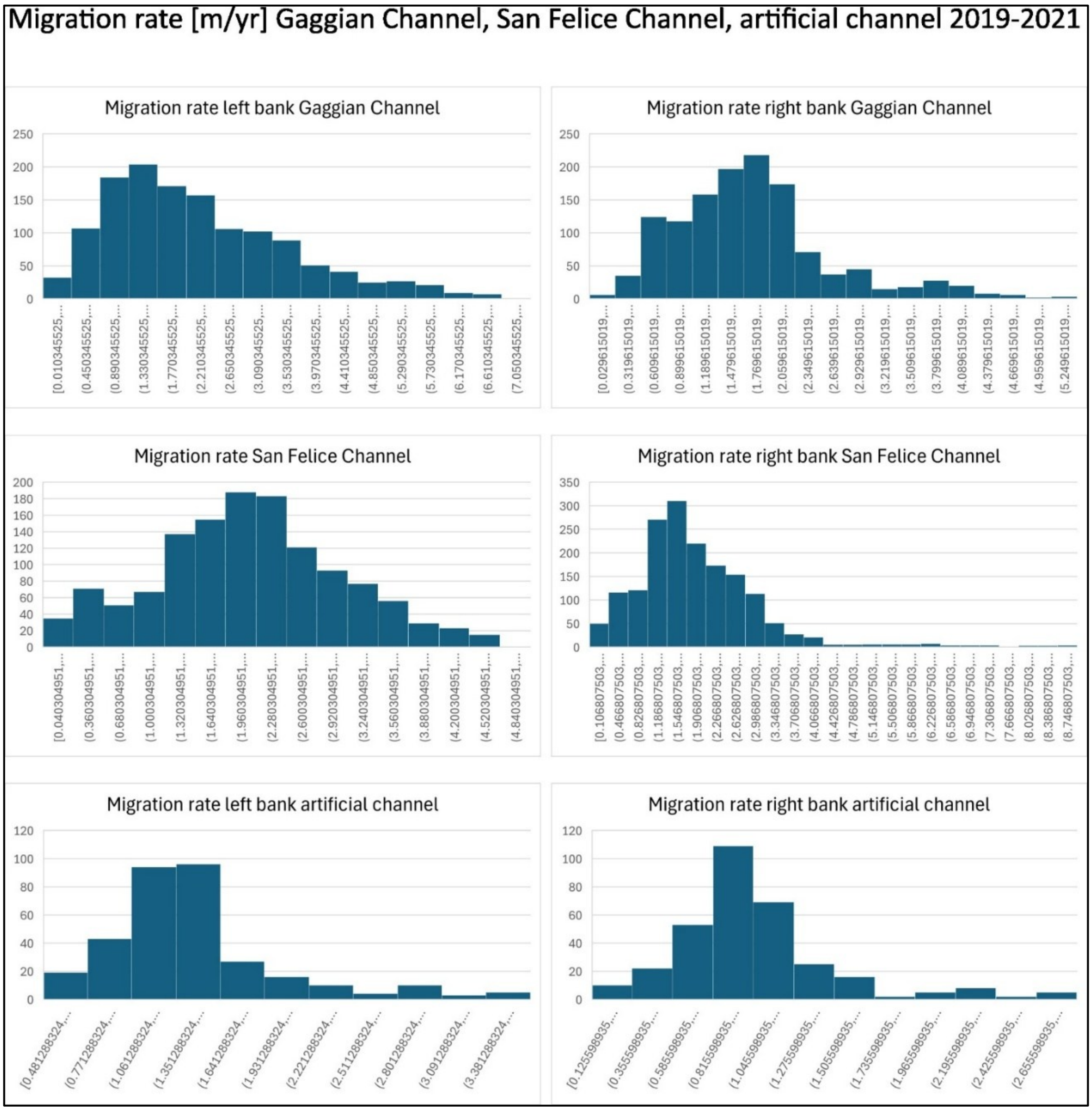

Figure B.14: Enlarged version of Figure 4.25, left bottom panel. Distribution of channel migration rates (m/yr) for the left and right banks of the Gaggian Channel, San Felice Channel and the artificial channel (2019-2021). Error: 1.13 m.

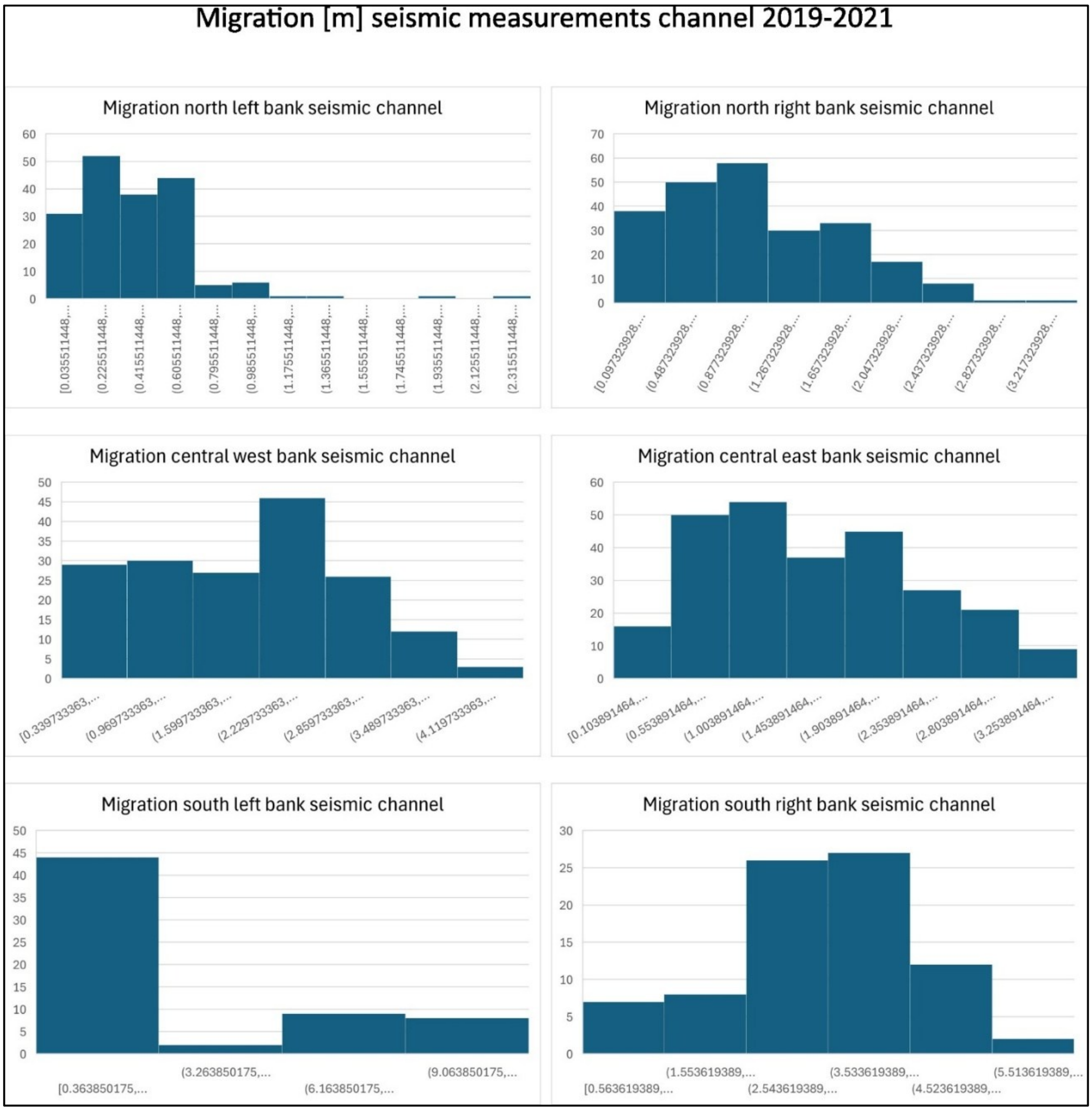

Figure B.15: Enlarged version of Figure 4.25, right top panel. Distribution of channel migration distances (m) for the seismic measurements channel banks subdivided into north, central, and south segments (2019-2021). Error: 1.13 m.

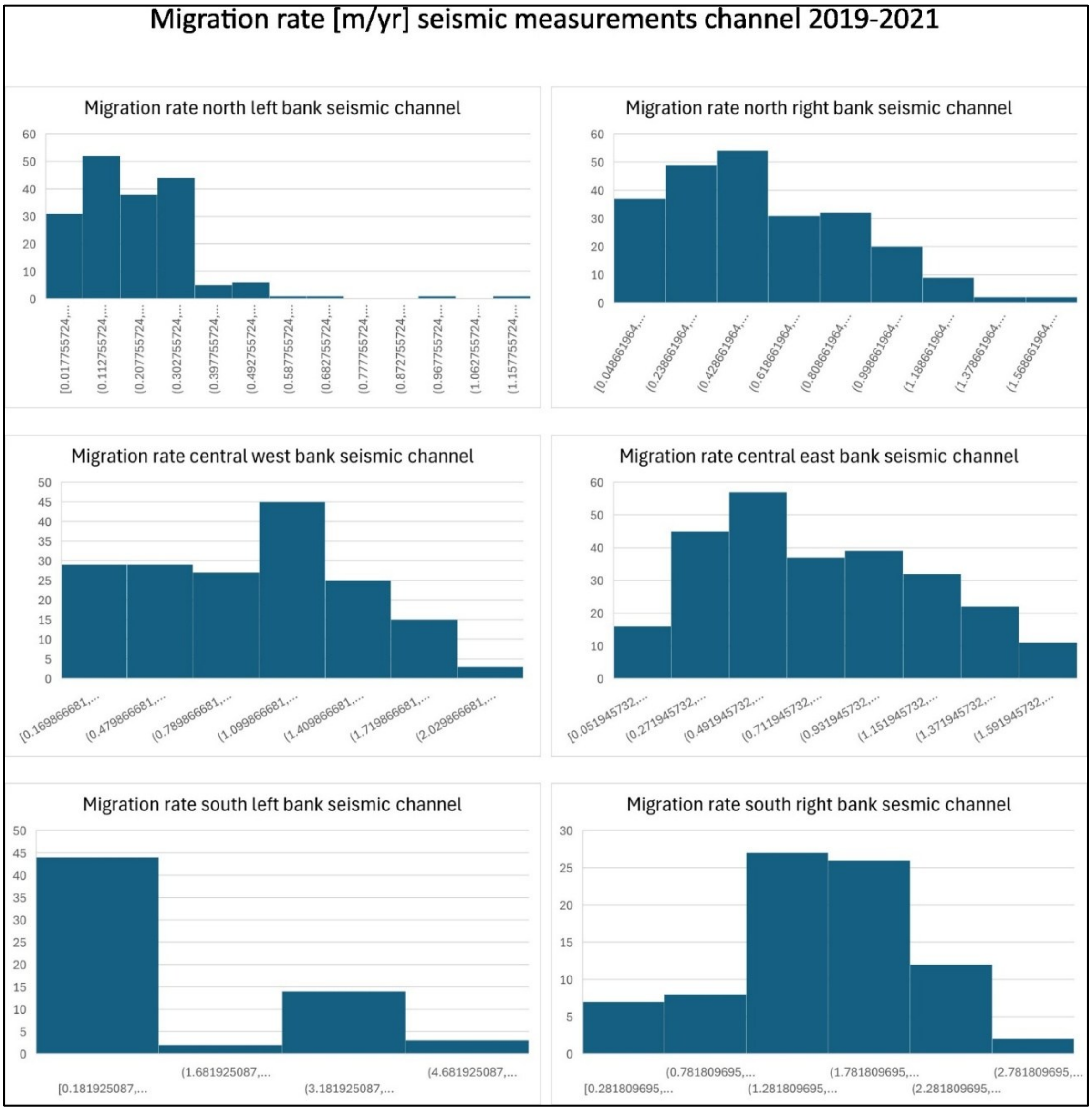

Figure B.16: Enlarged version of Figure 4.25, right bottom panel. Distribution of channel migration rates (m/yr) for the seismic measurements channel banks subdivided into north, central, and south segments (2019-2021). Error: 1.13 m.

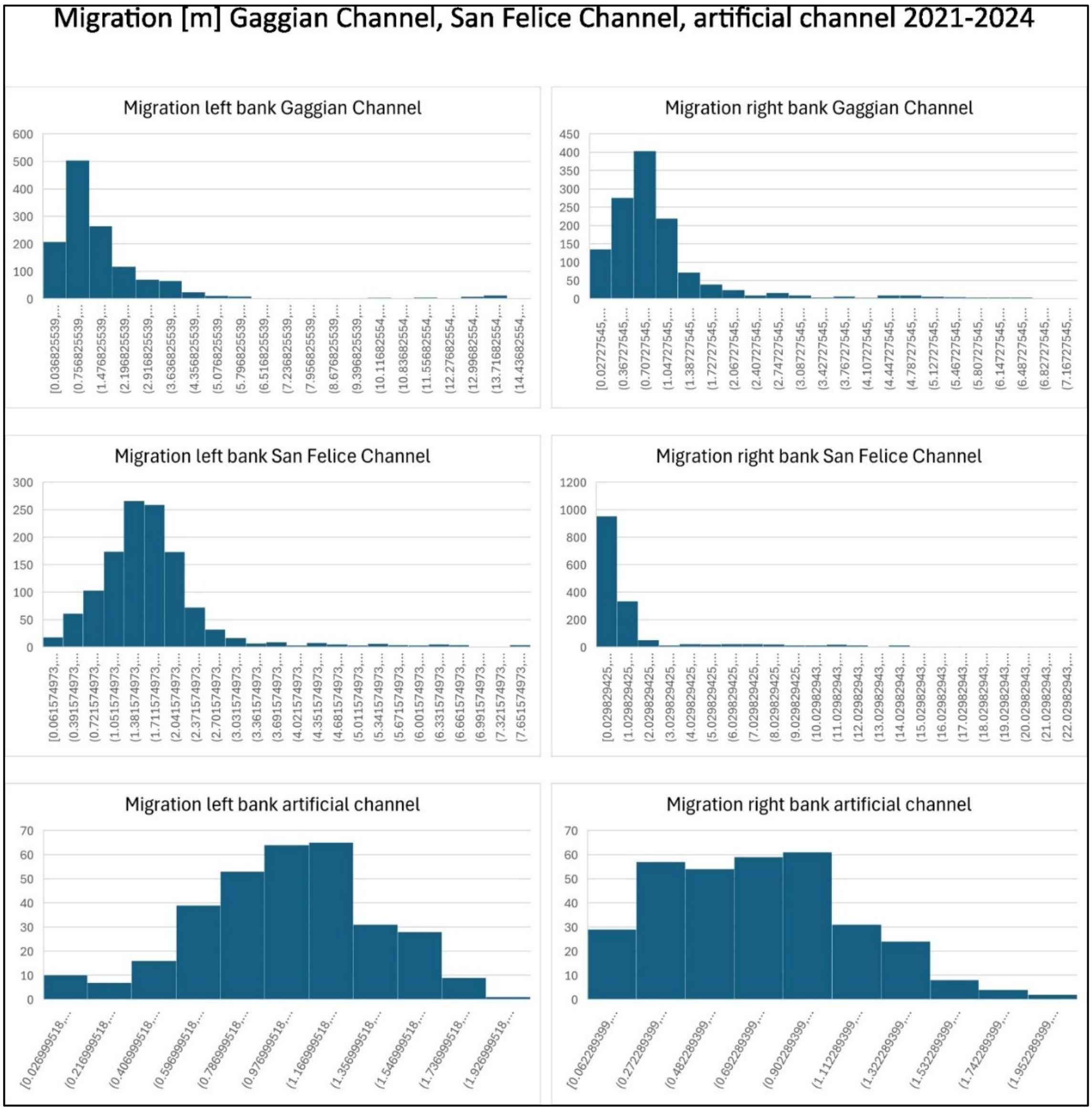

Figure B.17: Enlarged version of Figure 4.27, left top panel. Distribution of channel migration distances (m) for the left and right banks of the Gaggian Channel, San Felice Channel and the artificial channel (2021-2024). Error: 1.73 m.

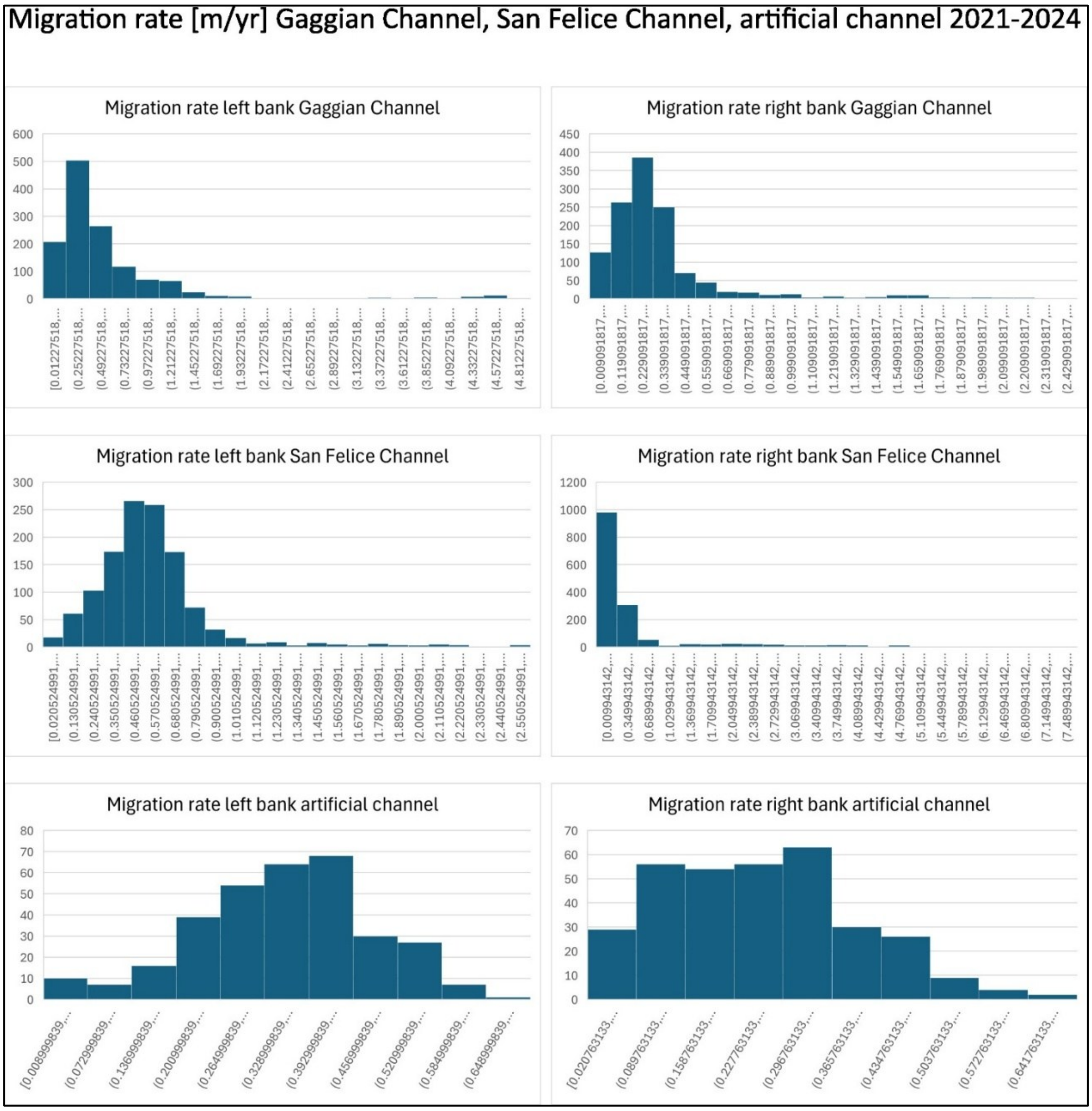

Figure B.18: Enlarged version of Figure 4.27, left bottom panel. Distribution of channel migration rates (m/yr) for the left and right banks of the Gaggian Channel, San Felice Channel and the artificial channel (2021-2024). Error: 1.73 m.

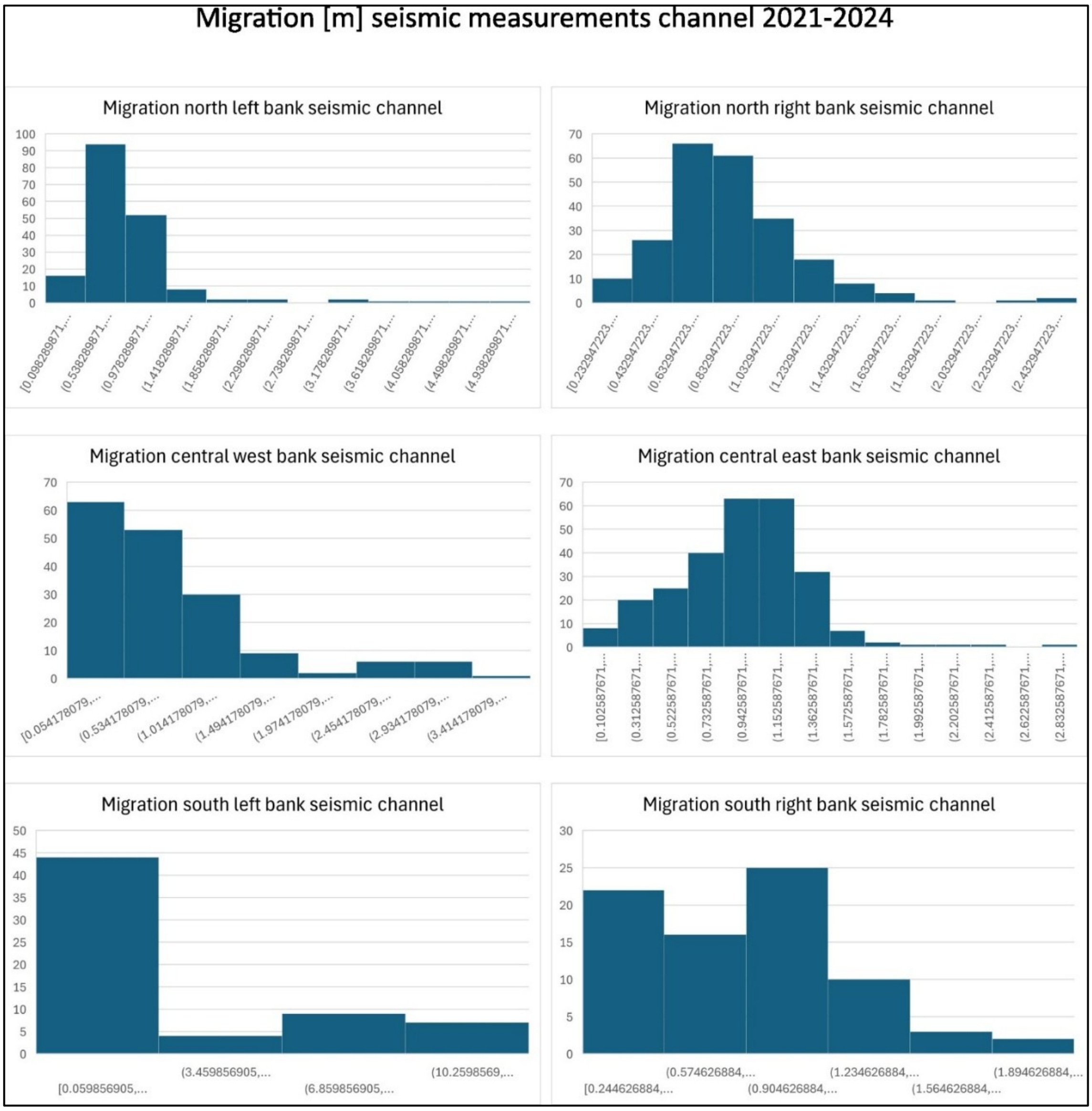

Figure B.19: Enlarged version of Figure 4.27, right top panel. Distribution of channel migration distances (m) for the seismic measurements channel banks subdivided into north, central, and south segments (2021-2024). Error: 1.73 m.

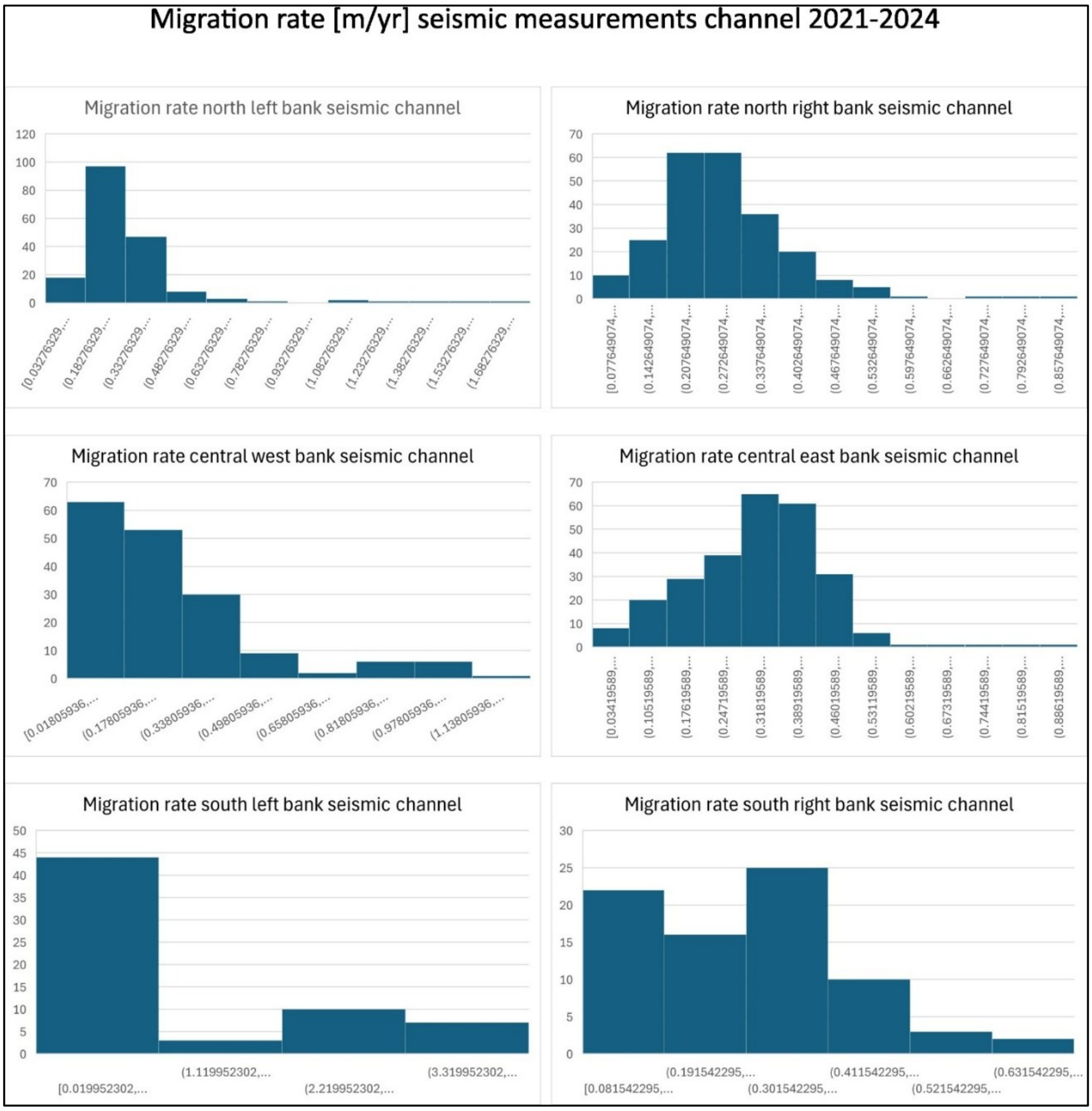

Figure B.20: Enlarged version of Figure 4.27, right bottom panel. Distribution of channel migration rates (m/yr) for the seismic measurements channel banks subdivided into north, central, and south segments (2021-2024). Error: 1.73 m.

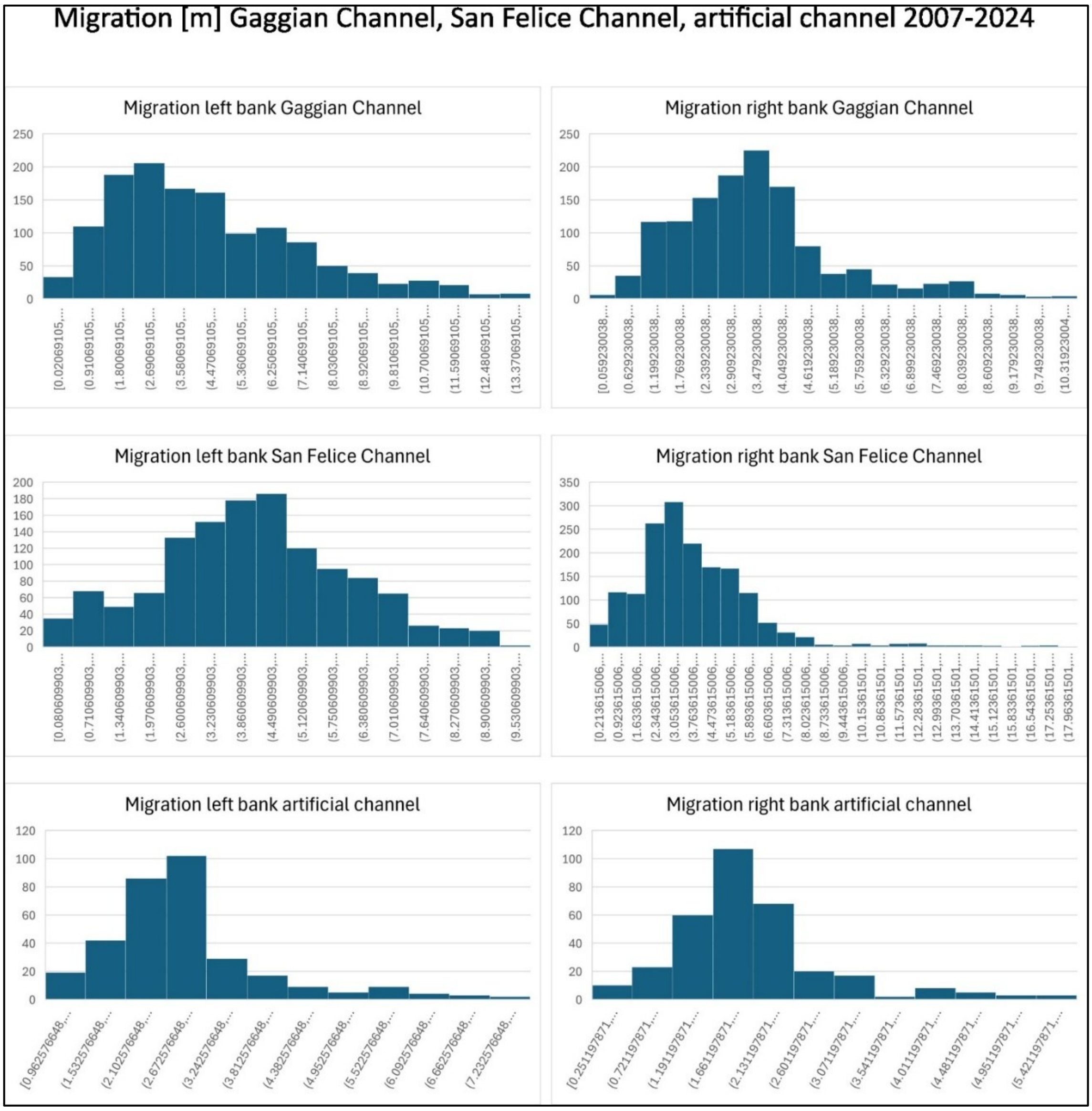

Figure B.21: Enlarged version of Figure 4.29, left top panel. Distribution of channel migration distances (m) for the left and right banks of the Gaggian Channel, San Felice Channel and the artificial channel (2007-2024). Error: 1.67 m.

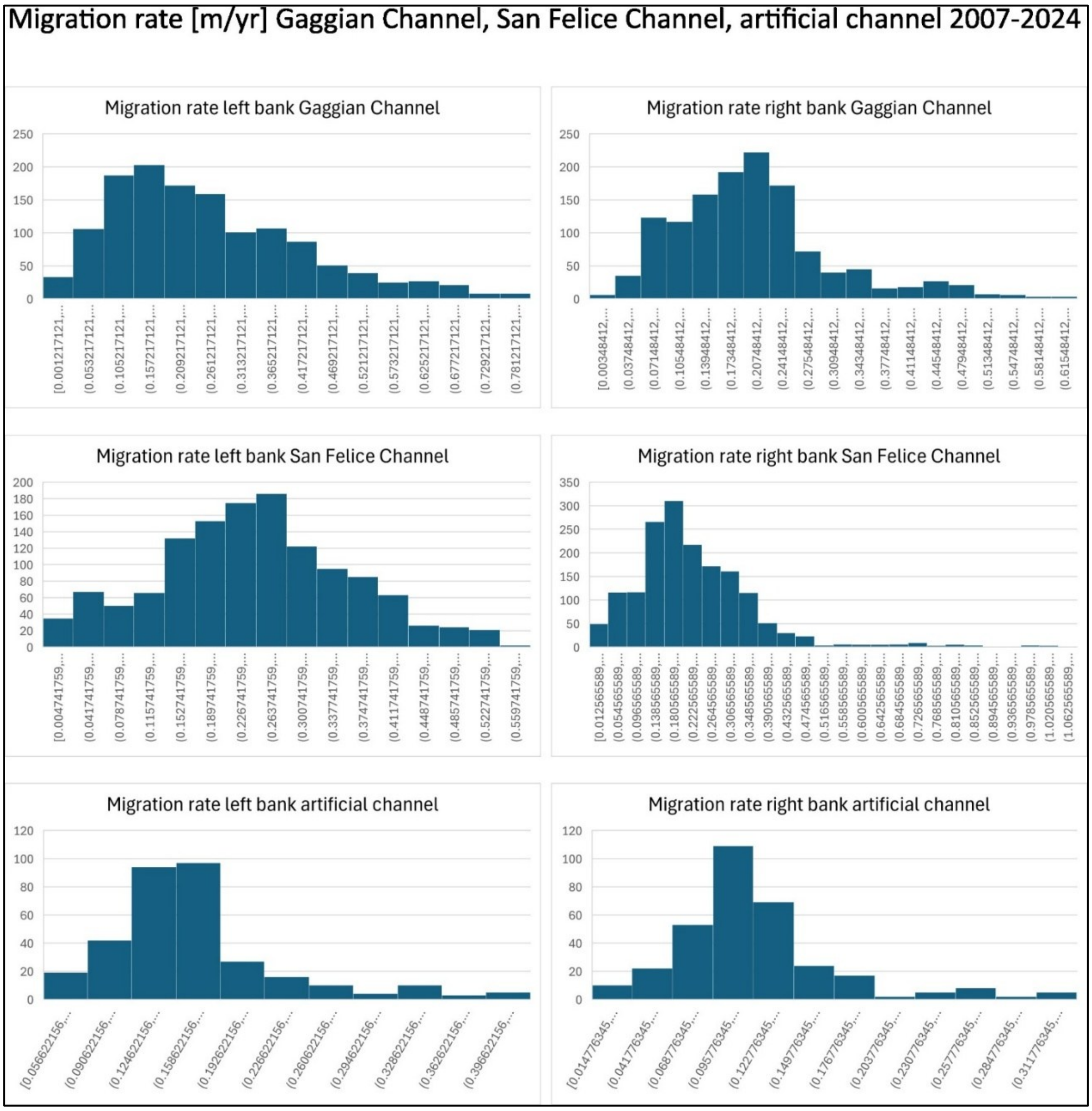

Figure B.22: Enlarged version of Figure 4.29, left bottom panel. Distribution of channel migration rates (m/yr) for the left and right banks of the Gaggian Channel, San Felice Channel and the artificial channel (2007-2024). Error: 1.67 m.

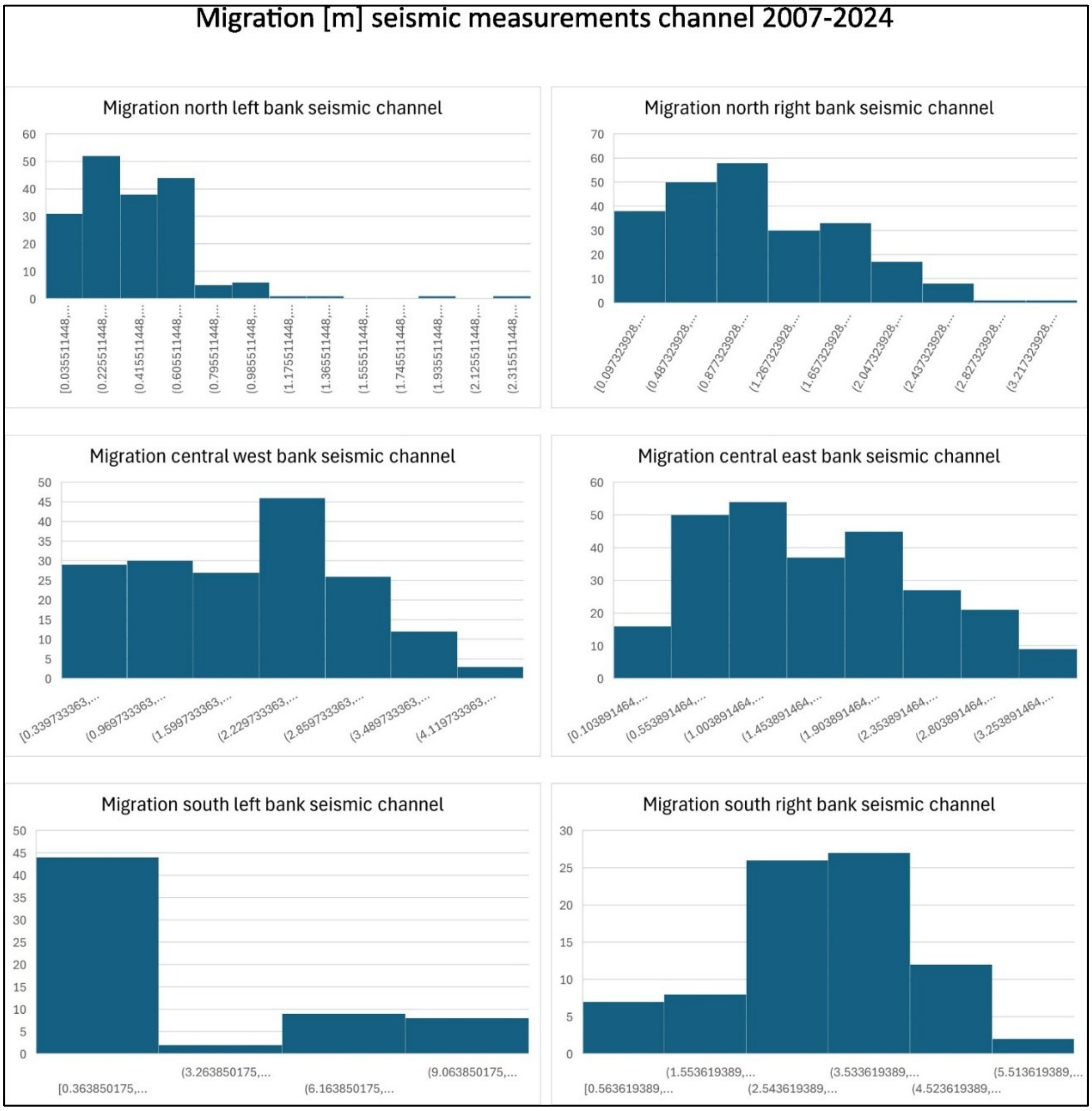

Figure B.23: Enlarged version of Figure 4.29, right top panel. Distribution of channel migration distances (m) for the seismic measurements channel banks subdivided into north, central, and south segments (2007-2024). Error: 1.67 m.

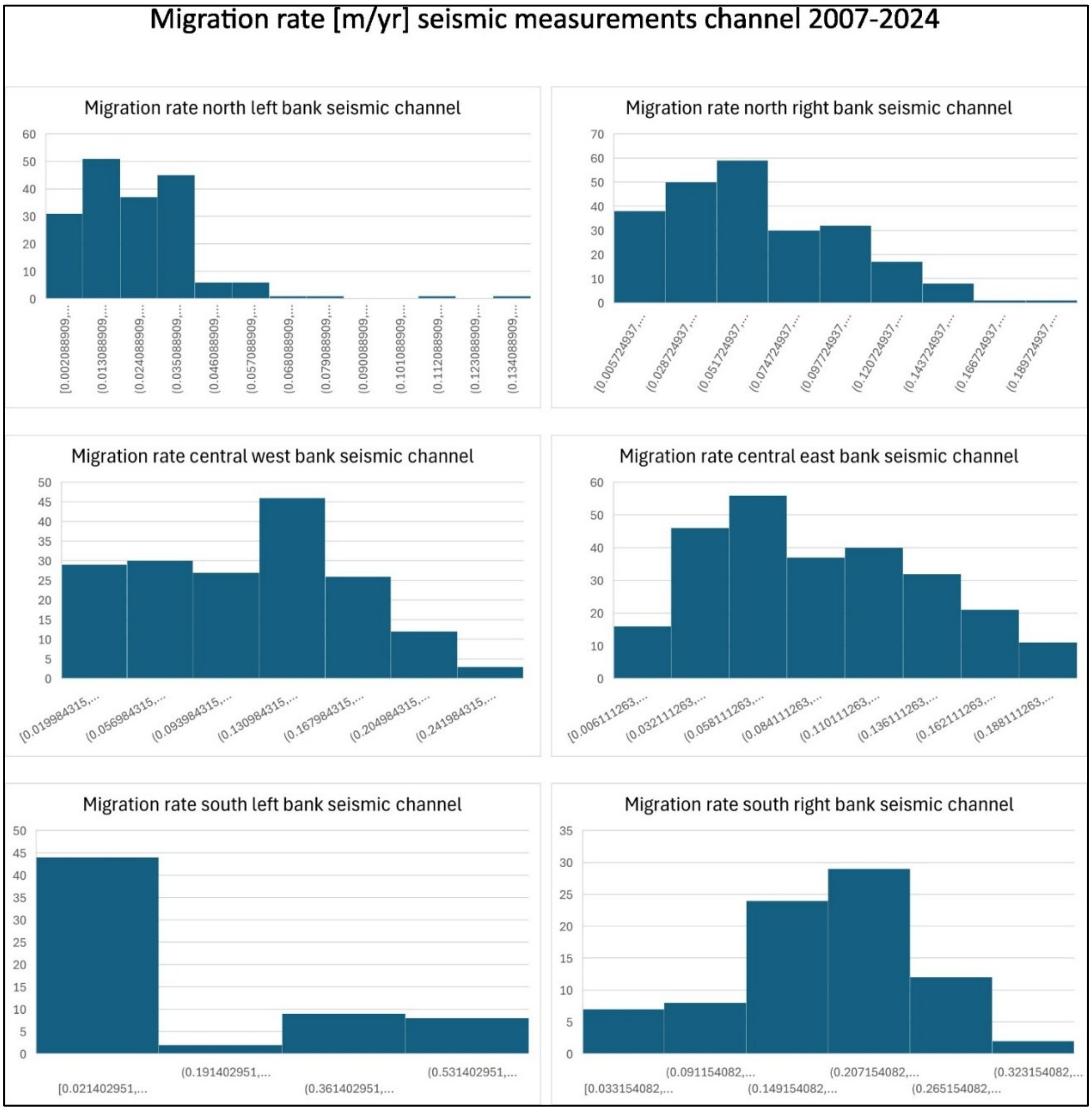

Figure B.24: Enlarged version of Figure 4.29, right bottom panel. Distribution of channel migration rates (m/yr) for the seismic measurements channel banks subdivided into north, central, and south segments (2007-2024). Error: 1.67 m.

REFERENCES

Anoè, N., Calzavara, D., Salviato, L. (1984). Flora e Vegetazione delle Barene, note e schede. *Società Veneziana di Scienze Naturali, lavori*.

Baccarin, M. (2024). Signature of Tidal Processes in Channelized deposits of the Venice Lagoon and Po River Delta (Italy). Master Thesis. *Università degli Studi di Padova*.

Bendoni, M., Francalanci, S., Cappietti, L., & Solari, L. (2014). On salt marshes retreat: Experiments and modeling toppling failures induced by wind waves. *Journal of Geophysical Research: Earth Surface*, *119*(3), 603–620. https://doi.org/10.1002/2013JF002967

Blount, T. R., Carrasco, A. R., Cristina, S., & Silvestri, S. (2022). Exploring open-source multispectral satellite remote sensing as a tool to map long-term evolution of salt marsh shorelines. *Estuarine, Coastal and Shelf Science*, *266*. https://doi.org/10.1016/j.ecss.2021.107664

Blount, T., Silvestri, S., Marani, M., & D'Alpaos, A. (2023). LiDAR DERIVED SALT MARSH TOPOGRAPHY AND BIOMASS: DEFINING ACCURACY AND SPATIAL PATTERNS OF UNCERTAINTY. *International Archives of the Photogrammetry, Remote Sensing and Spatial Information Sciences - ISPRS Archives*, *48*(1/W1-2023), 57–62. https://doi.org/10.5194/isprs-archives-XLVIII-1-W1-2023-57-2023

Boaga, J., D'Alpaos, A., Cassiani, G., Marani, M., & Putti, M. (2014). Plant-Soil interactions in salt marsh environments: Experimental evidence from electrical resistivity tomography in the Venice Lagoon. *Geophysical Research Letters*, *41*(17), 6160–6166. https://doi.org/10.1002/2014GL060983

Cagnin, F. (2024). Metodi microsismici in barene lagunari per la caratterizzazione della rizosfera. Mester thesis. *Università degli Studi di Padova*.

Campbell, A. D., Fatoyinbo, L., Goldberg, L., & Lagomasino, D. (2022). Global hotspots of salt marsh change and carbon emissions. *Nature*, *612*(7941), 701–706. https://doi.org/10.1038/s41586-022-05355-z

Campbell, A., & Wang, Y. (2019). High spatial resolution remote sensing for salt marsh mapping and change analysis at fire Island national seashore. *Remote Sensing*, *11*(9). https://doi.org/10.3390/rs11091107

Carniello, L., D'Alpaos, A., & Defina, A. (2011). Modeling wind waves and tidal flows in shallow micro-tidal basins. *Estuarine, Coastal and Shelf Science*, *92*(2), 263–276. https://doi.org/10.1016/j.ecss.2011.01.001

Carniello, L., Defina, A., & D'Alpaos, L. (2009). Morphological evolution of the Venice lagoon: Evidence from the past and trend for the future. *Journal of Geophysical Research: Earth Surface*, *114*(4). https://doi.org/10.1029/2008JF001157

Carniello, L., Defina, A., Fagherazzi, S., & D'Alpaos, L. (2005). A combined wind wave-tidal model for the Venice lagoon, Italy. *Journal of Geophysical Research: Earth Surface*, *110*(4). https://doi.org/10.1029/2004JF000232

Carrera, A., Barone, I., Pavoni, M., Boaga, J., Dal Ferro, N., Cassiani, G., & Morari, F. (2024). Assessment of different agricultural soil compaction levels using shallow seismic geophysical methods. *Geoderma*,*447*. https://doi.org/10.1016/j.geoderma.2024.116914

Castro, I. J., Dias, J. M., & Lopes, C. L. (2023). Assessing Shoreline Changes in Fringing Salt Marshes from Satellite Remote Sensing Data. *Remote Sensing*, *15*(18). https://doi.org/10.3390/rs15184475

Da Lio, C., Teatini, P., Strozzi, T., & Tosi, L. (2018). Understanding land subsidence in salt marshes of the Venice Lagoon from SAR Interferometry and ground-based investigations. *Remote Sensing of Environment*, *205*, 56–70. https://doi.org/10.1016/j.rse.2017.11.016

D'Alpaos, A., Tognin, D., Tommasini, L., D'Alpaos, L., Rinaldo, A., & Carniello, L. (2024). Statistical characterization of erosion and sediment transport mechanics in shallow tidal environments – Part 1: Erosion dynamics. *Earth Surface Dynamics*, *12*(1), 181–199. https://doi.org/10.5194/esurf-12-181-2024

D'Alpaos, L. (2010). *Fatti e misfatti di idraulica lagunare. La laguna di Venezia dalla diversione dei fiumi alle nuove opere delle bocche di* (Vol. 44). Istituto Veneto di Scienze, Lettere ed Arti.

Evans, B. R., Brooks, H., Chirol, C., Kirkham, M. K., Möller, I., Royse, K., Spencer, K., & Spencer, T. (2022). Vegetation interactions with geotechnical properties and erodibility of salt marsh sediments. *Estuarine, Coastal and Shelf Science*, *265*. https://doi.org/10.1016/j.ecss.2021.107713

Everett, E. M. (2013). Near-Surface Applied Geophysics. *Cambridge University Press*.

Fagherazzi, S., Kirwan, M. L., Mudd, S. M., Guntenspergen, G. R., Temmerman, S., D'Alpaos, A., Van De Koppel, J., Rybczyk, J. M., Reyes, E., Craft, C., & Clough, J. (2012). Numerical models of salt marsh evolution: Ecological, geomorphic, and climatic factors. *Reviews of Geophysics*, *50*(1). https://doi.org/10.1029/2011RG000359

Farris, A. S., Defne, Z., & Ganju, N. K. (2019). Identifying salt marsh shorelines from remotely sensed elevation data and imagery. *Remote Sensing*, *11*(15). https://doi.org/10.3390/rs11151795

Feagin, R. A., M., S., Ravens, T. M., Möller, I., Yeager, K. M., & Baird, A. H. (2009). Does vegetation prevent wave erosion of salt marsh edges? *Proceedings of the National Academy of Sciences*, *106*(25), 10109-10113. https://doi.org/10.1073/pnas.0901297106

Finotello, A., Ielpi, A., Lapôtre, M. G. A., Lazarus, E. D., Ghinassi, M., Carniello, L., Favaro, S., Tognin, D., & D'Alpaos, A. (2024). Vegetation enhances curvature-driven dynamics in meandering rivers. *Nature Communications*, *15*(1). https://doi.org/10.1038/s41467-024-46292-x

FitzGerald, D. M., Hughes, Z. J. (2021). Salt marshes: function, dynamics, and stresses. *Cambridge University Press*. DOI: 10.1017/9781316888933.

Francalanci, S., Bendoni, M., Rinaldi, M., & Solari, L. (2013). Ecomorphodynamic evolution of salt marshes: Experimental observations of bank retreat processes. *Geomorphology*, *195*, 53–65. https://doi.org/10.1016/j.geomorph.2013.04.026

Friess, D. A., Spencer, T., Smith, G. M., Möller, I., Brooks, S. M., & Thomson, A. G. (2012). Remote sensing of geomorphological and ecological change in response to saltmarsh managed realignment, The Wash, UK. *International Journal of Applied Earth Observation and Geoinformation*, *18*(1), 57–68. https://doi.org/10.1016/j.jag.2012.01.016

Gasparotto, A. (2015). Architettura deposizionale ed idrodinamica di una barra tidale nella zona settentrionale della Laguna di Venezia. Master Thesis. *Università degli Studi di Padova*.

Gedan, K. B., Kirwan, M. L., Wolanski, E., Barbier, E. B., & Silliman, B. R. (2011). The present and future role of coastal wetland vegetation in protecting shorelines: Answering recent challenges to the paradigm. In *Climatic Change* (Vol. 106, Issue 1, pp. 7–29). https://doi.org/10.1007/s10584-010-0003-7

Hollis, L. O., & Turner, R. E. (2018). The tensile root strength of five emergent coastal macrophytes. *Aquatic Botany*, *146*, 39–47. https://doi.org/10.1016/j.aquabot.2018.01.004

Hou, J., Wang, H., Fu, B., Zhu, L., Wang, Y., & Li, Z. (2016). Effects of plant diversity on soil erosion for different vegetation patterns. *Catena*, *147*, 632–637. https://doi.org/10.1016/j.catena.2016.08.019

Houttuijn Bloemendaal, L. J., FitzGerald, D. M., Hughes, Z. J., Novak, A. B., & Georgiou, I. Y. (2023). Reevaluating the wave power-salt marsh retreat relationship. *Scientific Reports*, *13*(1). https://doi.org/10.1038/s41598-023-30042-y

JONASSON, S., & CALLAGHAN, T. V. (1992). Root mechanical properties related to disturbed and stressed habitats in the Arctic. *New Phytologist*, *122*(1), 179–186. https://doi.org/10.1111/j.1469-8137.1992.tb00064.x

Kervroëdan, L., Armand, R., Saunier, M., Ouvry, J. F., & Faucon, M. P. (2018). Plant functional trait effects on runoff to design herbaceous hedges for soil erosion control. *Ecological Engineering*, *118*, 143–151. https://doi.org/10.1016/j.ecoleng.2018.04.024

Kolker, A. S., Goodbred, S. L., Hameed, S., & Cochran, J. K. (2009). High-resolution records of the response of coastal wetland systems to long-term and short-term sea-level variability. *Estuarine, Coastal and Shelf Science*, *84*(4), 493–508. https://doi.org/10.1016/j.ecss.2009.06.030

Lopes, C. L., Mendes, R., Caçador, I., & Dias, J. M. (2020). Assessing salt marsh extent and condition changes with 35 years of Landsat imagery: Tagus Estuary case study. *Remote Sensing of Environment*, *247*. https://doi.org/10.1016/j.rse.2020.111939

Marani, M., Lanzoni, S., Silvestri, S., & Rinaldo, A. (2004). Tidal landforms, patterns of halophytic vegetation and the fate of the lagoon of Venice. *Journal of Marine Systems*, *51*(1-4 SPEC. ISS.), 191–210. https://doi.org/10.1016/j.jmarsys.2004.05.012

Marani, M., Silvestri, S., Belluco, E., Ursino, N., Comerlati, A., Tosatto, O., & Putti, M. (2006). Spatial organization and ecohydrological interactions in oxygen-limited vegetation ecosystems. *Water Resources Research*, *42*(SUPPL.). https://doi.org/10.1029/2005WR004582

Mariotti, G., & Carr, J. (2014). Dual role of salt marsh retreat: Long-term loss and short-term resilience. *Water Resources Research*, *50*(4), 2963–2974. https://doi.org/10.1002/2013WR014676

Martignon, C. (2013). Impatto della chiusura delle bocche di porto sui livelli di marea all'interno della laguna di Venezia in presenza di vento intenso. Master thesis. *Università degli Studi di Padova*.

Mel, R. A., Bendoni, M., & Steffinlongo, D. (2022). Salt-marsh retreat on different time scales: Issues and prospects from a 5-year monitoring campaign in the Venice Lagoon. *Earth Surface Processes and Landforms*, *47*(8), 1989–2005. https://doi.org/10.1002/esp.5359

Merlo, G. (2016). Analisi dell'evoluzione morfodinamica di un meandro a marea in Laguna di Venezia. Master thesis. *Università degli Studi di Padova*.

Möller, I., Kudella, M., Rupprecht, F., Spencer, T., Paul, M., Van Wesenbeeck, B. K., Wolters, G., Jensen, K., Bouma, T. J., Miranda-Lange, M., & Schimmels, S. (2014). Wave attenuation over coastal salt marshes under storm surge conditions. *Nature Geoscience*, *7*(10), 727–731. https://doi.org/10.1038/NGEO2251

Munari, G. (2016). Idrodinamica e distribuzione di sedimenti in barre di meandro tidale. Master thesis. *Università degli Studi di Padova*.

Pastro, M. (2016). Analisi delle caratteristiche morfometriche e sedimentologiche di un meandro a marea in Laguna di Venezia. Master thesis. *Università degli Studi di Padova*.

Puppin, A., Tognin, D., Ghinassi, M., Franceschinis, E., Realdon, N., Marani, M., & D'Alpaos, A. (2025). Depth-Distribution Patterns of Soil Organic Matter in the Tidal Marshes of the Venice Lagoon (Italy): Signatures of Depositional and Environmental Conditions. *Journal of Geophysical Research: Biogeosciences*, *130*(2). https://doi.org/10.1029/2024JG008327

Puppin, A. (2022). Soil Organic Matter and Carbon dynamics in Venice Lagoon salt marshes under natural and anthropogenic forcing. PhD thesis. *Università degli Studi di Padova*.

Reynolds, J. M. (2011). An Introduction to Applied and Environmental Geophysics, 2nd ed. *Wiley-Blackwell*.

Roner, M., D'Alpaos, A., Ghinassi, M., Marani, M., Silvestri, S., Franceschinis, E., & Realdon, N. (2016). Spatial variation of salt-marsh organic and inorganic deposition and organic carbon accumulation: Inferences from the Venice lagoon, Italy. *Advances in Water Resources*, *93*, 276–287. https://doi.org/10.1016/j.advwatres.2015.11.011

Rücker, C., Günther, T., & Wagner, F. M. (2017). pyGIMLi: An open-source library for modelling and inversion in geophysics. *Computers and Geosciences*, *109*, 106–123. https://doi.org/10.1016/j.cageo.2017.07.011

Schulte Ostermann, T., Heuner, M., Fuchs, E., Temmerman, S., Schoutens, K., Bouma, T. J., & Minden, V. (2021). Unraveling plant strategies in tidal marshes by investigating plant traits and environmental conditions. *Journal of Vegetation Science*, *32*(3). https://doi.org/10.1111/jvs.13038

Sharma, P. V. (1997). Environmental and Engineering Geophysics. *Cambridge University Press*.

Silvestri, S., Capra, V., Cucchiaro, S., Pivato, M., & Tarolli, P. (2022). Tides, Topography, and Seagrass Cover Controls on the Spatial Distribution of Pinna nobilis on a Coastal Lagoon Tidal Flat. *Journal of Geophysical Research: Biogeosciences*, *127*(3). https://doi.org/10.1029/2021JG006667

Silvestri, S., & Marani, M. (2013a). *Salt-Marsh Vegetation and Morphology: Basic Physiology, Modelling and Remote Sensing Observations* (pp. 5–25). https://doi.org/10.1029/ce059p0005

Silvestri, S., & Marani, M. (2013b). *Salt-Marsh Vegetation and Morphology: Basic Physiology, Modelling and Remote Sensing Observations* (pp. 5–25). https://doi.org/10.1029/ce059p0005

Soldati, M., Marchetti, M. (2017). Landscapes and Landforms of Italy. *Springer*.

Sun, C., Fagherazzi, S., & Liu, Y. (2018). Classification mapping of salt marsh vegetation by flexible monthly NDVI time-series using Landsat imagery. *Estuarine, Coastal and Shelf Science*, *213*, 61–80. https://doi.org/10.1016/j.ecss.2018.08.007

Tognin, D., D'Alpaos, A., Ghinassi, M., & Carniello, L. (2024). Marsh topography reveals the signature of storm-surge-driven sedimentation. *Geology*, *53*(1), 45–49. https://doi.org/10.1130/G52552.1

Tosi, L., Da Lio, C., Cosma, M., & Donnici, S. (2024). Vulnerability of tidal morphologies to relative sea-level rise in the Venice Lagoon. *Science of the Total Environment*, *931*. https://doi.org/10.1016/j.scitotenv.2024.173006

Tosi, L., Rizzetto, F., Bonardi, M., Donnici, S., Serandrei Barbero, R., & Toffoletto, F. (2007). NOTE ILLUSTRATIVE della CARTA GEOLOGICA D'ITALIA alla scala 1:50.000 foglio 128 VENEZIA A cura di Ente realizzatore. In *J. Centonze* (Issue 4).

Ursino, N., Cassiani, G., Deiana, R., Vignoli, G., & Boaga, J. (2014). Measuring and modeling water-related soil-vegetation feedbacks in a fallow plot. *Hydrology and Earth System Sciences*, *18*(3), 1105–1118. https://doi.org/10.5194/hess-18-1105-2014

Ursino, N., Silvestri, S., & Marani, M. (2004). Subsurface flow and vegetation patterns in tidal environments. *Water Resources Research*, *40*(5). https://doi.org/10.1029/2003WR002702

Vannoppen, W., De Baets, S., Keeble, J., Dong, Y., & Poesen, J. (2017). How do root and soil characteristics affect the erosion-reducing potential of plant species? *Ecological Engineering*, *109*, 186–195. https://doi.org/10.1016/j.ecoleng.2017.08.001

Xin, P., Kong, J., Li, L., & Barry, D. A. (n.d.). *Modelling of groundwater-vegetation interactions in a tidal marsh*.

Zago, F. (2016). Analisi dell'influenza del tipo di suolo sull'erosione dei margini di barena. Master thesis. *Università degli Studi di Padova*.

Zoccarato, C., Da Lio, C., Tosi, L., & Teatini, P. (2019). A Coupled Biomorpho-Geomechanical Model of Tidal Marsh Evolution. *Water Resources Research*, *55*(11), 8330–8349. https://doi.org/10.1029/2019WR024875

Google Earth (2025). Wikipedia, the free encyclopedia. 2025.

QGIS (2025). Google LLC. 2025.

QGIS Development Team (2024). QGIS Geographic Information System (version 3.40). Open Source Geospatial Foundation.

Seismic wave (2025). Encyclopedia Britannica. 2025.

ACKNOWLEDGEMENTS

While working on this thesis, I had the pleasure of meeting many brilliant people who encouraged me and taught me what I needed to learn. First, I thank my supervisor, Prof. Andrea D'Alpaos, who made this work possible. I cannot thank my co-supervisor, Prof. Jacopo Boaga, and Dr. Alberto Carrera enough for their patience and availability. Prof. Alvise Finotello and Dr. Tegan Blount taught me everything they could about remote sensing to make sure I was independent. I thank Dr. Alessandro Michielotto for his kindness in providing the numerical outputs of the wind wave-tidal model and Dr. Alice Puppin for supervising the analysis of the core samples. It was really a group effort, and I very much appreciate all your contributions.

I now have to thank my family. My parents made it possible for me to study here. It was truly a groundbreaking experience to live in another city and to attend an excellent university such as the University of Padova. From the bottom of my heart, thank you.

My siblings encouraged me when I needed them the most, always offering honest words and sharing similar experiences to make me feel less lonely. Also, my aunts, uncles, and cousins are to thank because every time I went back home, they always listened with interest to the tales from Padova that I told them.

New and old friends always make the difference. I thank you all for our shared experiences and laughs; you are all very precious to me.

My housemates deserve a special thanks. They saw all the ups and downs I went through, and even though we were forced to live together, I am happy to consider you my friends now.

A final thank you goes to my most beloved, Zelda and Marco. Zelda is unbelievably precious to me, and thoughts of her always bring a smile to my face. Marco was the last person to enter my life, but he has been there for me since day one. He always provided the very much needed rational insight and valuable opinions that I sometimes lack. Thank you for your love and support.